Wind Farm Layout Optimization over Complex Terrain

オマ, モハメド, アリ, モハメド, イブラヒム

https://doi.org/10.15017/4059955

出版情報：Kyushu University, 2019, 博士（学術）, 課程博士
バージョン：
権利関係：

Wind Farm Layout Optimization over Complex Terrain

Omar M. Ali M. Ibrahim

Supervised by
Professor Shigeo Yoshida

Department of Energy and Environmental Engineering
Interdisciplinary Graduate School of Engineering Sciences
Kyushu University

July 2019

Dissertation submitted to the Department of Energy and Environmental Engineering, Interdisciplinary Graduate School of Engineering Sciences, Kyushu University, Fukuoka, Japan in partial fulfillment of the requirements for the degree of Doctor of Philosophy in Engineering.

Department of Energy and Environmental Engineering

Interdisciplinary Graduate School of Engineering Sciences

Kyushu University

6-1 Kasuga-koen, Kasuga, Fukuoka, 816-8580, Japan

Abstract

Over the last decade, more onshore wind farms were constructed over or near to complex terrain such as: hills and mountains. Complex terrains can have an impact on wind turbine performance and power output. In this thesis, the flow over a steep two-dimensional hill as well as the performance of a turbine located over the same hill was examined to investigate the effect of complex terrain on wind turbine performance. A good agreement between Experimental and Numerical simulations was achieved for the average vertical wind speed profiles. These results displayed the impact of the steep hill on air flow. A good agreement between wind tunnel test and Computational Fluid Dynamics (CFD) results was achieved for the wind turbine power coefficient by using the Transition SST model. The Transition SST model yielded better results than the SST k-omega turbulence model specifically at high tip speed ratios.

An engineering wake model, that considers acceleration on a two-dimensional hill, was developed based on the momentum theory. The model consists of the wake width and wake wind speed. The equation to calculate the rotor thrust, which is calculated by the wake wind speed profile, was also formulated. Then, the model was validated through wind tunnel test and CFD. The results obtained by using the current model were close to the wind tunnel test and CFD results, and by using the current model, it was possible to estimate the wake shrinkage in accelerating two-dimensional wind field.

In this thesis, a wind-tunnel test was conducted to investigate wake development over a two-dimensional hill in simple flow conditions, where a uniform approach-flow with turbulence intensity less than 0.5 % was used. Conducting the wind-tunnel test in such simple flow conditions was necessary for this study in order to investigate the effect of the hill on wake development and evaluate the new wake model without the influence of the Atmospheric Boundary Layer (ABL), ground roughness, or turbulence.

The wake model was compared with the wind-tunnel test, and the results obtained by using the wake model were close to the wind-tunnel test results. The wake model was able to estimate the wake shrinkage in accelerating two-dimensional wind field.

The measured wake width at the top of the hill was lower than the estimated value (by the wake model), this could be because the wake center at the top of the hill was moved downwards due to the hill effect.

In the wind-tunnel test, the hill surface was smooth as it was made of ABS resin, however, the surface roughness may affect wind speed profiles over the hill. Consequently, the effect of the surface roughness on wake development must be considered in the future studies.

Further experimental and numerical studies where the approach-flow represents real atmospheric conditions (where the ABL is reproduced) are required to investigate wake development over the hill in conditions that wind turbines experience in the field. Finally, further modifications to the wake model are necessary to include the effect of turbulence and ground roughness on wake development over the hill, and to extend the wake model to decelerating wind field (downstream of the hill).

The wake model introduced in this thesis could be integrated into wind farm layout optimization algorithms to estimate far-wake shrinkage in accelerating wind field, which was not possible previously using the Jensen or the adapted Jensen wake models.

A wind farm layout optimization algorithm was developed, where a Genetic Algorithm was used as an initial step for the optimization process. Then, a new Random Algorithm was developed to overcome the limitations of the Genetic Algorithm and improve the output of the optimization algorithm. CTFLOW (Complex Terrain Farm Layout Optimization Workbench) was developed by the author for layout optimization over complex terrain. CTFLOW can import satellite terrain images then convert them directly to an STL file, rather than creating the STL file manually.

Acknowledgment

I would like to thank Professor Shigeo Yoshida for accepting me as a student in his laboratory. Professor Yoshida always took time to discuss my research results and further procedures. Professor Jun Tanimoto and Professor Aya Hagishima acted as referees for this thesis and they are sincerely acknowledged. Furthermore, I would like to thank Dr. Yingyi Liu for his valuable suggestions and advice, and I appreciate the cooperation with all my fellow students and researchers in Chikushi campus, Kyushu University.

The author is thankful for receiving scholarship from the Advanced Graduate Program in Global Strategy for Green Asia, Kyushu University, Japan.

July 2019

Omar M. Ali M. Ibrahim

Contents

List of Figures

List of Tables

List of Symbols

Symbol	Description
a	Slope of the hill
a_0	Axial induction factor
$C_{O\&M}$	Annual operation and maintenance cost per wind turbine
C_P	Power coefficient
C_s	Cost per substation
C_T	Thrust coefficient
$C_{T\,Hill}$	Thrust coefficient calculated by the wake wind speed profile over the two-dimensional hill
C_{WT}	Cost per wind turbine
D	Wind turbine rotor diameter
D_{wake}	Wake width
h	Height of the two-dimensional hill
L	Two-dimensional hill half-length
M	Number of wind turbines for each substation
m_B	Momentum loss in the wake caused by the rotor
m_{disc}	Rate of change of momentum caused by the disc
m_T	Rate of change of momentum caused by the terrain
N	Number of wind turbines
n	Revolutions per minute
P	Power
P_{WF}	Wind farm power output
R	Wind turbine rotor radius
S	Cross sectional area of the wind stream tube
T	Thrust
U	Wind velocity
U_{B0}	Wind velocity outside the wake at location B

Δp	Pressure difference across the actuator disc
λ	Tip speed ratio
ρ	Density
ω	Rotor speed in rad/s

Subscripts

R	Relevant to circumstances at the rotor
W	Relevant to circumstances in the wake (between the rotor and $X= -L$)
B	Relevant to circumstances between X= -L and X=0
∞	Relevant to circumstances upstream of the turbine

Acronyms

ABL	Atmospheric Boundary Layer
AD	Actuator Disc
AL	Actuator Line
CFD	Computational Fluid Dynamics
COE	Cost of Energy
GA	Genetic Algorithm
HAWT	Horizontal Axis Wind Turbine
LES	Large Eddy Simulation
LMADT	Linear Momentum Actuator Disc Theory
RA	Random Algorithm
SST	Shear Stress Transport
SGS	Subgrid-Scale

TSR	Tip Speed Ratio
VAWT	Vertical Axis Wind Turbine

1 Introduction

1.1 Wind

Wind is the movement of air from areas with high pressure to areas with low pressure. The pressure difference is caused by the uneven heating of the earth's surface by the sun's radiation. When the air temperature on the surface increases relative to the air above, the air will start rising upwards due to the difference in densities. The rising air mass causes low pressure areas which draws air from the surrounding regions, as shown in Figure 1.1.

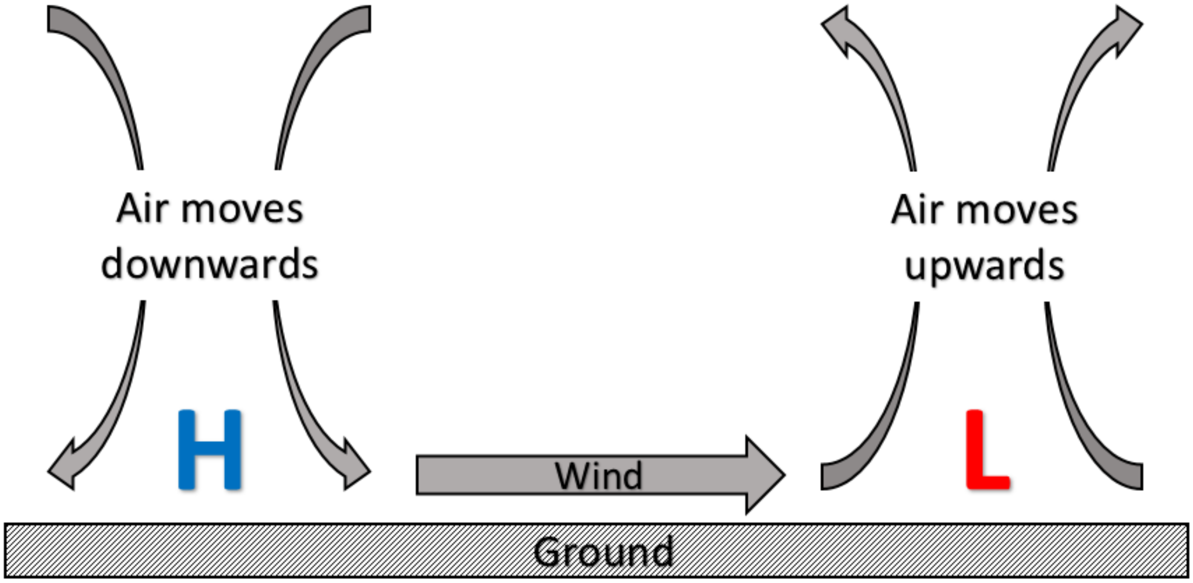

Figure 1.1 Wind is caused by air movement from areas with high pressure to areas with low pressure.

1.2 Wind Energy

Wind energy refers to the process of generating electricity using wind. Wind turbines converts wind’s kinetic energy to mechanical energy, then the mechanical energy is converted to electricity through a generator. Figure 1.2 shows the main components of a wind turbine.

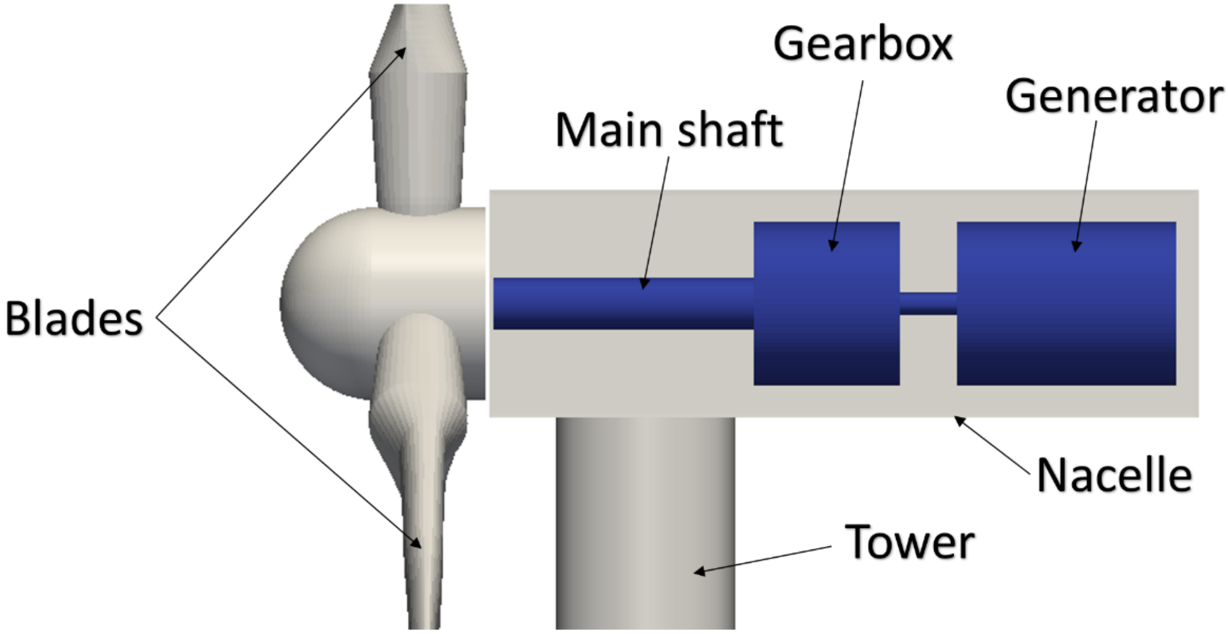

Figure 1.2 A schematic of the main components of a wind turbine.

Wind energy usage for electricity generation has been growing over the last years. According to the World Wind Energy Association (WWEA), “The overall capacity of all wind turbines installed worldwide by the end of 2018 reached 600 Gigawatt” [1], and “all wind turbines installed worldwide by mid-2016 can generate around 4,7 % of the world’s electricity demand” [2]. Figure 1.3 shows worldwide wind capacity from 2012 to 2016.

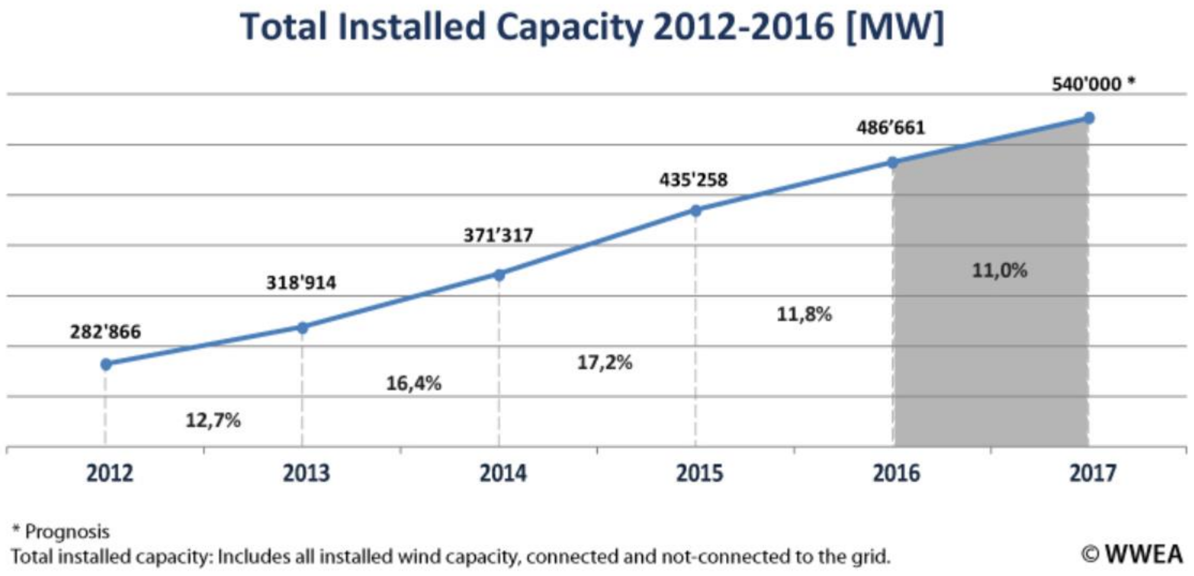

Figure 1.3 Worldwide wind capacity from 2012 to 2016 [3].

Mainly, there are two types of wind turbines, Horizontal Axis Wind Turbine (HAWT), and Vertical Axis Wind Turbine (VAWT). The axis of rotation of a HAWT is horizontal (parallel to wind stream), while the axis of rotation of a VAWT is vertical (perpendicular to the ground). HAWT can be single bladed or multi bladed, upwind or downwind type. The three bladed upwind HAWT are the most widely used wind turbines for electricity generation in multi-MW wind farms nowadays. Increasing wind turbine rotor diameter has been a major direction over the last years to generate more energy and reduce the cost of energy production. Figure 1.4 illustrates the growth of wind turbine size from 1980 to 2005.

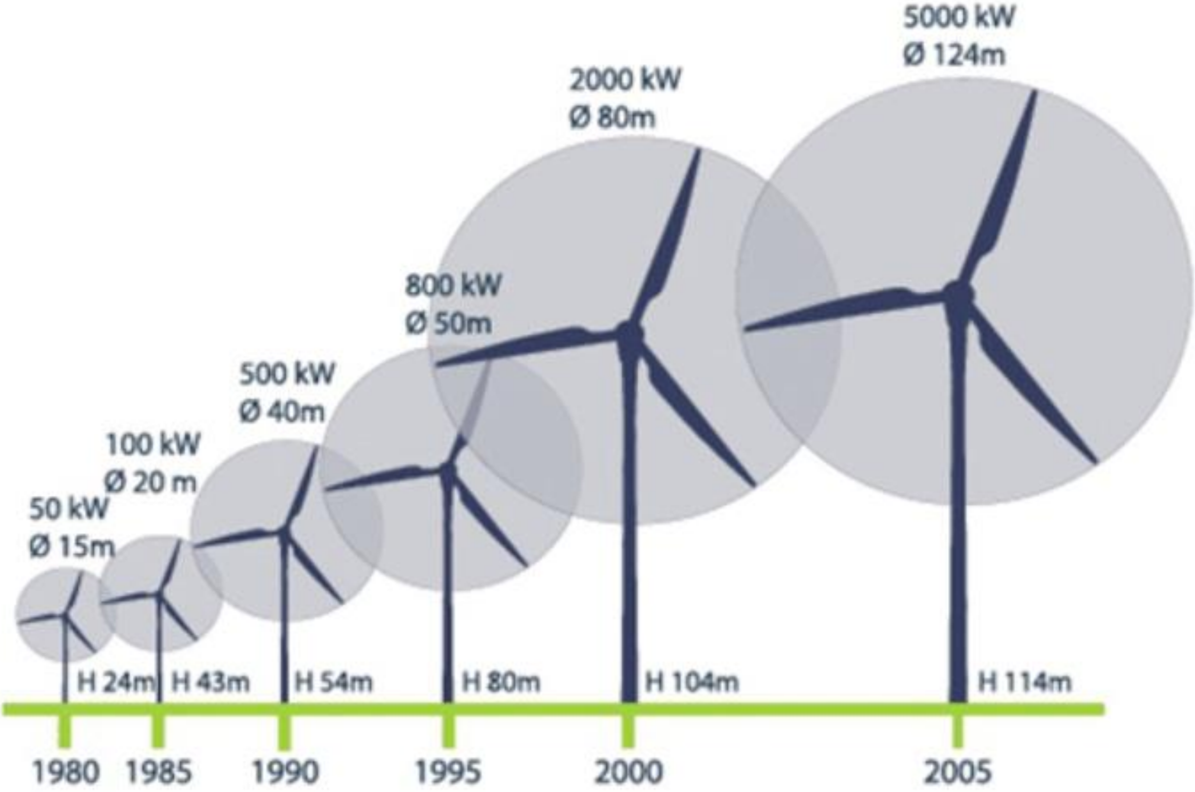

Figure 1.4 Wind turbine size growth from 1980 to 2005 [4].

1.3 Wind Farm

A wind farm consists of a group of wind turbines (as shown in Figure 1.5) in order to reduce the cost of energy production. Wind speed decreases as upstream wind turbines extract wind kinetic energy in a wind farm. As a consequence, power output of downstream turbines drastically decrease [5] [6]. Power output reduction of downstream turbines could be 10 – 40 %, depending on wind speed profiles and wind direction [7] [8], [9].

Figure 1.5 Thanet off-shore windfarm [10].

1.4 Wind Turbine Wake

The area behind a wind turbine is called wake (as shown in Figure 1.6), and it can be divided into two areas: a near wake and a far wake [11]. The near wake is the area from the wind turbine rotor to roughly one wind turbine rotor diameter downstream as shown in Figure 1.7. As the thrust acting on the wind turbine rotor increases the wake velocity decreases and the difference between the wind velocity inside and outside the wake (shear) increases [12]. Turbulent wake state happens when a very high load acts on the rotor, leading to the conversion of a large amount of kinetic energy of the incoming flow into turbulent motion. The turbulence in the wake mixes the low wind velocity of the wake with the high wind velocity outside of the wake resulting in wake expansion [12].

Figure 1.6 Horns rev offshore wind farm [13], where wind-turbine wakes are visible due to fog.

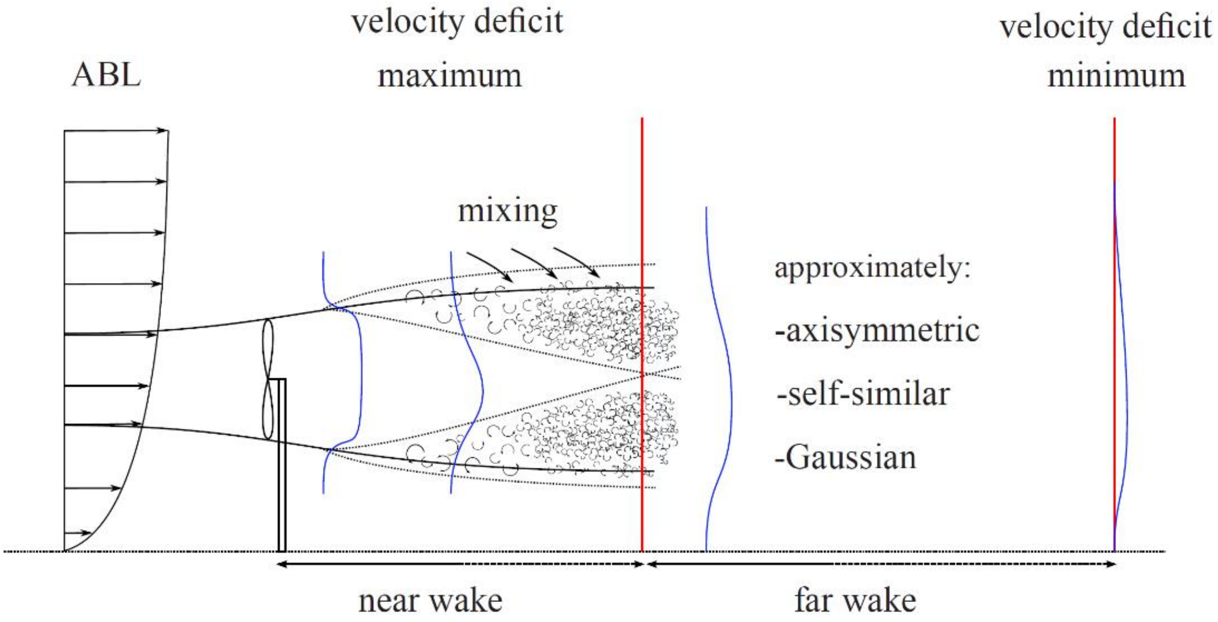

Figure 1.7 Wind turbine wake [12].

Development of the turbulent wake is affected by several factors, such as: wind farm terrain shape, atmosphere turbulence levels, wind turbine operation conditions, and vertical wind speed gradients. When the ambient turbulence levels are low, wind turbine wake recovers slower and wake velocity deficit increases [14]. Therefore, the power output difference between a wind turbine and the first row turbine is higher at low ambient turbulence levels and low wind velocities [15]. Also, tower, nacelle of the wind turbine, and tip vortices could cause turbulence [16] [17]. It was noticed that turbulence is still existing at a distance of 15 rotor diameter (*D*) [18], and the load acting on the wind turbine rotor could increase due to turbulence by 45% at 5*D* and 10% at 9.5*D* in the case of operating in a full wake [19].

Array efficiency is the power output of the total wind farm divided by the total power that could be generated by the same amount of wind turbines if standing alone [12]. Array efficiency is affected by ambient turbulence intensity and wind farm layout [6]. If the ambient turbulence intensity is high, turbulent mixing happens in the wind turbine wake, therefore, wind turbine wake recovery is faster. If the ambient turbulence intensity is low, wind turbine wake recovery is slower. A study showed that when a downstream wind turbine is partially operating in an upstream wind turbine wake, it experiences high loads [20].

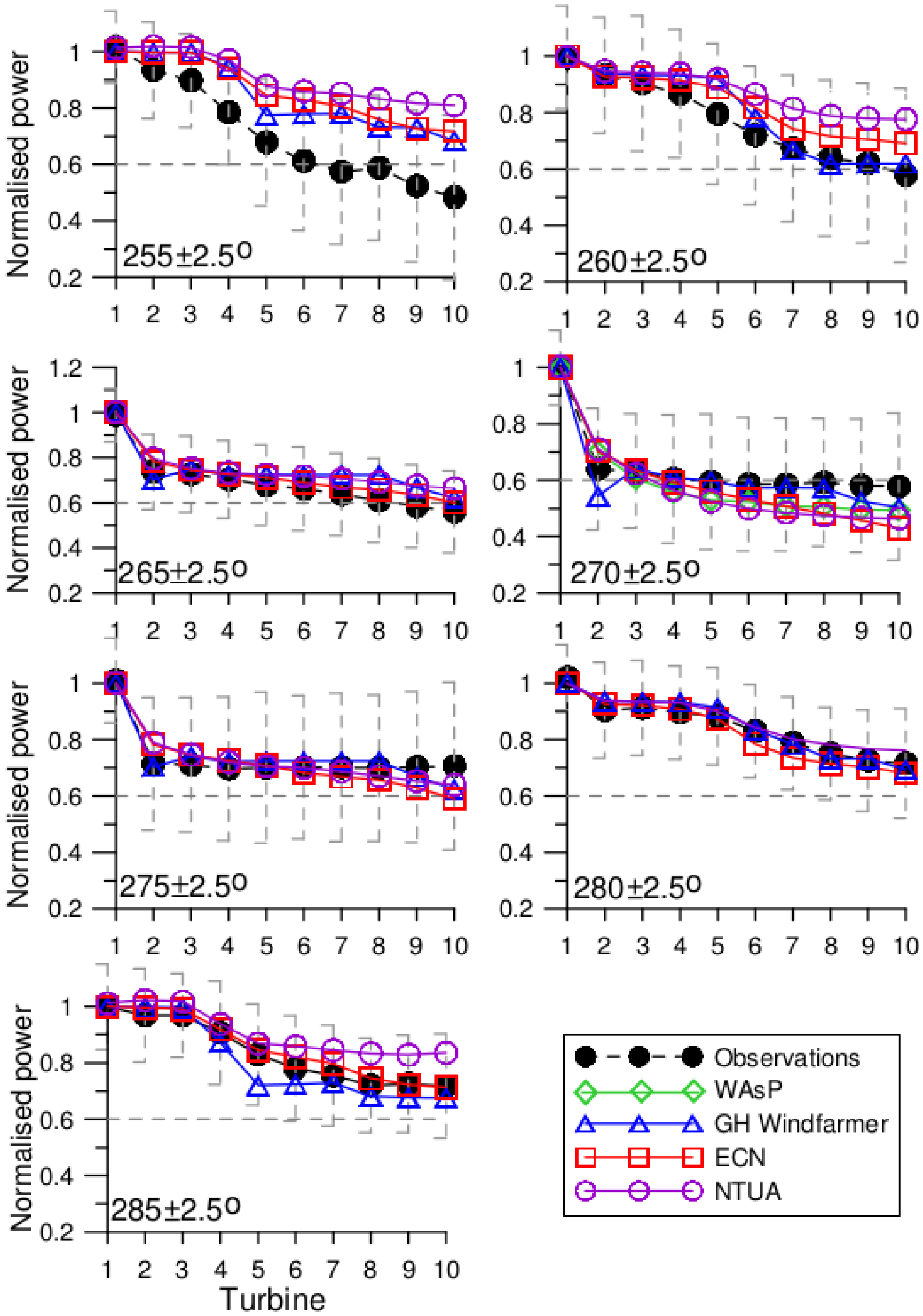

Figure 1.8 Comparison between observations and different models of the normalized power as function of turbine number in a wind farm [8].

Downstream wind turbine wakes recovery is faster than the first row wind turbine wakes, because upstream wind turbines increase turbulence levels leading to better turbulent mixing in the wake of the downstream wind turbines [8]. Figure 1.8 shows the normalized power as function of turbine number in a wind farm [8]. Measurements were compared to different models such as: WAsP, GH Windfarmer, ECN, and NTUA. This comparison showed that there is a huge power loss between the first and second row of wind turbines, however, the power loss in successive wind turbines is much smaller. The power output of the downstream wind turbines is almost constant. This constant power output in the downstream wind turbines could be due to an equilibrium value of turbulence was accomplished [8].

The movement of the wind turbine wake is called wake meandering as shown in Figure 1.9. Wake meandering may happen because of eddies larger than the wake size [12]. Wake meandering can increase fatigue loads acting on wind turbines, and it can also decrease the mean wake deficit and power losses [12]. Ainslie modeled the effect of wake meandering on wake deficits, and he founded that wake meandering effect is notable in decreasing the depth of the deficits [17]. Larsen et al [21] have studied wind turbine wake meandering using full scale wake experiments and a numerical model, and they developed a model for the dynamic wake meandering phenomenon. This model does not take into account the interaction between different wind turbine wakes. Some experimental studies [22] [23] proposed that wind turbine wake meandering happens due to wake instability.

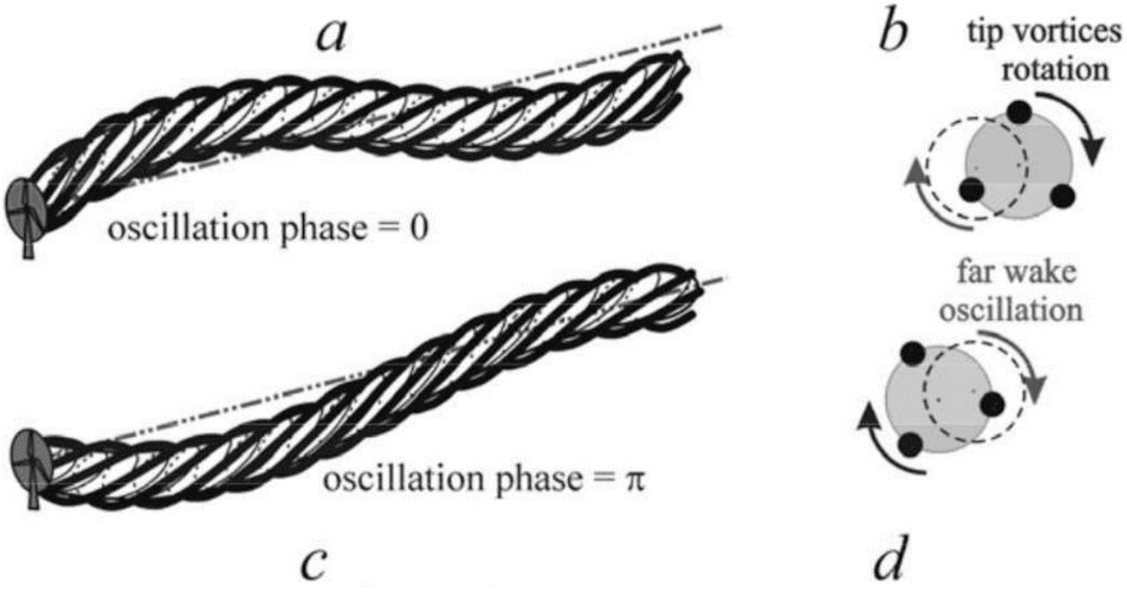

Figure 1.9 Wind turbine wake meandering [21].

1.5 Linear Momentum Actuator Disc Theory

Linear Momentum Actuator Disc Theory (LMADT) was used by Betz to determine the limit of power extraction in a fluid [24]. Figure 1.10 shows the actuator disc and the geometry of the flow. As the fluid passes the rotor disc the fluid slows down because its kinetic energy decreases, and the stream tube cross-sectional area expands due to the decrease in fluid velocity [24].

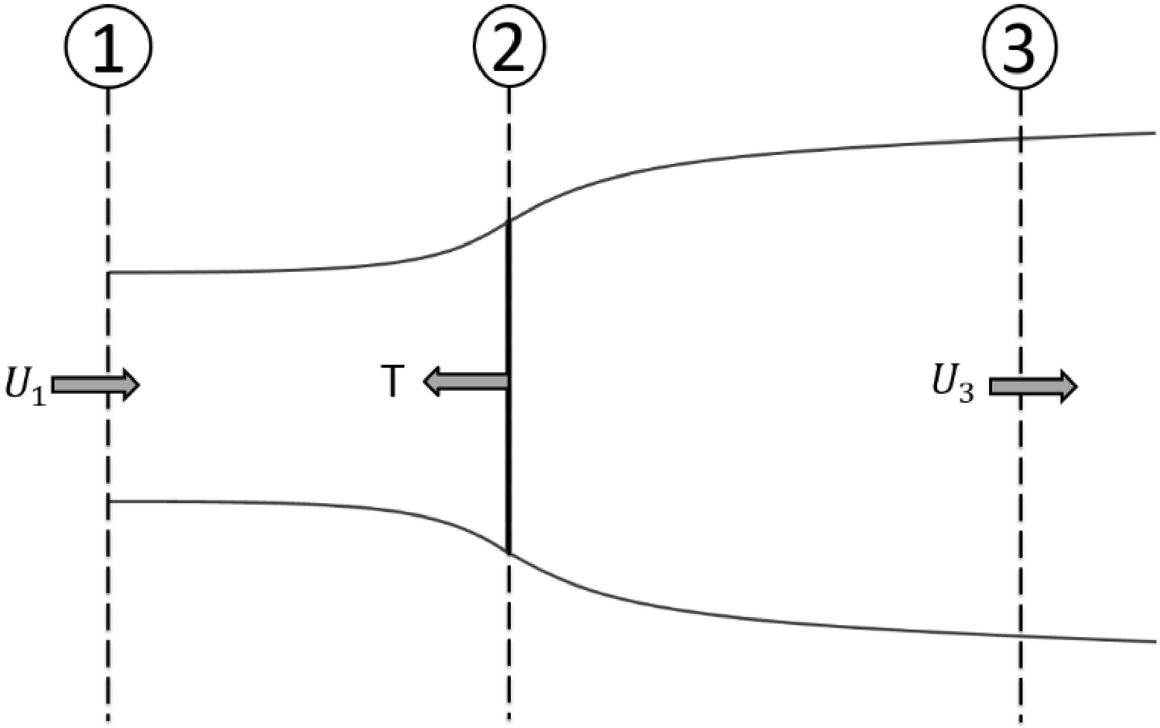

Figure 1.10 The actuator disc and the geometry of the fluid flow.

Three reference locations are considered as shown in Figure 1.10, the far upstream from the rotor (denoted with 1), rotor (denoted as 2), and the far downstream from the rotor (denoted as 3).

The mass flow rate has to be the same upstream and downstream of the turbine, therefore,

$$\rho S_1 U_1 = \rho S_2 U_2 = \rho S_3 U_3 \tag{1.1}$$

Where U is the fluid velocity, T is the thrust from the actuator disc to the fluid, ρ is the fluid density, and S is the cross-sectional area.

U_2 can be defined as follows:

$$U_2 = U_1(1 - a_0) \tag{1.2}$$

Where a_0 is the axial induction factor.

Since the disc causes the fluid velocity to change from U_1 to U_3 as shown in Figure 1.10, therefore, the rate of change of momentum caused by the disc (m_{disc}) is as follows:

$$m_{disc} = (U_1 - U_3)\rho S_2 U_2 \tag{1.3}$$

The force (T) causing the change of momentum can be represented as follows:

$$\mathrm{T} = (U_1 - U_3)\rho S_2 U_1 (1 - a_0) \tag{1.4}$$

By applying Bernoulli equation along the stream line, the pressure difference across the actuator disc (Δp) can be obtained:

$$\Delta p = \frac{1}{2}\rho\,({U_1}^2 - {U_3}^2) \tag{1.5}$$

Therefore, from equation (1.4):

$$\frac{1}{2}\rho\left({U_1}^2 - {U_3}^2\right)S_2 = (U_1 - U_3)\rho S_2 U_1(1 - a_0) \tag{1.6}$$

$$U_3 = (1 - 2a_0)U_1 \tag{1.7}$$

Therefore, from equation (1.4):

$$\mathrm{T} = 2\rho S_2 {U_1}^2 a_0(1 - a_0) \tag{1.8}$$

Therefore Power (P),

$$P = \mathrm{T}U_2 = 2\rho S_2 {U_1}^3 a_0(1 - a_0)^2 \tag{1.9}$$

The power coefficient (C_P) can be defined as follows:

$$C_P = \frac{Power}{\frac{1}{2}\rho {U_1}^3 S_2} \tag{1.10}$$

Therefore:

$$C_P = 4a_0(1 - a_0)^2 \tag{1.11}$$

The maximum power extracted from the fluid can be obtained when:

$$\frac{dC_P}{da_0} = 4(1 - a_0)(1 - 3a_0) = 0$$

Which gives a value of $a_0 = 1/3$

Therefore C_P = 16 / 27, which is the maximum achievable value of the power coefficient (the Lanchester-Betz limit).

1.6 Wind Turbine Wake Models

1.6.1 Jensen Wake Model

Jensen model [25] is a simple wind turbine wake model. The wake is assumed to expand linearly as shown in Figure 1.11. It is also assumed that the downstream velocity is constant. By using this model, it is possible to obtain the velocity at a given distance along the far wake region of the turbine, however, for the near wake region, this wake model gives inaccurate results [25].

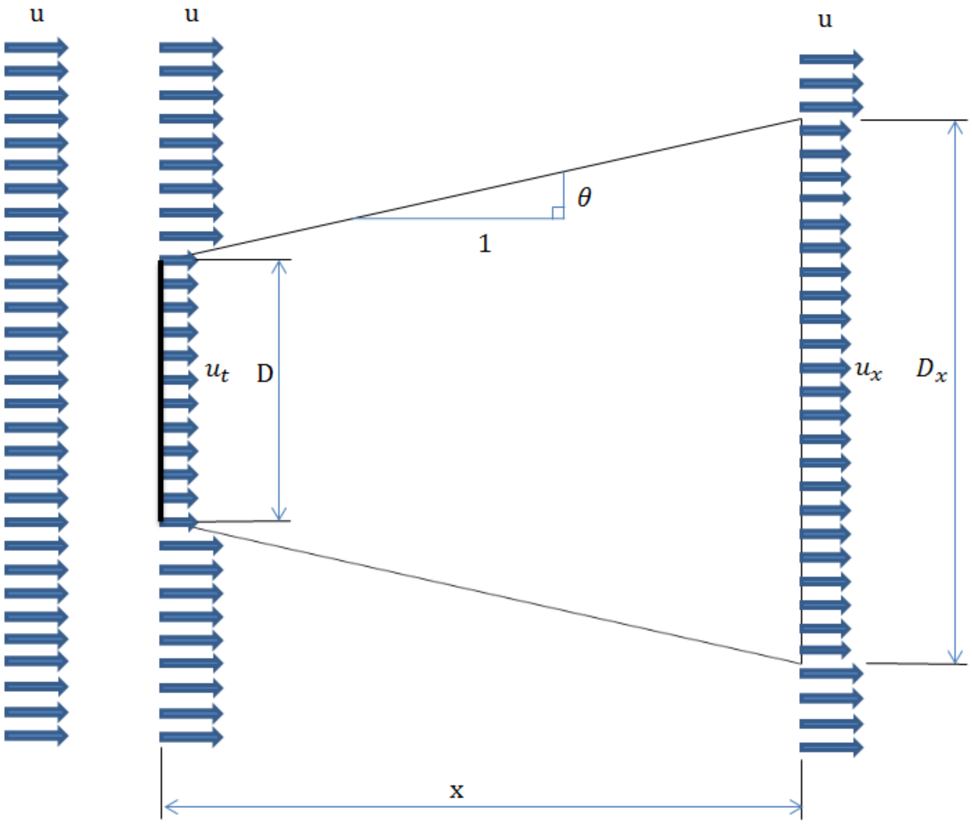

Figure 1.11 Jensen wake model.

From Figure 1.11, the following expression can be used to obtain the diameter at distance x (D_x):

$$D_x = \mathrm{D} + 2\,\theta\,\mathrm{x} \tag{1.12}$$

The balance of momentum gives the following expression:

$$D^2\,u_t + (D_x^2 - D^2)\,\mathrm{u} = D_x^2\,u_x \tag{1.13}$$

The wake velocity at a given distance x (u_x) can be obtained by the following expression:

$$u_x = \mathrm{u} + \mathrm{u}\,(\sqrt{1 - \mathrm{C_T}} - 1)\,(\frac{D}{D_x})^2 \tag{1.14}$$

1.6.2 Adapted Jensen Wake Model

Feng and Shen [26] tried to adapt Jensen wake model so that it can account for the terrain effects. The adapted Jensen wake model assumes that the wake expands linearly and the center of the wake follows terrain shape along the streamwise direction as shown in Figure 1.12. It also assumes that velocity deficit and wake zone radius develop linearly according to the travelling distance. But, the model includes a contradiction with the physics of fluid-dynamics such as conservation of flow rate and momentum.

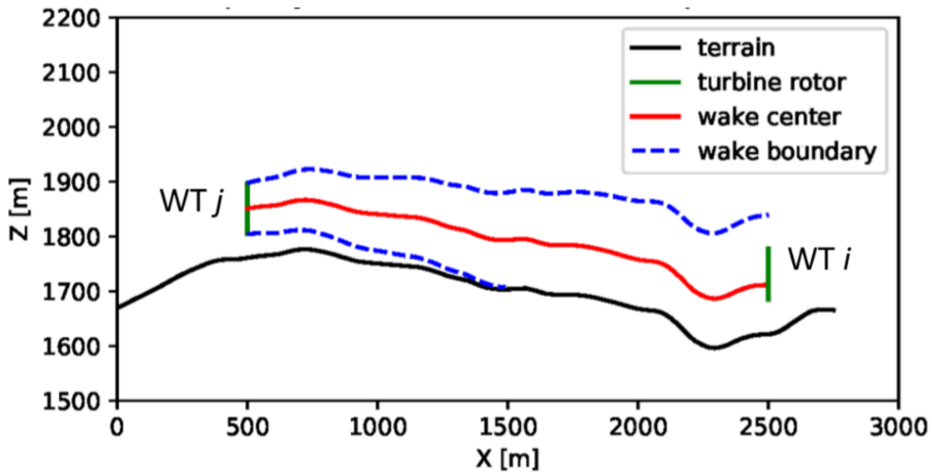

Figure 1.12 Adapted Jensen wake model [27]

The wind speed (V_{ij}) can be obtained using the following equation:

$$V_{ij} = S(x_j)V_0\left[1 - \frac{1-\sqrt{1-C_T(S(x_j)V_0)}}{\left(1+\alpha(s_{ij}/R_r)\right)^2}\right] \tag{1.15}$$

Wake zone radius (R_{ij}) of the wake of WT$_j$ when arriving the streamwise level where WT$_i$ located, can be obtained using the following equation:

$$R_{ij} = \alpha s_{ij} + R_r \tag{1.16}$$

Where S is the speed-up factor of a given position at the hub height.

1.7 Complex Terrain

Over the last decade, more onshore wind farms were constructed over or near to complex terrain such as: hills and mountains (Figure 1.13). Complex terrain can be defined as any terrain that can affect wind flow. Moreover, Complex terrains can have an impact on wind turbine performance and power output. The performance of a wind turbine placed at several locations over a hill, where the vertical wind component changes significantly, was affected by the terrain [28], [29], [30]. Uchida et al. [31] showed that the pitch control of a wind turbine was incapable of reacting properly to wind speed variation that resulted from the terrain upstream of the wind farm. In addition, complex terrains can have a negative impact on wind turbine life time. Li et al. [32] found that varying wind speeds resulted from complex terrain was the reason of the recurrent failure of a wind turbine yaw system (Figure 1.14). Furthermore, complex terrains can influence wind turbine wakes and wind speed profiles in a wind farm. As a consequence, predicting wind turbines performance and energy production over complex terrains is more difficult than that over flat terrains. Flow over complex terrain was investigated in many previous studies. A wind-tunnel test [33] that examined the flow over a Gaussian hill showed higher hub height mean velocity and lower turbulence intensity at the top of a hill compared to that downstream of the hill. Webster et al. [34] studied flow over a two-dimensional bump, and the study indicated that the boundary layer over the two-dimensional bump was different from that over a flat terrain. Helmis et al. [35] investigated flow over a complex terrain, and the study suggested that applying a simple logarithmic extrapolation formula to calculate hub height wind speed can lead to unreliable results.

The flow over a hill is influenced by the roughness and steepness of the hill, where rough hills with steeper slopes are more likely to cause flow separation downstream of the hill [36]. A number of linear flow models [37] [38] [39] [40] have been developed to predict the flow field over hills, however, the validity of these linear flow models decreases significantly when considering flow over hills with steeper slopes, therefore, these linear flow models can only be used to predict flow over hills of modest slopes [36]. Cao and Tamura [41] performed wind-tunnel tests to investigate surface roughness effects on the flow over a two-dimensional steep hill, and the study showed that the speed-up ratio at the top of a rough hill is greater than that of a smooth hill, and the flow separation region of a rough hill extends farther downstream than that of a smooth hill. Also, for a rough hill, the position of the maximum turbulence intensity is located farther downstream than that for a smooth hill. Allen [42] studied the flow over hills with variable roughness, and the study indicated that the roughness change can either cause or prevent flow separation depending on the location and size of the roughness change. Cao and Tamura [43] performed wind-tunnel tests to examine the effects of roughness blocks on the flow over a two-dimensional hill, and the study suggested that the velocity deficit and turbulence structure downstream of the hill are significantly affected by the number and location of roughness blocks on the hill surface or upstream of the hill.

Figure 1.13 Wind turbine in complex terrain.

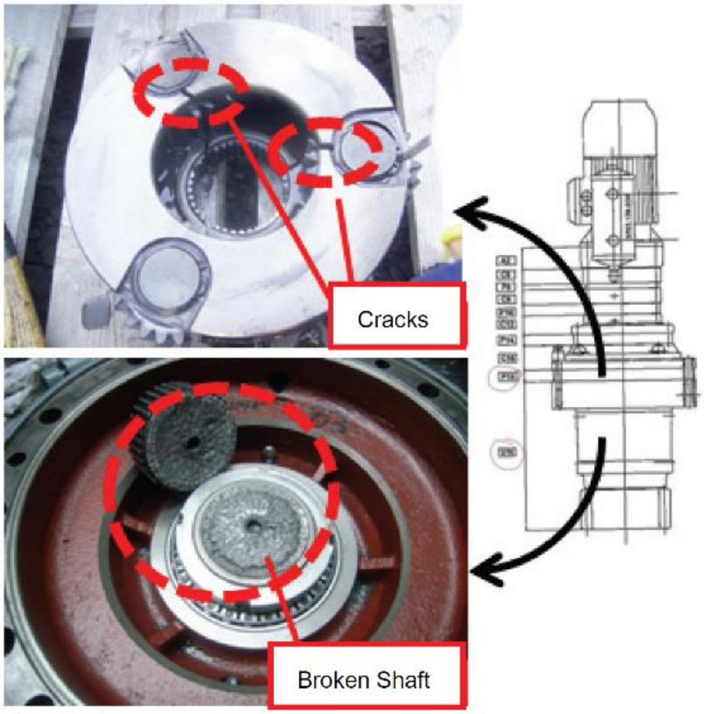

Figure 1.14 Wind turbine component damage due to turbulence induced by complex terrain [32].

Terrain effect on wind-turbine wakes was investigated in several studies. Politis et al. [44] studied wake development of a wind turbine placed over a Gaussian hill, and the study showed that the velocity deficit over a hill existed at farther distances than over a flat terrain. Makridis and Chick [45]conducted Computational Fluid Dynamics (CFD) simulations for wind turbines in complex terrain, where the wind turbine rotor was modelled as an Actuator Disc (AD), then the results were validated with measurements. Hansen et al. [46] studied wind turbine wake properties over complex terrain by examining high frequency time series measurements, and the study showed that complex terrain can greatly influence wind turbine wake. The influence of a complex terrain on the wakes of a group of four wind turbines was studied through numerical and experimental data [47], [48], and the study showed that the wake of the upstream turbine was distorted due to the terrain effect, and as a result, the upstream wake recovered faster than what would occur over flat terrain. Hyvärinen and Segalini [49], [50] studied wind turbine wake development over sinusoidal hills through wind tunnel test and numerical simulations, and the results showed a faster wake recovery over the hilly terrain. The Large Eddy Simulation (LES) model was used for wake modelling, where the wind turbine rotor was modelled as an AD [51] and Actuator Line (AL) [52], then the simulation results were compared with wind tunnel tests, achieving good agreement. The LES model was also used in other Ref. [53], [54] to simulate wind-turbine wakes over complex terrains. Literature reviews on wind turbine wake aerodynamics were reported by Vermeer et al. [11] and Sanderse [12]. The literature reviews include some experimental and numerical studies of wind turbine wakes over complex terrain.

1.8 Objectives and Approaches

Wind farm layout optimization using full scale experiments or numerical simulations, which include wind turbine rotors, is infeasible. Therefore, a simple engineering model such as Jensen wake model [25] is widely used for wind farm layout optimization. Jensen wake model assumes that the wake expands linearly, and the wake velocity is uniform. However, Jensen wake model does not take into account the terrain effects. Feng and Shen [26] tried to adapt Jensen wake model so that it can account for the terrain effects. The adapted Jensen wake model assumed that the wake expands linearly and the center of the wake follows terrain shape along the streamwise direction. But, the model includes contradiction with physics of fluid-dynamics such as conservation of flow rate and momentum.

Considering the situations above, an engineering wake model, which considers wind acceleration, was developed based on the momentum theory in this research. The wake model consists of the wake width and wake wind speed. The equation to calculate the rotor thrust, which is calculated by the wake wind speed profiles, was also formulated. Then, the model was validated through wind tunnel test and CFD. The results obtained by using the current model were close to the wind tunnel test and CFD results, and by using the current model, it was possible to estimate the wake shrinkage in accelerating two-dimensional wind field.

Furthermore, wind tunnel tests and Numerical simulations were performed to study the effect of a steep two-dimensional hill on the performance of a horizontal axis wind turbine. Experiments were performed in the wind tunnel to measure the average vertical wind speed profiles over the hill and the load acted on the wind turbine at a number of locations over the hill. Flow over the hill and wind turbine power coefficient were examined using CFD simulations where the wind turbine rotor was fully resolved. CFD simulations had a good agreement with wind tunnel test results, and current studies showed the great impact of the hill on the performance of wind turbines.

2 Wake Model Formulation

An engineering wake model, which considers acceleration on a two-dimensional hill, is formulated in this chapter based on the momentum theory. The model consists of the wake width and wake wind speed [55]. The equation to calculate the rotor thrust, which is calculated by the wake wind speed profiles, is also formulated.

2.1 Thrust Coefficient over a Two-Dimensional Hill

In this chapter, the thrust and the thrust coefficient equations will be formulated to include the acceleration of the wind upstream of a steep two-dimensional hill. Figure 2.1(a) and 1(b) show wind turbine wake over a flat terrain and a two-dimensional hill respectively, where L is the hill half-length, and X is the streamwise direction. As the turbine extracts kinetic energy from the wind, the wind has to slow down and expand. The mass flow rate has to be the same upstream and downstream of the turbine, therefore,

$$\mathrm{\rho S_\infty U_\infty = \rho S_R U_R = \rho S_W U_W = \rho S_B U_B} \tag{2.1}$$

where ρ is the air density, S is the cross sectional area of the wind stream tube, and U is the wind velocity. The subscript ∞ is relevant to circumstances upstream of the turbine, R is relevant to circumstances at the rotor, W is relevant to circumstances in the wake (between the rotor and $X= -L$), and B is relevant to circumstances between $X= -L$ and $X=0$.

The momentum loss in the wake caused by the rotor (m_B) is as follows:

$$\mathrm{m_B = -\rho {U_{B0}}^2 \int_{-\infty}^{\infty} \frac{U_B}{U_{B0}}\left(1 - \frac{U_B}{U_{B0}}\right) dS_B = -\rho {U_{B0}}^2 S_B \nu_B (1 - \nu_B)} \tag{2.2}$$

where, U_{B0} is the wind velocity outside the wake at location B, and $\nu_B = U_B/U_{B0}$.

Since the terrain causes the wind velocity to change from U_W to U_B as shown in Figure 2.1(b), therefore, the rate of change of momentum caused by the terrain (m_T) is as follows:

$$\mathrm{m_T} = \rho \mathrm{S_B} \mathrm{U_B}^2 - \rho \mathrm{S_W} \mathrm{U_W}^2 = \rho \mathrm{U_B}^2 \mathrm{S_B} \left(1 - \frac{1}{\sigma}\right) = \rho \mathrm{U_{B0}}^2 \mathrm{S_B} \nu_\mathrm{B}^2 \left(1 - \frac{1}{\sigma}\right) \qquad (2.3)$$

where, $\sigma = U_B/U_W$.

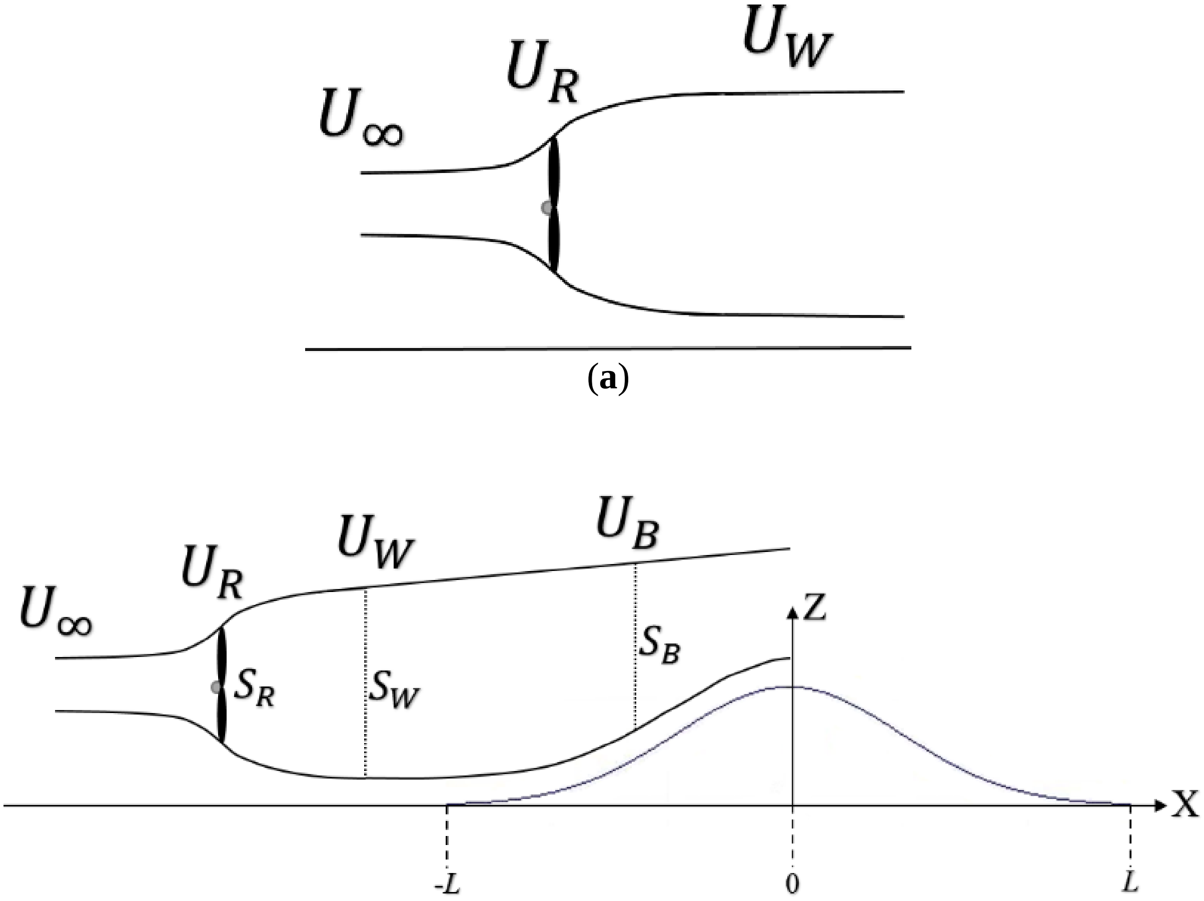

(**a**)

(**b**)

Figure 2.1(a) Wind turbine wake over a flat terrain; (b) The combined effect of both the turbine and the hill on the wind turbine wake.

Therefore, the net force that acts on the wind stream tube can be represented as follows:

$$\mathrm{T} = -\mathrm{m_B} + \mathrm{m_T} = \rho \mathrm{U_{B0}}^2 \mathrm{S_B} \nu_\mathrm{B} \left(1 - \frac{\nu_\mathrm{B}}{\sigma}\right) \tag{2.4}$$

Therefore the thrust coefficient calculated by the wake wind speed profile over the two-dimensional hill ($C_{T\,Hill}$) can be as follows:

$$C_{T\,Hill} = \frac{\rho \mathrm{U_{B0}}^2 \mathrm{S_B} \nu_\mathrm{B} \left(1 - \frac{\nu_\mathrm{B}}{\sigma}\right)}{\frac{1}{2} \rho \mathrm{U_\infty}^2 \mathrm{S_R}} = 2\sigma_0{}^2 \bar{\mathrm{S}} \nu_\mathrm{B} \left(1 - \frac{\nu_\mathrm{B}}{\sigma}\right) \tag{2.5}$$

where, $\sigma_0 = U_{B0}/U_\infty$, and $\bar{S} = S_B/S_R$.

2.2 Wake Development over a Two-Dimensional Hill

The rotor thrust can be represented as follows:

$$\mathrm{T} = \rho \mathrm{U}_{\infty}{}^{2} \mathrm{S}_{\mathrm{R}} \mu_{\mathrm{R}} (1 - \mu_{\mathrm{W}}) \tag{2.6}$$

where $\mu_R = U_R/U_\infty$, and $\mu_W = U_W/U_\infty$.

Therefore, from equations (2.4) and (2.6),

$$\bar{\mathrm{S}} = \frac{\nu_{\mathrm{R}}\left(1 - \frac{\sigma_0}{\sigma}\nu_{\mathrm{B}}\right)}{\sigma_0{}^{2}\nu_{\mathrm{B}}\left(1 - \frac{\nu_{\mathrm{B}}}{\sigma}\right)} \tag{2.7}$$

where, $\nu_R = U_R/U_{R0} = U_R/U_\infty$.

3 Wind Tunnel Test

In this chapter methods for the experimental studies are described. These include equipment such as: test facility, wind turbine model, and terrain model. The measurement methods used for forces and moments measurements, and flow velocity measurements are described. Finally, test conditions for several wind tunnel configurations are described.

3.1 Test Facility

The wind tunnel test was conducted in the Boundary Layer Wind Tunnel at the Research Institute of Applied Mechanics of Kyushu University [56]. The outline is shown in Figure 3.1. The wind tunnel has a closed test section of 15 m length, 3.6 m width, and 2.0 m height. A uniform flow with turbulence intensity less than 0.5 % can be achieved in this wind tunnel, and the maximum wind speed is 30 m/s. Wind tunnel top walls were removed at sections 3, 4, and 5 (Figure 3.1) so as to minimize wind tunnel blockage effects [57], [58].

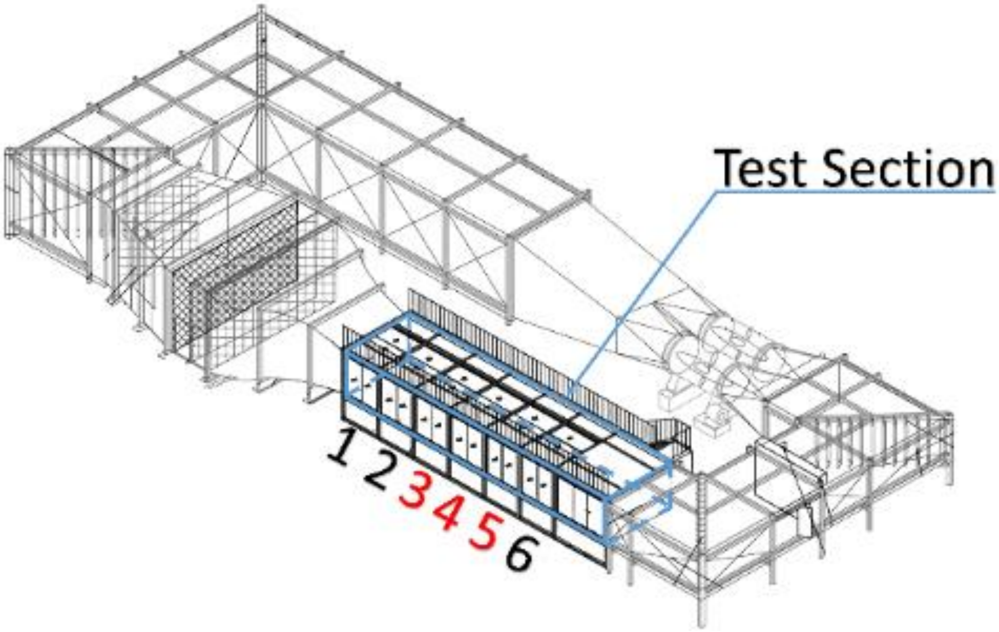

Figure 3.1 Boundary Layer Wind Tunnel [56], [58]

3.2 Wind Turbine Model

A three bladed Horizontal Axis Wind Turbine (HAWT) was used in the wind tunnel test as shown in Figure 3.2 (a). The turbine rotor diameter (*D*) was 0.512 m, and it was attached to an electric motor placed inside a nacelle. The blades of the wind turbine model were created using a 3D printer, and with the scale ratio of 1:175, the wind turbine test model would represent a wind turbine in a wind farm with a rotor diameter *D* equals to about 89.6 m and a hub height equals to about 89.6 m. The blade pitch angle of the wind turbine was fixed, and the wind turbine was maintained at a constant rotational speed. The rotational speed was set by the controller of the electric motor, and the rotor speed was measured by the built-in encoder. The nacelle was attached to a 6-component load cell (Figure 3.2 (b)) to measure the forces and moments acting on and around the turbine in X, Y, and Z axes. Then, the load cell was attached to a steel pipe that is hanged from the wind tunnel ceiling, and the steel pipe was streamlined using a streamline tube (Figure 3.2 (c)) to minimize the wake of the pipe.

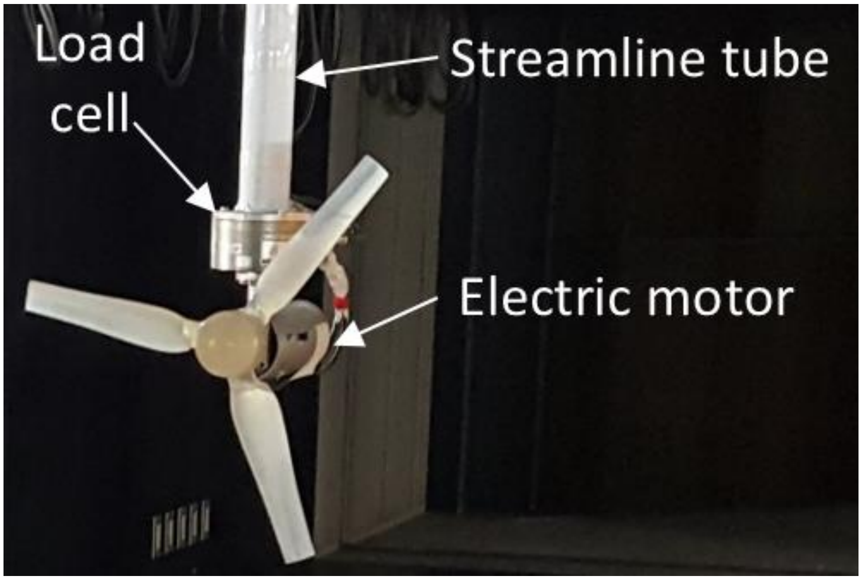

(a)

(**b**)

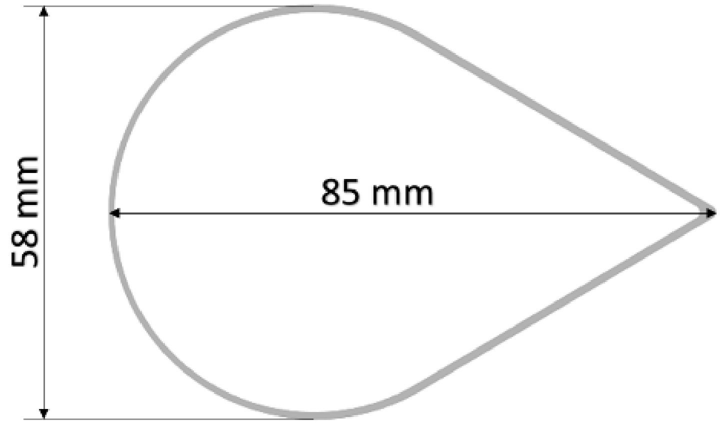

(**c**)

Figure 3.2 (a) Wind Turbine Model; (b) Load cell; (c) Streamline tube cross section.

3.3 Terrain Model

Figure 3.3 shows the two-dimensional hill model. The hill surface was smooth, and it was made of ABS resin. The height of the hill was *h* = 512 mm (same as the hub height) and its half-length *L* = 1560 mm long. The hill model was placed at about 0.12 m from wind tunnel floor so as to impose a uniform flow condition avoiding the boundary layer on the floor of the wind tunnel. The hill is represented by equation (3.1), where the slope of the hill *a* = 0.45. The two-dimensional hill model was created by using a wooden frame with a curve that is represented by equation (3.1), then the wooden frame was covered with a sheet made of ABS resin. With the scale ratio of 1:175, the terrain test model would represent a hill with the hill height *h* equals to about 89.6 m.

$$Z = h \exp\left[-\frac{1}{2}\left(\frac{X}{h/2.3548a}\right)^2\right] \tag{3.1}$$

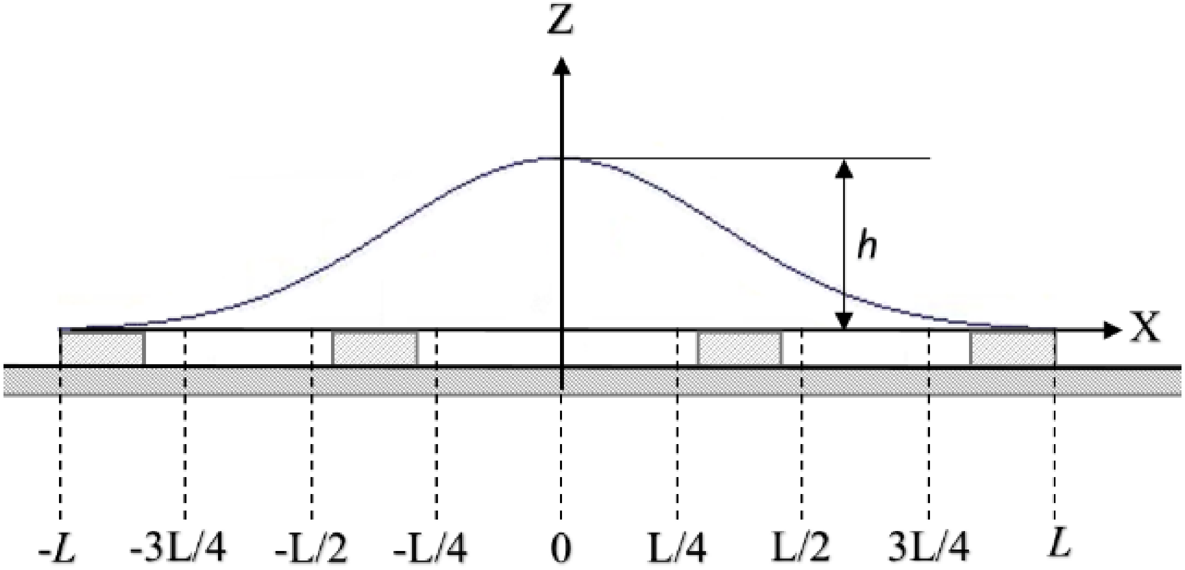

(a)

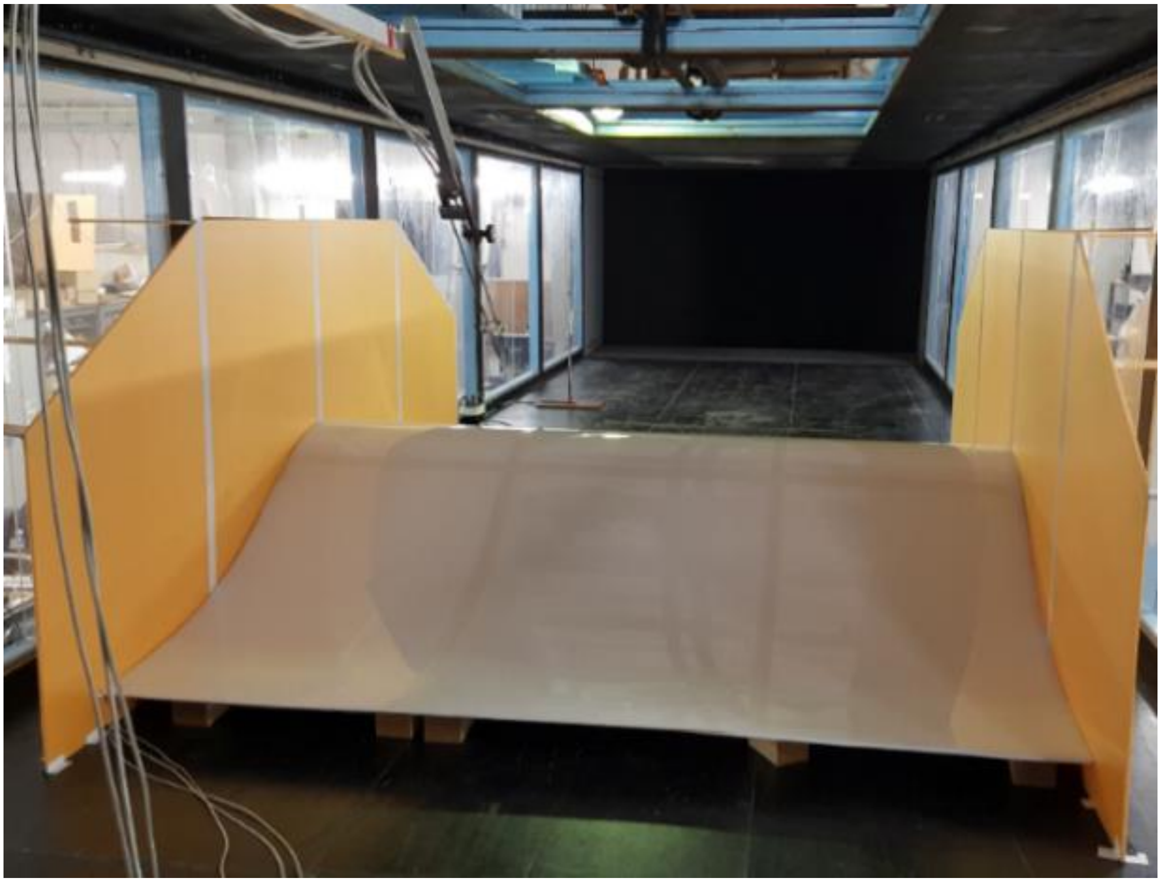

(b)

Figure 3.3 (a) Schematic diagram of the two-dimensional hill model; (b) Hill model used in the wind tunnel test.

3.4 Measurements

A hot wire anemometer (Figure 3.4) is often utilized to measure flow velocity in a wind tunnel. When the hot thin wire is placed perpendicular to the flow, the temperature of the thin wire changes. The change in temperature changes the wire resistance, and the flow velocity can be obtained by measuring the variation in resistance. The hot wire was mounted on a rod which was fixed to the traverse system of the wind tunnel. Wind speed profiles were measured using a standard straight hot wire anemometer at several locations over the hill with an increment of *L*/4 along the streamwise direction (Table 3.1), vertically along the Z-axis every 0.02 m, and horizontally along the Y-axis at the hub height every 0.02 m. The hot wire was fixed to the traverse system of the wind tunnel as shown in Figure 3.5. The flow velocity was measured with a sampling time of 30 seconds and a sampling frequency of 1 kHz.

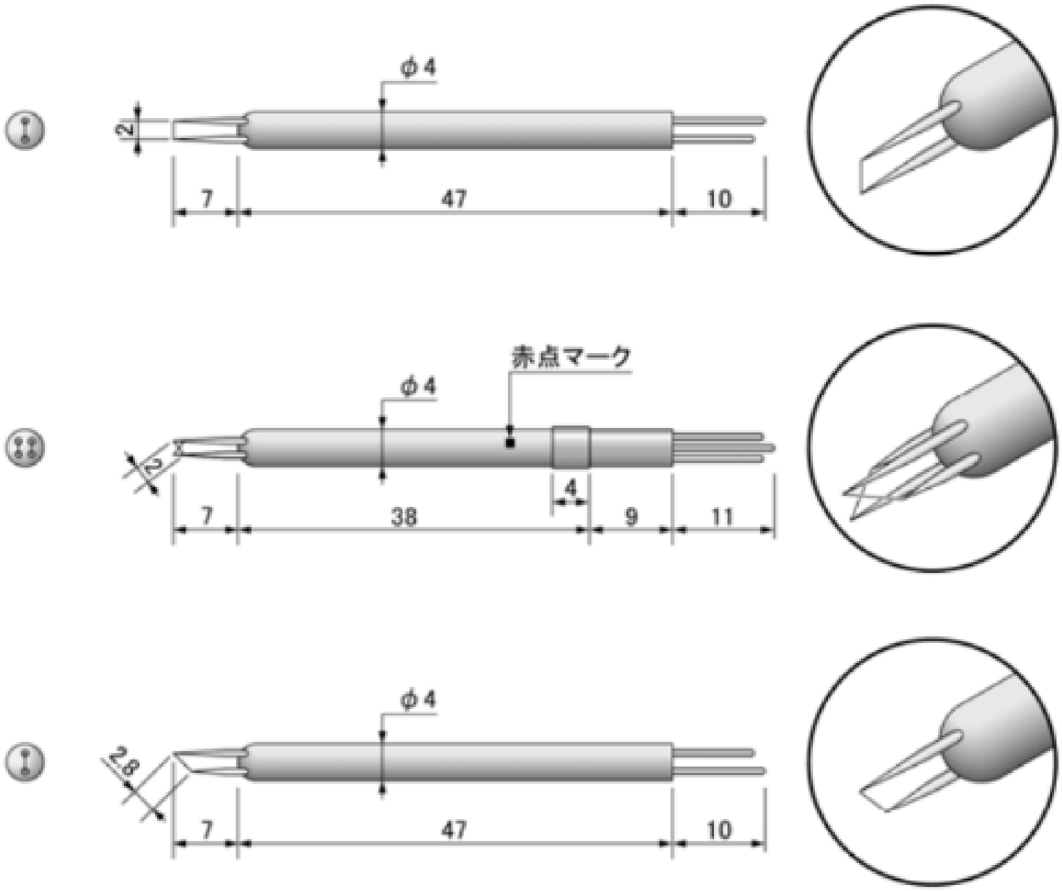

Figure 3.4 Different types of hot wire anemometers [59].

Table 3.1 Measurement locations of wind speed profiles along X-axis.

Location Number	*X* [mm]	*X/L*	Distance from Location 1
1	- 1560	-1	0
2	- 1170	-3/4	0.76 *D*
3	-780	-1/2	1.52 *D*
4	-390	-1/4	2.29 *D*
5	0	0	3.05 *D*
6	390	1/4	3.81 *D*
7	780	1/2	4.57 *D*
8	1170	3/4	5.33 *D*
9	1560	1	6.09 *D*

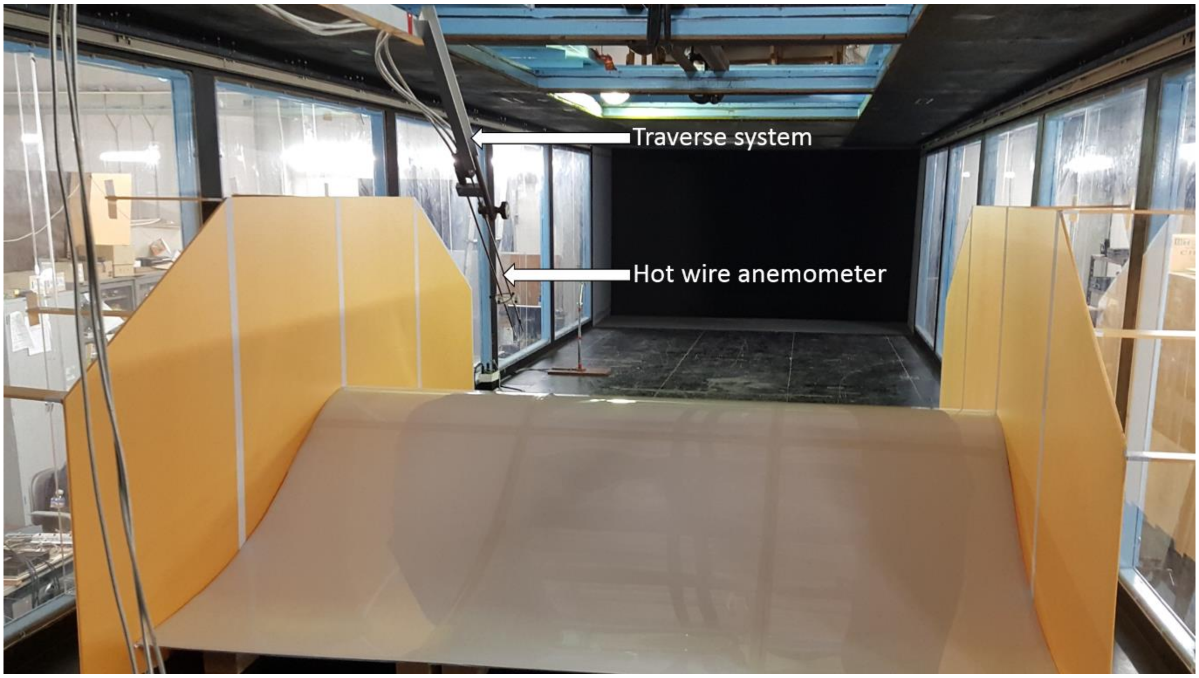

Figure 3.5 Wind velocity measurement setup.

The forces and moments acting on and around the turbine in X, Y, and Z axes were measured using a 6-component load cell (Figure 3.6) at several rotational speeds as shown in Table 3.2. Wind turbine rotor speed was set by the controller of the electric motor, and the rotor speed was measured by the built-in encoder. The Tip Speed Ratio (TSR; λ) can be defined as equation (3.2), where ω is the rotor speed in rad/s, R is the wind turbine radius in meters, and U is the wind velocity in m/s.

$$\lambda = \frac{\omega R}{U} \tag{3.2}$$

MULTI COMPONENT LOADCELL

MODEL	LMC-6566A-50N	
CAPACITY	Fx ±50N	Mx ±5N-m
	Fy ±50N	My ±5N-m
	Fz ±100N	Mz ±5N-m
SERIAL No.	13124	

NEW NISSHO ELECTRIC WORKS CO.,LTD.

Figure 3.6 Model number and capacity of the load cell [60].

Table 3.2 Wind turbine rotor speed.

rpm	Tip Speed Ratio (λ)
261	1.0
392	1.5
522	2.0
653	2.5
783	3.0
914	3.5
1044	4.0
1175	4.5
1306	5.0
1436	5.5
1567	6.0

3.5 Test Conditions

The test was conducted in three configurations A, B, and C as shown in Figure 3.7 and Figure 3.8. The inlet wind velocity was constant at 7 m/s for the three configurations. Wind speed profiles over the hill with no wind turbine are measured in configuration A. The wind speed profiles at the wake of a turbine placed at location 1 were measured in configuration B. Also, forces acting on turbine in X, Y, and Z axes as well as moments around X, Y, and Z axes were measured using a 6-component load cell in configuration B. The wind speed profiles at the wake of a turbine placed over a flat terrain were measured in configuration C to extract the terrain effects. The Tip Speed Ratio was $\lambda = 4$ for configurations B and C.

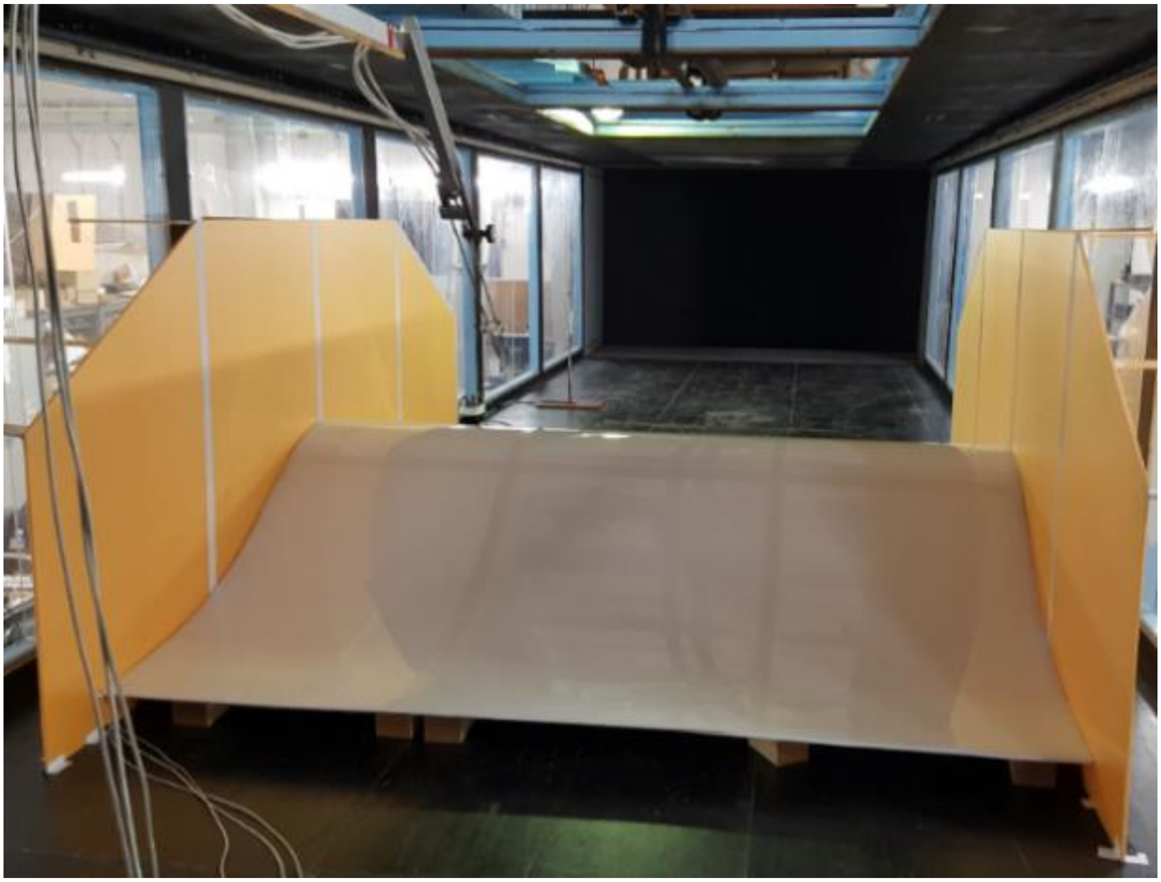

(a)

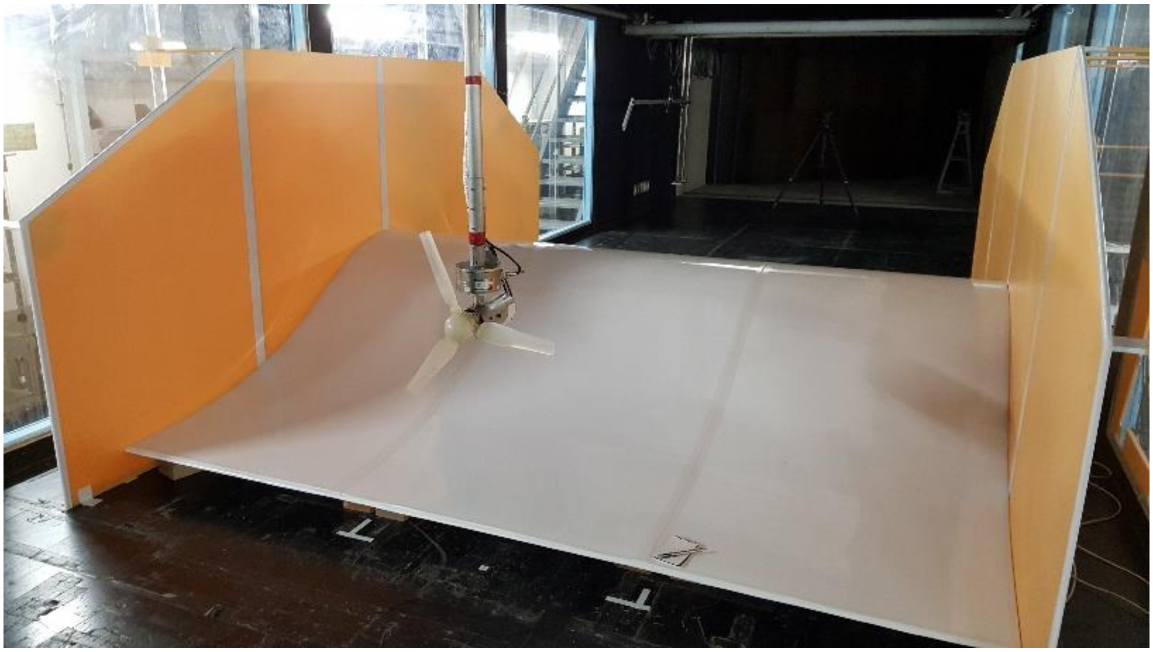

(b)

(c)

Figure 3.7 Measurement setup. (a) Configuration A: No wind turbine over the hill; (b) Configuration B: Wind turbine at –L over the hill; (c) Configuration C: Wind turbine at –L over the flat terrain.

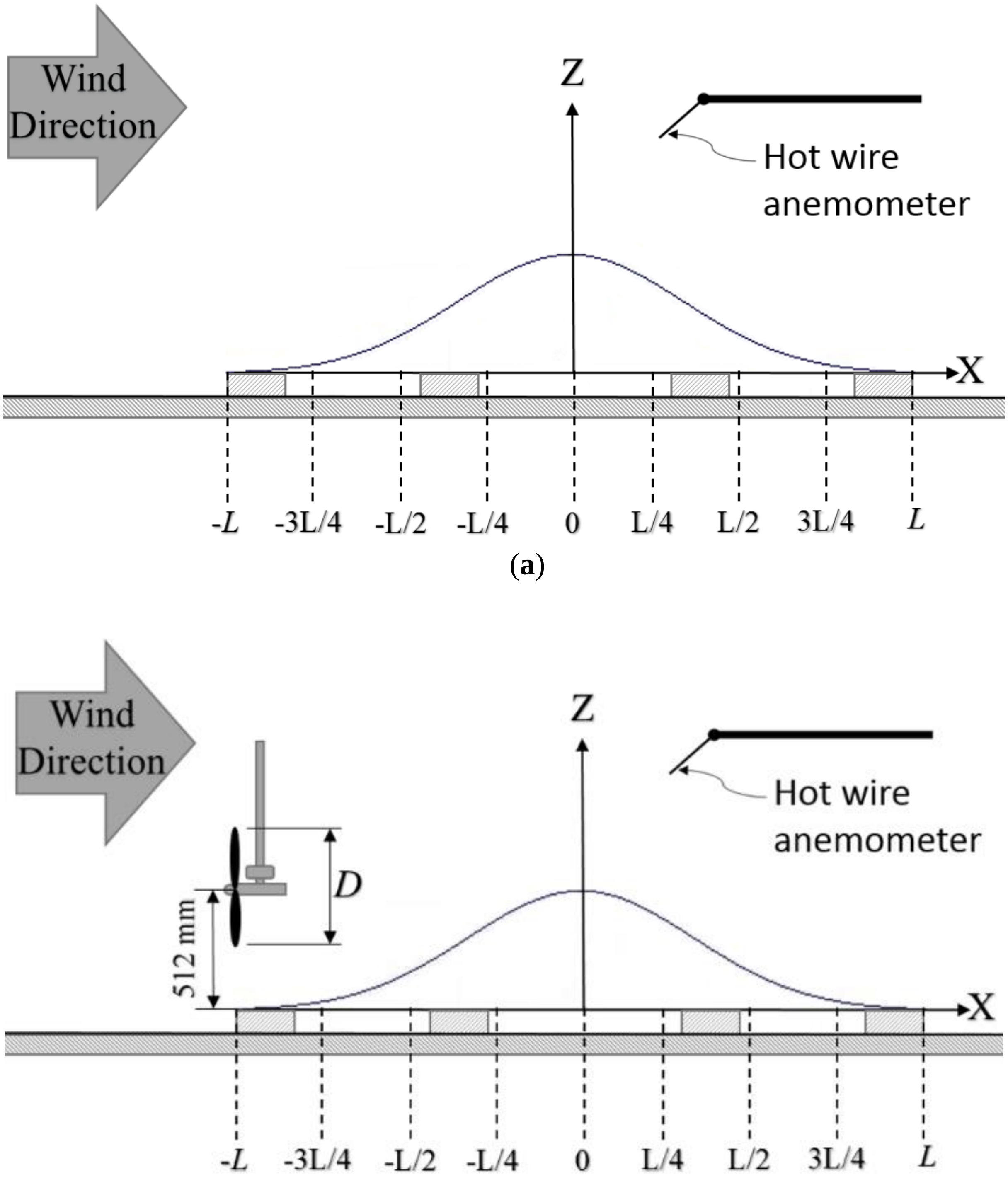
Wind Direction
Z
Hot wire anemometer
X
-L
-3L/4
-L/2
-L/4
0
L/4
L/2
3L/4
L
D
512 mm

(a)

(b)

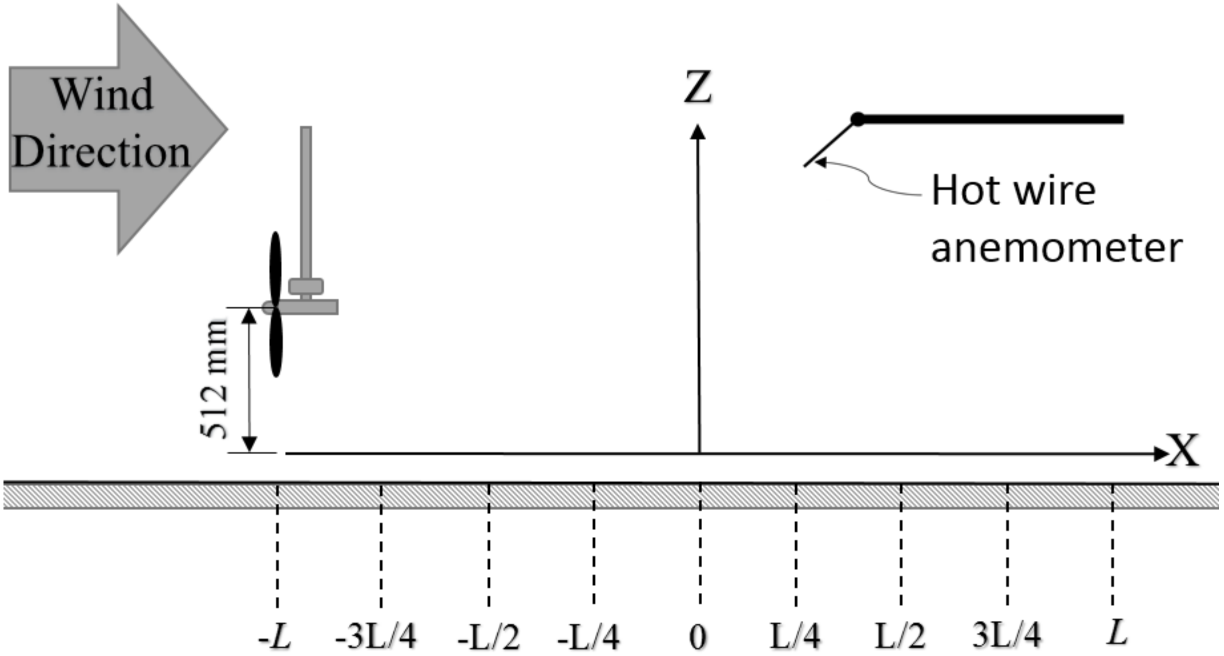

(**c**)

Figure 3.8 A schematic diagram of the measurement setup. (a) Configuration A: No wind turbine over the hill; (b) Configuration B: Wind turbine at –L over the hill; (c) Configuration C: Wind turbine at –L over the flat terrain.

4 Computational Fluid Dynamics

4.1 Wind Turbine Models

The wind turbine rotor could be modelled as a fully resolved rotor (by building a rotor body fitted mesh, as shown in Figure 4.1), or an actuator disk or an actuator line (Figure 4.2) [12]. Modelling the fully resolved rotor [61] [62] [63] [64] [65] [66] [67] [68] [69] is an accurate way for simulating air flow around the rotor, but, it has the highest computational cost. The actuator disk method [45] [44] [70] [71] [72] doesn't require the creation of the turbine rotor's body fitted mesh, however, the force applied by the actuator disk on the flow is added to the momentum equation. The actuator disk method is simpler than the fully resolved rotor method and has a lower computational cost. The actuator line method [73] doesn't need the creation of the body fitted mesh, but the turbine blades are replaced by forces acting on rotating lines, as shown in Figure 4.2.

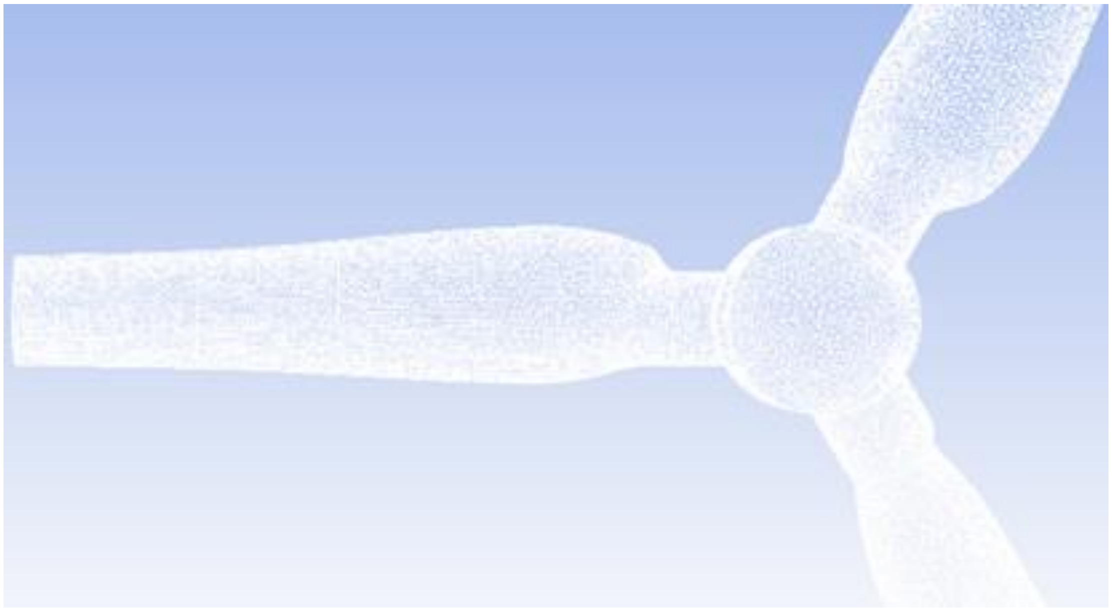

Figure 4.1 Surface mesh of a fully resolved wind turbine rotor.

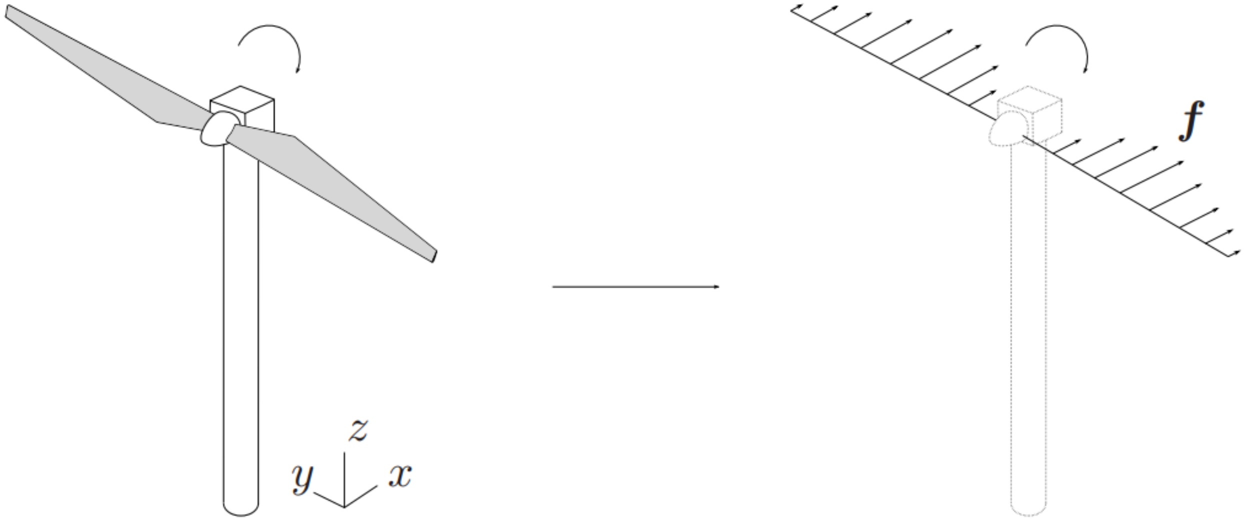

Figure 4.2 Actuator Line method [12].

4.2 CFD simulation cases

4.2.1 Case 1: Flow over a Two-Dimensional Hill

k–ε turbulence model was previously used for simulating flow over terrain and other applications [74] [75] [76]. However, using this method results in average turbulent kinetic energy and average wind speed [77]. Alternatively, Large Eddy Simulation (LES) model was previously used [53] [78] [79] for wind flow simulation over terrain, and was able to show flow unsteadiness. Therefore, the LES model was used in this paper for flow simulation over the steep 2D hill, and the standard Smagorinsky model [80] was used as the subgrid-scale (SGS) model.

The flow over the hill was simulated using Ansys Fluent [81] where a transient pressure-based solver was used to obtain the average vertical wind speed profiles along the hill.

Computational domain was as shown in Figure 4.3. It had the same dimensions as the wind tunnel, and the boundary conditions were as follows: Outlet was set to pressure-outlet with an operating pressure of 101,325 Pascals and a gauge pressure equals to zero. Inlet was set to velocity-inlet type at a constant velocity of 7m/s, and a uniform approach-flow with turbulence intensity less than 0.5 % was used. The hill was set to no-slip condition. The ceiling windows were set at atmospheric pressure (101,325 Pascals), and a no-slip condition was employed for side walls.

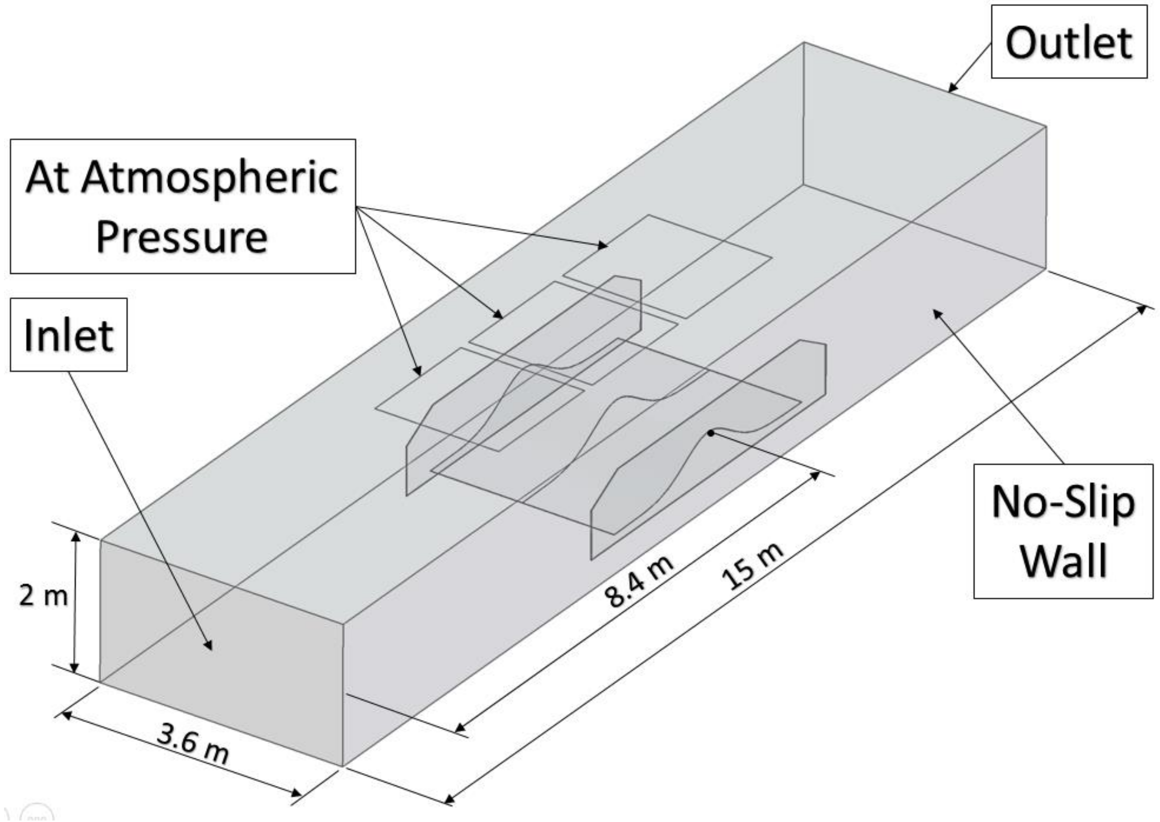

Figure 4.3 Computational domain of Case 1.

An unstructured mesh was created using Ansys Meshing. Prismatic volume cells were generated on hill surface with a growth rate of 1.2, as shown in Figure 4.4, and the first layer thickness was specified in order for y+ to be less than 1, where y^+ is a non-dimensional distance, and can be defined by equation 4.1. Where y is the distance to the closest wall, u_τ is the friction velocity, and ν is the kinematic viscosity.

$$y^+ = \frac{y\, u_\tau}{\nu} \tag{4.1}$$

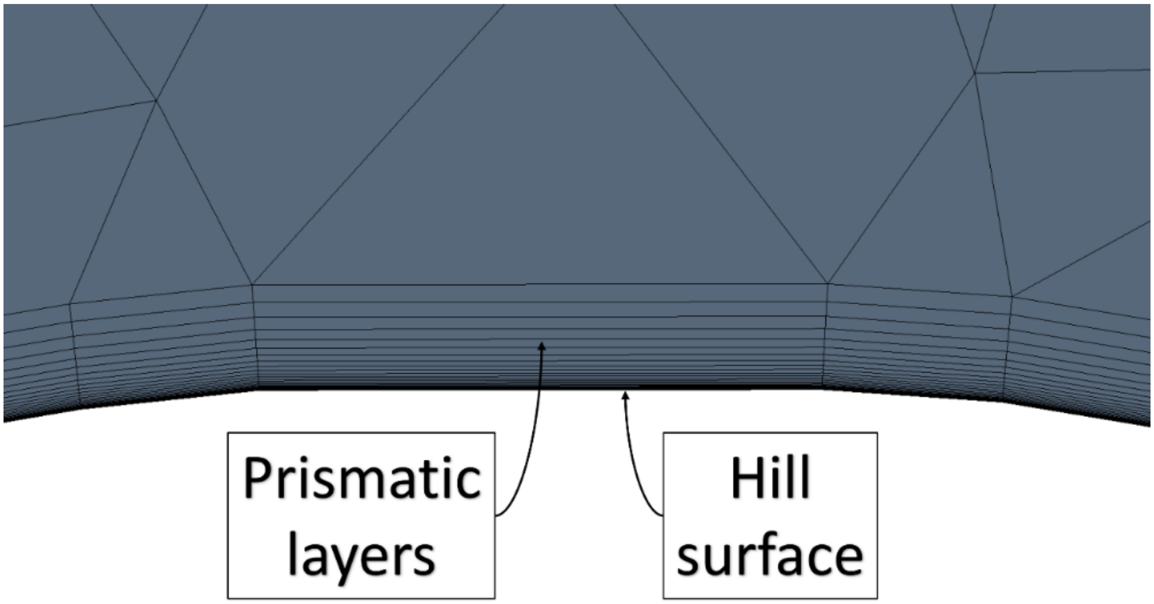

Figure 4.4 Prismatic layers were generated on the hill surface.

4.2.2 Case 2: Flow around a Wind Turbine

Transition Shear Stress Transport (SST) model (also called the γ - Re_{θ} model) was used in this paper. The transition SST model combines the transport equations of the SST k-ω and two more equations [82] [83] [84] [85] [86]. The Transition SST model is based on three local correlation parameters $Re_{\theta c}$, $Re_{\theta t}$, and F_{Length}. $Re_{\theta c}$ is the Critical momentum thickness Reynolds number, $Re_{\theta t}$ is the Transition onset momentum thickness Reynolds number, and F_{Length} is an empirical correlation that controls the laminar-turbulent transition region length. These three parameters were optimized as described in the work of Sørensen [86]. $Re_{\theta c}$ and F_{Length} were specified, then a number of simulation runs were done to get the optimum values for $Re_{\theta c}$ and F_{Length}. Then a second series of simulation runs were done to get the optimum value for third correlation parameter $Re_{\theta t}$.

Flow around wind turbine rotor was simulated using Ansys Fluent where a steady state solver was used for investigating wind turbine performance at different inlet wind velocity profiles.

For this case, a fully resolved rotor was used in CFD simulations as shown in Figure 4.5. An unstructured mesh that satisfies the Transition SST model limitations [82] [83] [84] [85] [86] was created using Ansys Meshing. Prismatic volume cells were generated on the wind turbine rotor surface with a growth rate less than 1.1, as shown in Figure 4.6, and the first layer thickness was specified in order for y+ to be less than 1. The total number of cells was about 7.6 million cells.

Figure 4.5 Surface mesh of the fully resolved wind turbine rotor.

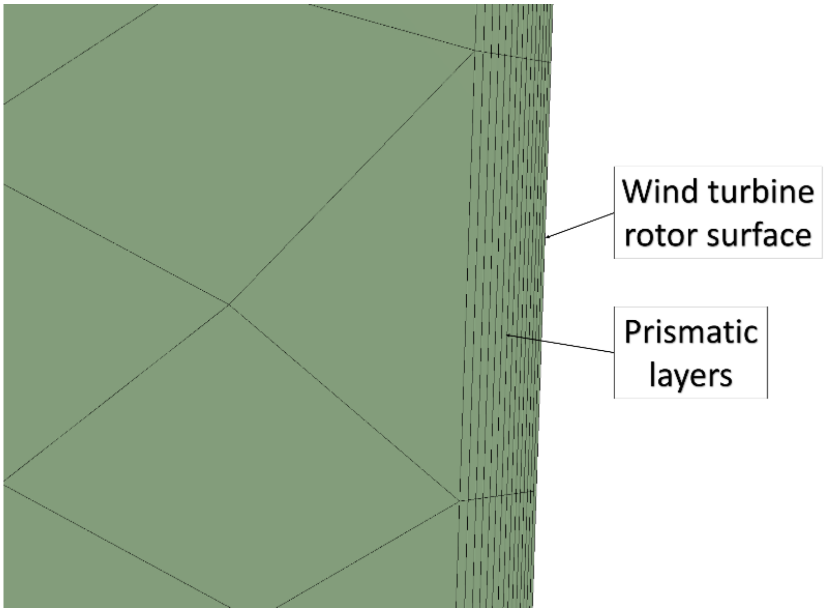

Figure 4.6 Prismatic layers were generated on turbine rotor surface.

The computational domain was as shown in Figure 4.7. The hill body was not included in this case, however, the hill effect was included in the inlet boundary condition.

Boundary conditions were as follows: Pressure-outlet condition was used for the outlet with an operating pressure of 101,325 Pascals and a gauge pressure equals to zero. Velocity-inlet condition was used for the inlet, and it had the same wind velocity profile as the wind tunnel test measurements. The rotor was set to no-slip condition, and the outer cylinder wall was set to symmetry type.

To simulate the rotation of the wind turbine rotor, moving reference frame was used where an axis of rotation, origin of axis of rotation, and rotational velocity were specified.

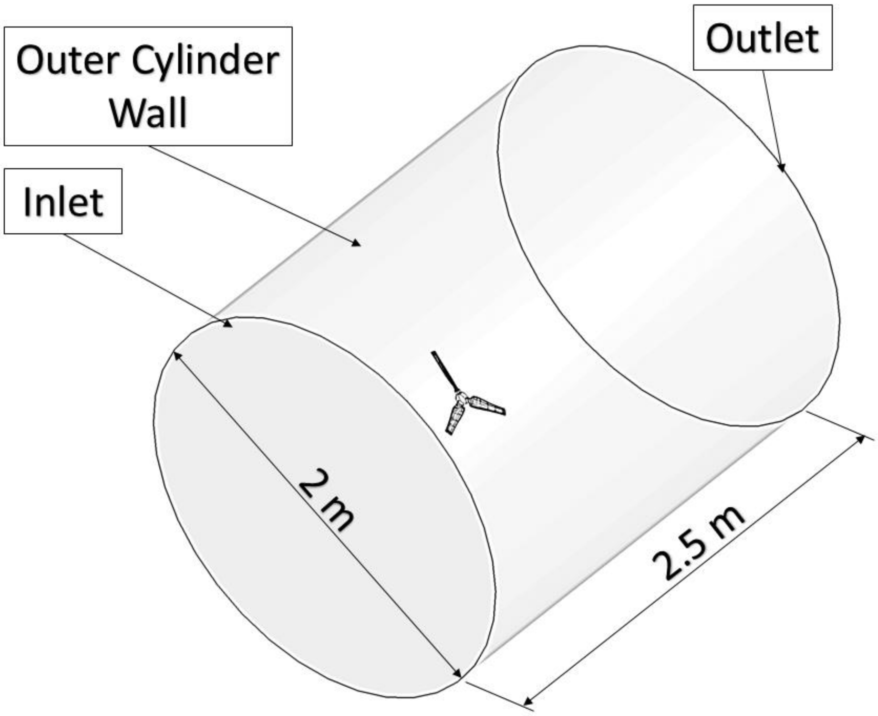

Figure 4.7 Computational domain of case 2.

4.2.3 Case 3: Wind Turbine Wake Development over Flat Terrain

The LES model was used in this case to investigate wind turbine wake development over flat terrain, and the standard Smagorinsky model was used as the SGS model. Wake development over the flat terrain was simulated using OpenFOAM [87], where a transient solver was used.

A fully resolved wind turbine rotor was used in this CFD case as shown in Figure 4.8, where the rotor diameter $D = 0.512$ m. A moving reference frame was used to simulate the rotation of the wind turbine rotor, where the axis of rotation, origin of axis of rotation, and rotational velocity were specified. The Tip Speed Ratio was $\lambda = 4$, because it is the optimum λ for this turbine.

Figure 4.8 Wind turbine model used for case 3.

Computational domain was as shown in Figure 4.9. Boundary conditions were as follows: The inlet was set to uniform flow, and the inlet velocity was constant at U_{inlet}= 7 m/s, and a uniform approach-flow with turbulence intensity less than 0.5 % was used. A slip condition was used for upper, lower, and side walls. An unstructured mesh was created for the rotor. Cells were generated on the rotor surface with a growth rate of about 1.2, and the first layer thickness was specified in order for y+ to be less than 1, where y^+ is a non-dimensional distance, and can be defined by equation (4.1). The total number of cells was about 12 million cells.

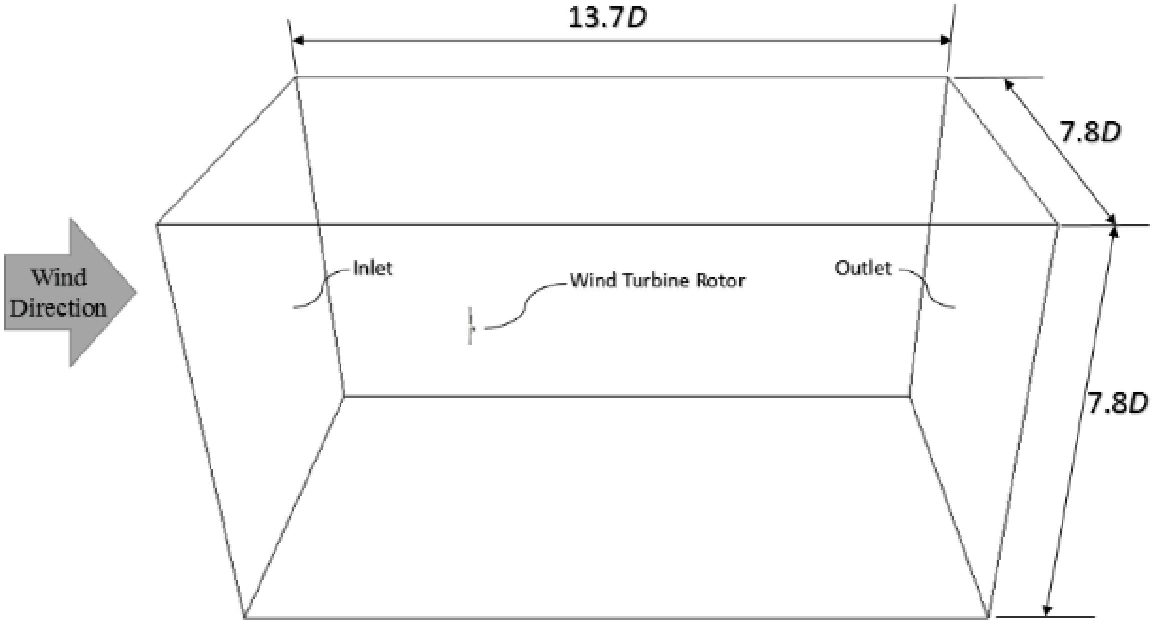

Figure 4.9 Computational Domain of Case 3.

4.2.4 Case 4: Wake development of a Wind Turbine Located at the Top of a Hill

The LES model was used in this study to investigate wake development of a wind turbine located at the top of a two-dimensional hill, and the standard Smagorinsky model was used as the SGS model. Wake development over the hill was simulated using OpenFOAM, where a transient solver was used. The hill is represented by equation (3.1), where the slope of the hill $a = 0.45$, the height of the hill is $h = 0.1$ m (same as the hub height) and half-length of hill $L = 3D$ as shown in Figure 4.10.

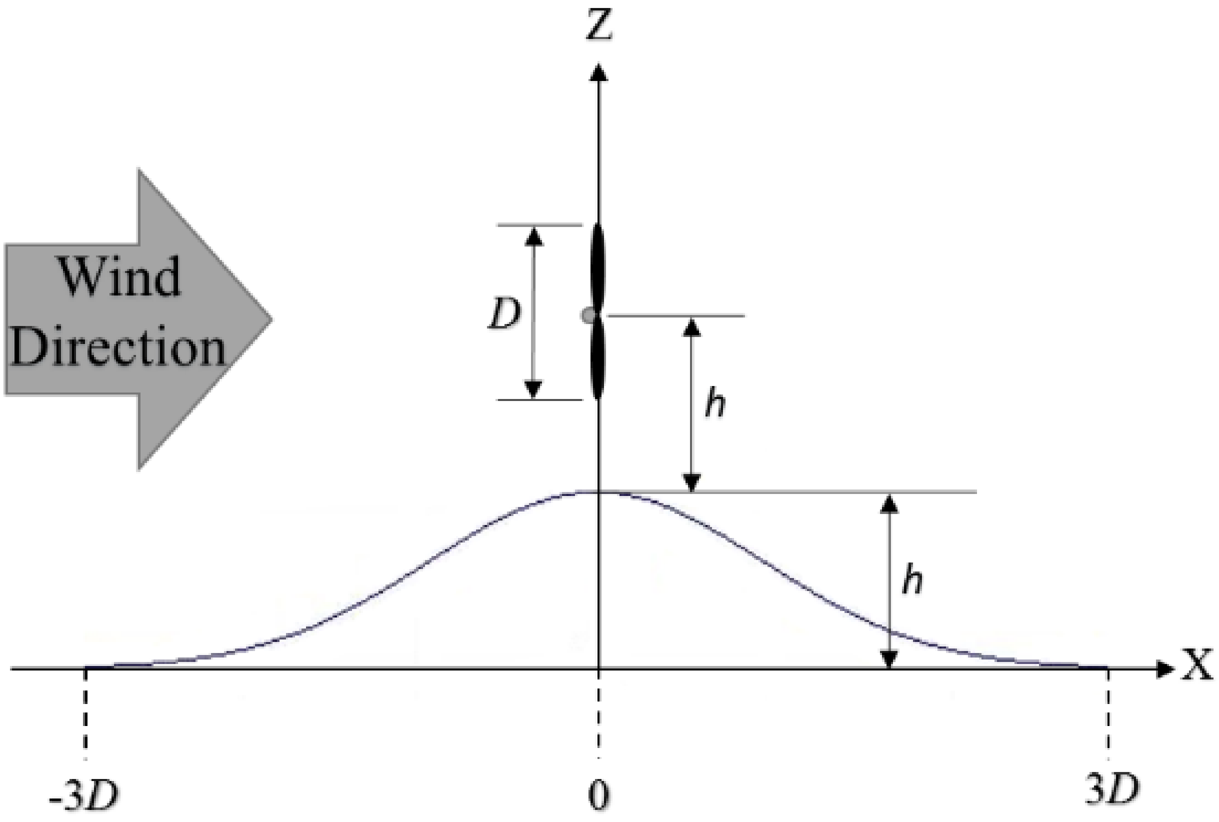

Figure 4.10 A schematic diagram of Case 4.

A fully resolved wind turbine rotor was used in the CFD simulation as shown in Figure 4.11, where the rotor diameter $D = 0.1$ m. The rotor was placed at the top of the hill, as shown in Figure 4.10. A moving reference frame was used to simulate the rotation of the wind turbine rotor, where the axis of rotation, origin of axis of rotation, and rotational velocity were specified. The Tip Speed Ratio was $\lambda = 4$, because it is the optimum λ for this turbine.

Figure 4.11 The fully resolved wind turbine rotor used for Case 4.

Computational domain was as shown in Figure 4.12. Boundary conditions were as follows: The inlet was set to uniform flow, and the inlet velocity was constant at U_{inlet}= 7 m/s, and a uniform approach-flow with turbulence intensity less than 0.5 % was used. The hill was set to no-slip condition, and a slip condition was used for upper and side walls. A slip condition was used for the floor from the inlet boundary to 17D (as shown in Figure 4.12) so as to impose a uniform flow condition, and a no-slip condition was used for the rest of the floor as shown in Figure 4.12. An unstructured mesh was created for the hill and rotor. Cells were generated on hill and rotor surfaces with a growth rate of about 1.2, and the first layer thickness was specified in order for y+ to be less than 1, where y^+ is a non-dimensional distance, and can be defined by equation (4.1).

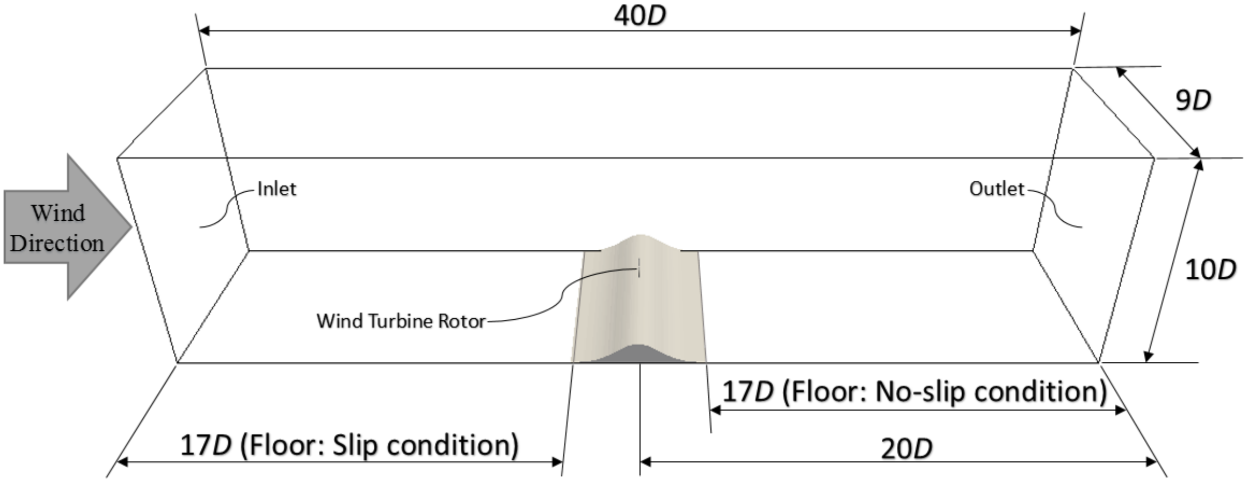

Figure 4.12 Computational Domain of Case 4.

4.2.5 Case 5: Wind Turbine Wake Development over a Two-Dimensional Hill

CFD was used in this case to investigate far-wake development in accelerating wind field over a hill, which was difficult to do in the wind tunnel due to the size limitations of the wind tunnel test section. In the wind tunnel, the hill model couldn't be made bigger due to the blockage effect, and the wind turbine rotor couldn't be made smaller due to the difficulty of manufacturing small diameter blades for the wind turbine model. Furthermore, smaller wind turbines wouldn’t be stable at higher wind speeds in the wind tunnel.

The LES model was used in this study to investigate wake development in accelerating wind field over a two-dimensional hill, and the standard Smagorinsky model was used as the SGS model. Wake development over the hill was simulated using OpenFOAM, where a transient solver was used to investigate far-wake development in accelerating wind field. The hill is represented by equation (3.1), where the slope of the hill $a = 0.45$, the height of the hill is $h = 0.1$ m (same as the hub height) and half-length of hill $L = 3D$ as shown in Figure 4.13.

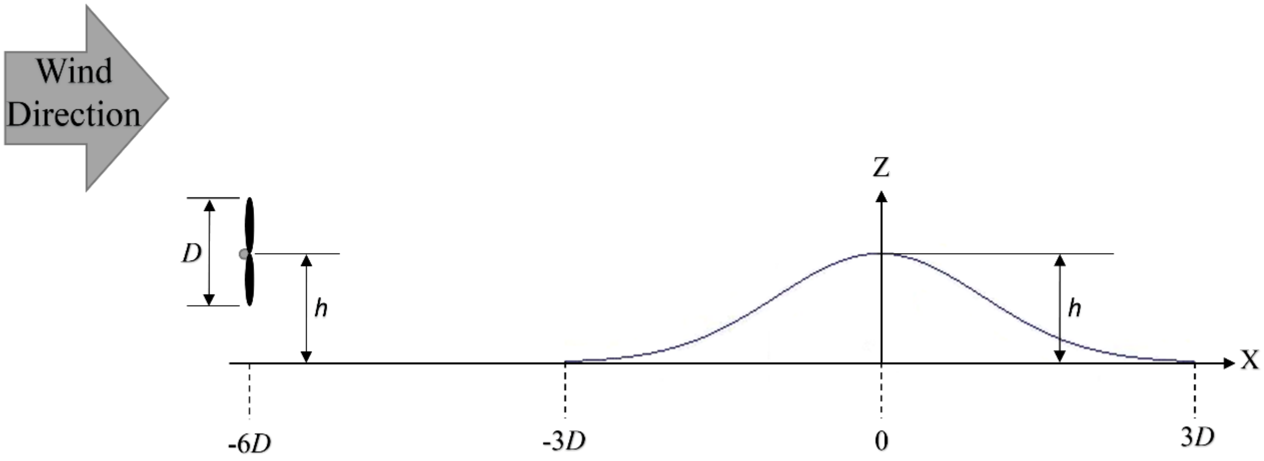

Figure 4.13 A schematic diagram of Case 5.

A fully resolved wind turbine rotor was used in the CFD simulation as shown in Figure 4.14, where the rotor diameter D = 0.1 m. The rotor was placed at a distance of 6D away from the hill center, as shown in Figure 4.13. A moving reference frame was used to simulate the rotation of the wind turbine rotor, where the axis of rotation, origin of axis of rotation, and rotational velocity were specified. The Tip Speed Ratio was λ = 4, because it is the optimum λ for this turbine.

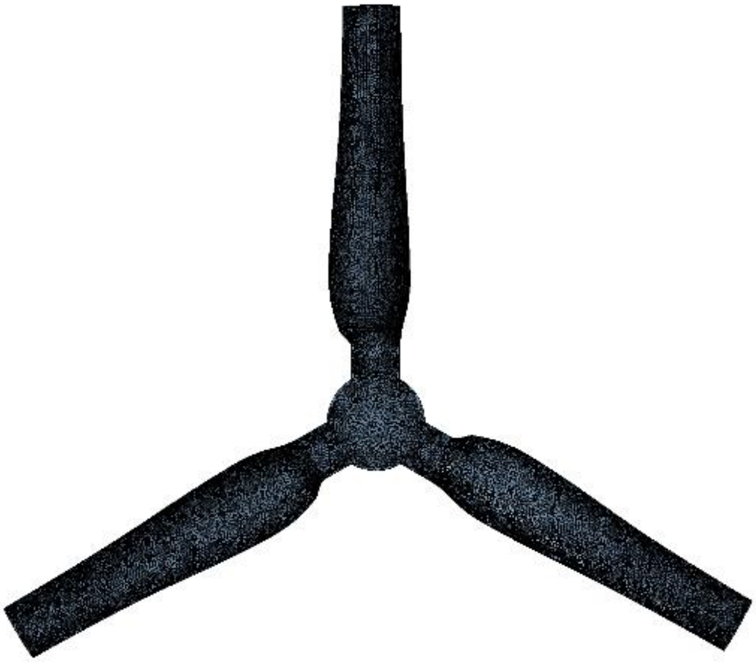

Figure 4.14 The fully resolved wind turbine rotor used for Case 5.

Computational domain was as shown in Figure 4.15. Boundary conditions were as follows: The inlet was set to uniform flow, and the inlet velocity was constant at U_{inlet}= 7 m/s, and a uniform approach-flow with turbulence intensity less than 0.5 % was used. The hill was set to no-slip condition, and a slip condition was used for upper and side walls. A slip condition was used for the floor from the inlet boundary to 17D (as shown in Figure 4.15) so as to impose a uniform flow condition, and a no-slip condition was used for the rest of the floor as shown in Figure 4.15.

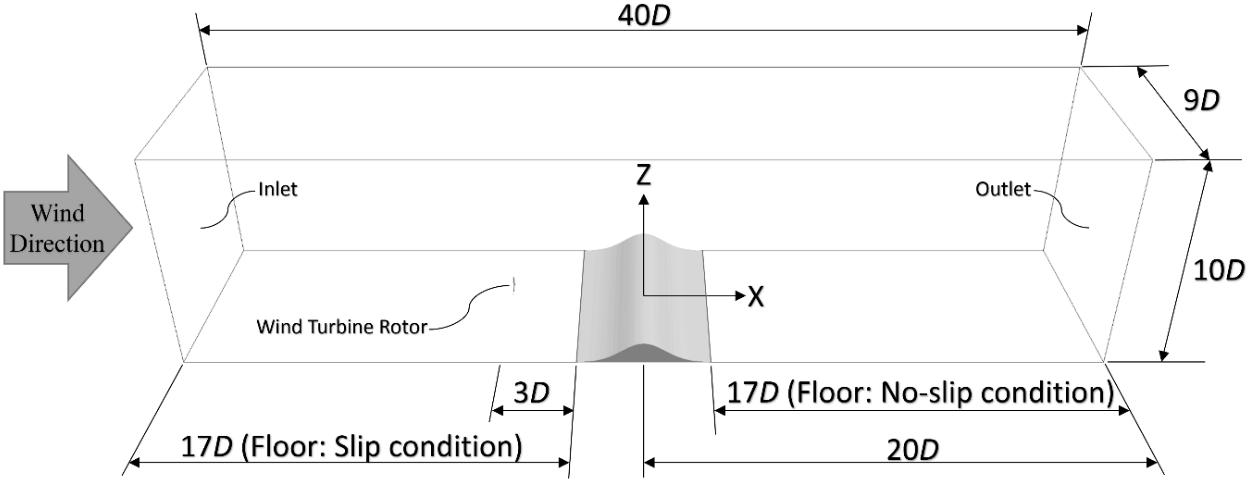

Figure 4.15 Computational Domain of Case 5.

An unstructured mesh was created for the hill and rotor. Cells were generated on hill and rotor surfaces with a growth rate of about 1.2, and the first layer thickness was specified in order for y+ to be less than 1, where y^+ is a non-dimensional distance, and can be defined by equation (4.1). The total number of cells was about 27 million cells.

5 Results and Discussion

5.1 Wind Tunnel Test Results

5.1.1 Wind Speed profiles over the Two-Dimensional Hill

Figure 5.1 shows the vertical wind speed profiles over the hill at locations 1 to 6 without a wind turbine. In Figure 5.1, the horizontal axis is normalized by $U_{h1} = 6.21\ m/s$, where U_{h1} is the hub height wind speed at *X* = -*L*. The vertical axis is normalized by the hill height h, and z* indicates the height from the hill surface. Wind velocity is almost constant at *X* = - *L*, afterwards, wind velocity starts to increase at *X* = -*L/2* until it reaches the maximum wind speed at *X* = *0*, then starts to decrease at the downstream of the hill at *X* = *L/4*.

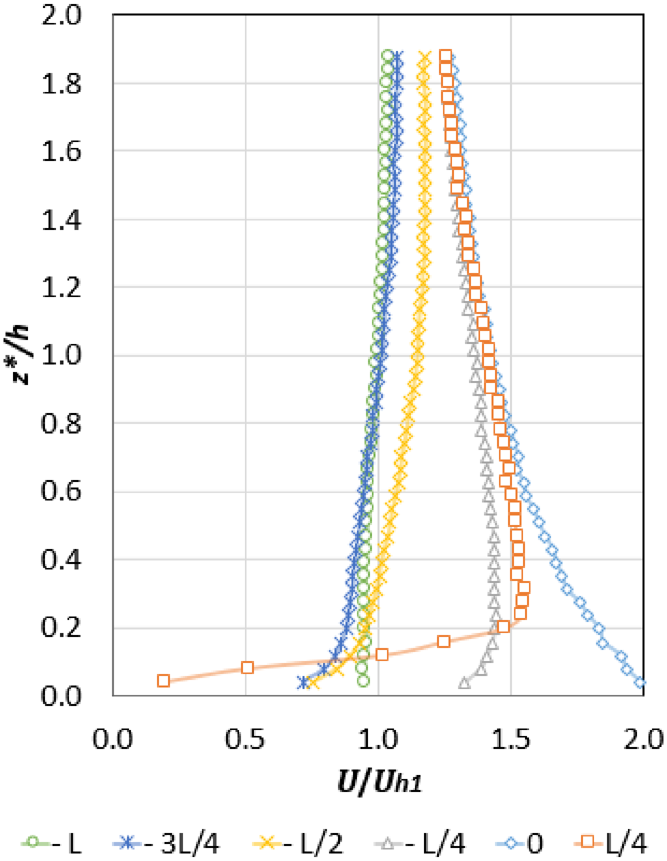

Figure 5.1 Configuration A: vertical wind speed profiles over locations 1 to 6.

5.1.2 Wake over the Two-Dimensional Hill

The power coefficient (C_P) and the thrust coefficient (C_T) were calculated using load cell measurements over a flat terrain as shown in Figure 5.2 and Figure 5.3. Figure 5.4 to Figure 5.7 show the average vertical and horizontal wind speed profiles at several distances downstream of the turbine for the configuration B. In Figure 5.5 and Figure 5.7, the horizontal axis is normalized by wind turbine radius R = 0.256 m. Wind speed profiles were measured at *-L/2, -L/4, 0, L/4, L/2,* and *L*.

The wake width (D_{wake}) was determined using an arbitrary threshold that the wind speed must be greater than or equal $0.9U_{B0}$ to be regarded as the wake edges.

Figure 5.4 and Figure 5.5 show the wind turbine wake development upstream of the hill. At 1.52 *D* (*X*= *-L/2*), the wake width was about 0.52 m, and by the time the wake reached 3.05 *D* at the top of the hill (*X* = *0*), the wake width has decreased to about 0.15 m. This means that the hill has caused the wake to accelerate and shrink upstream of the hill.

However, as the wake reaches 3.81 *D* (*X* = *L/4*) it started to expand and the wake width was about 0.50 m, and by the time the wake reached 6.09 *D* (*X* = *L*), the wake width has increased to about 0.56 m. This means that the hill has caused the wake to decelerate and expand downstream of the hill.

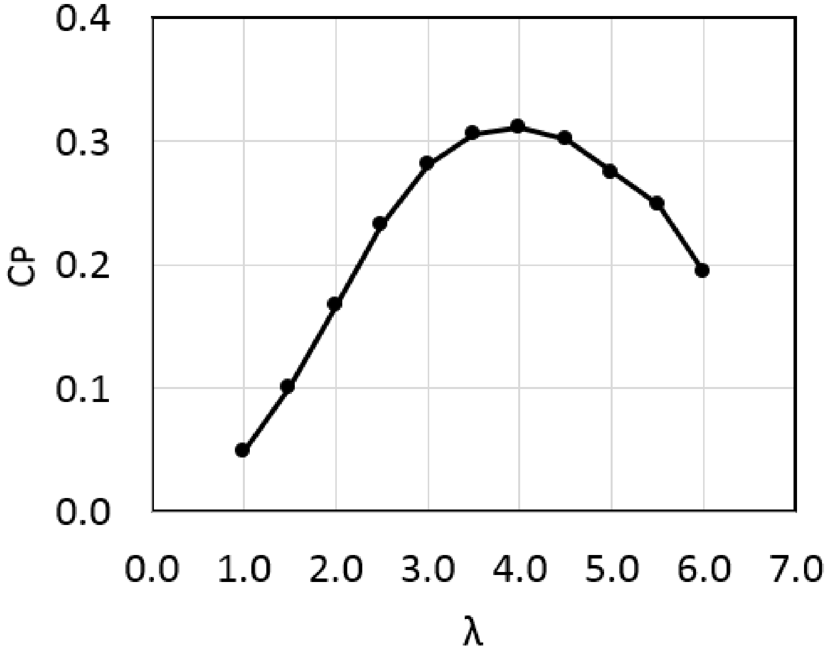

Figure 5.2 Wind turbine power coefficient over a flat terrain.

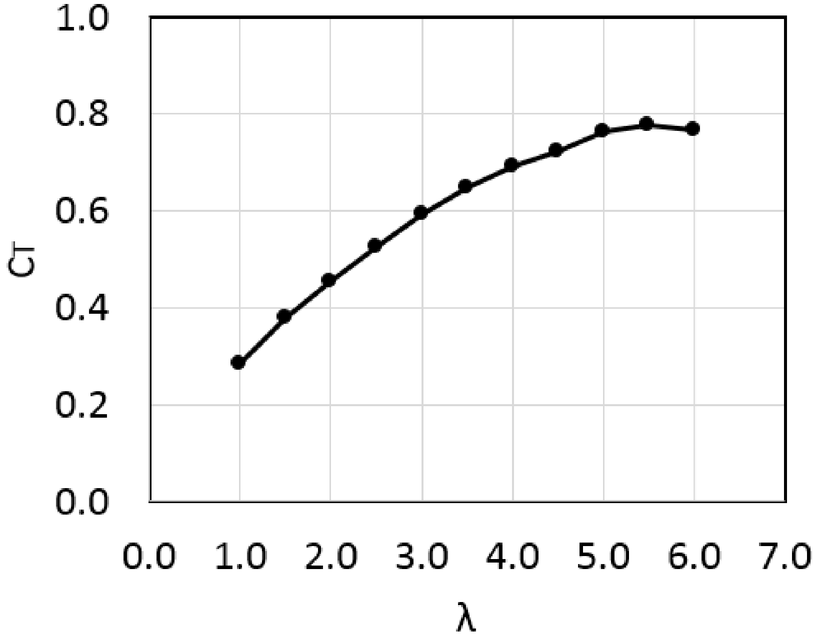

Figure 5.3 Wind turbine thrust coefficient over a flat terrain.

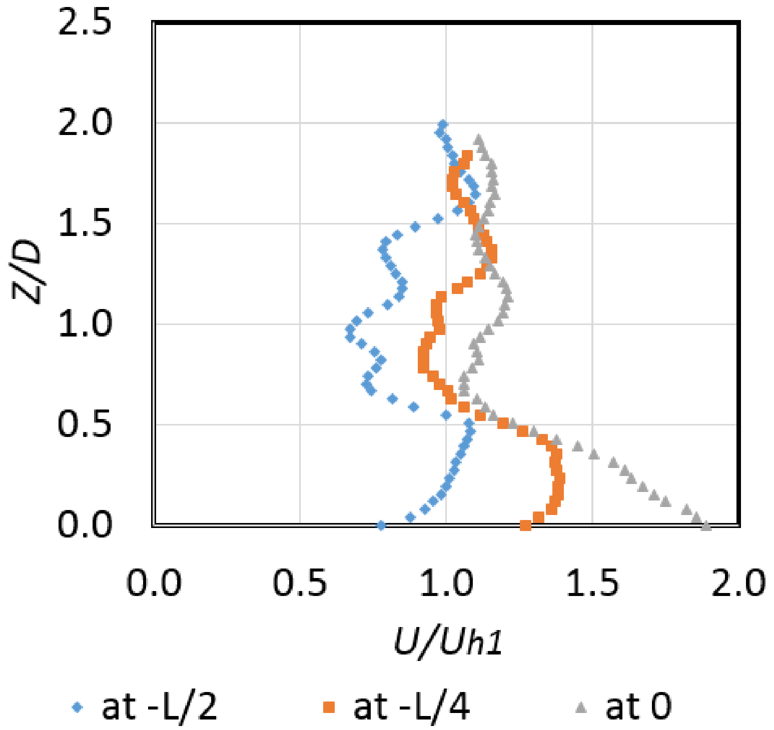

Figure 5.4 Configuration B: vertical wind speed profiles upstream of the hill.

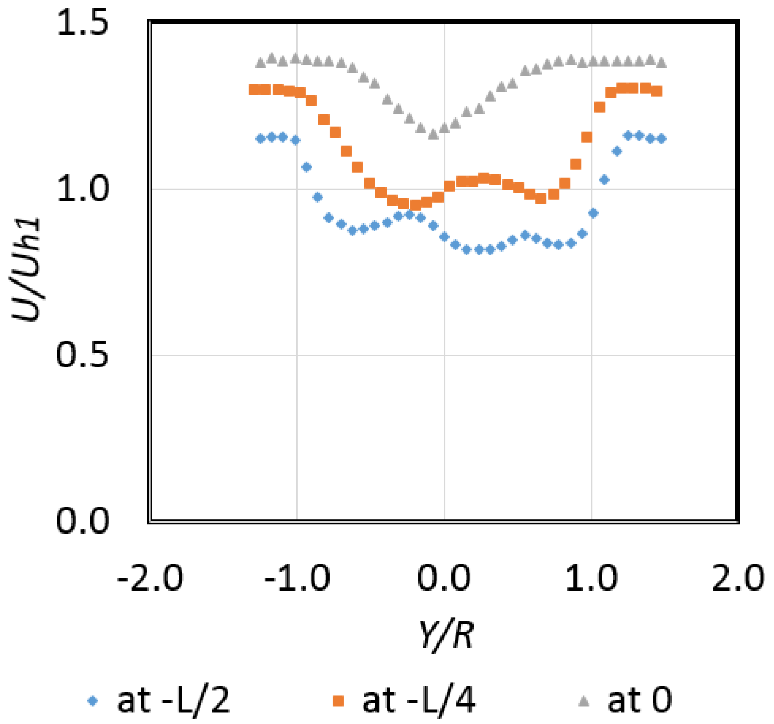

Figure 5.5 Configuration B: horizontal wind speed profiles upstream of the hill.

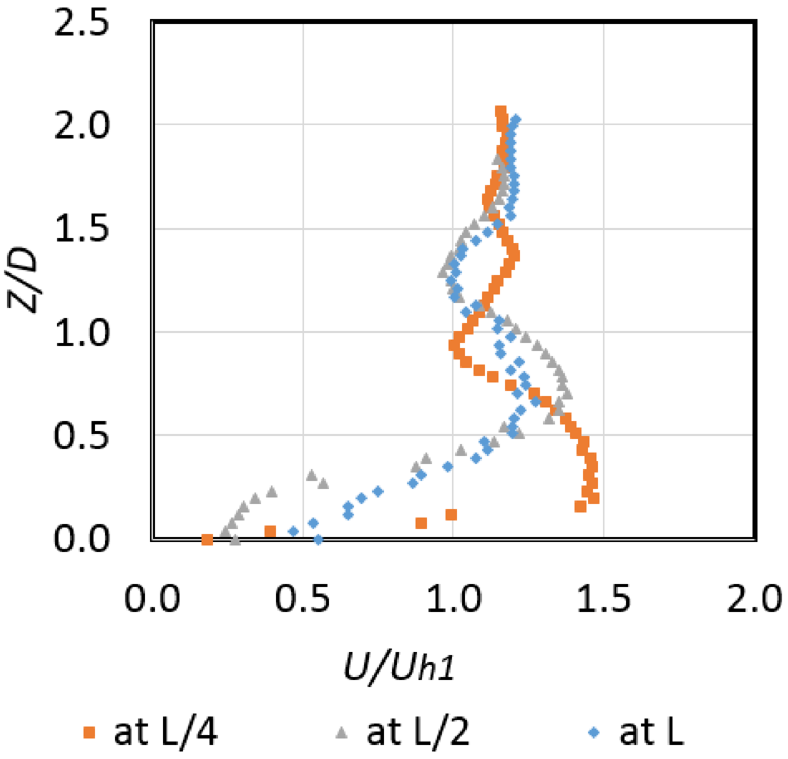

Figure 5.6 Configuration B: vertical wind speed profiles downstream of the hill.

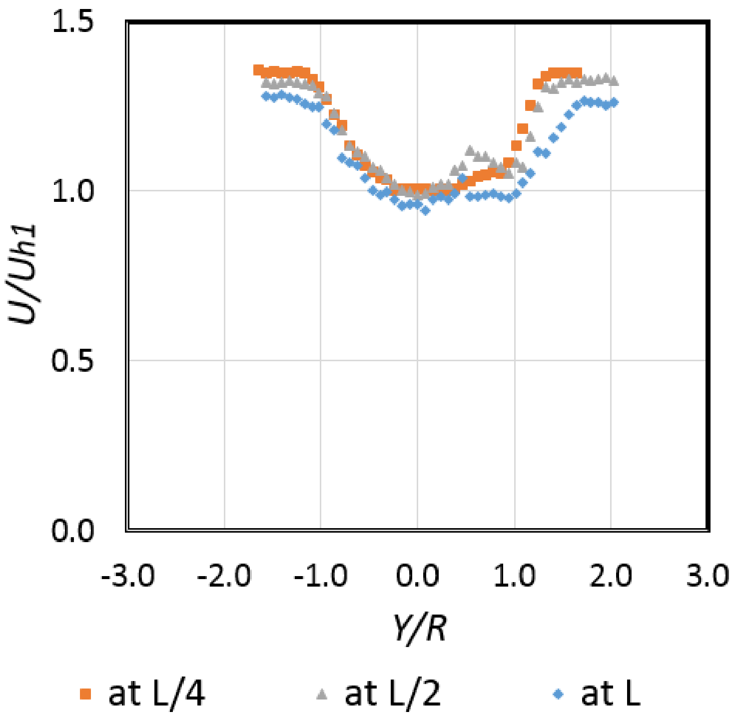

Figure 5.7 Configuration B: horizontal wind speed profiles downstream of the hill.

5.1.3 Wake Development over Hill versus Flat Terrain

Figure 5.8 and Figure 5.9 compare between wake development over hill (configuration B) and wake development over flat terrain (configuration C) at 3.05 D and 6.09 D respectively. The hill had an effect on both the velocity deficit and the wake width at the top and downstream of the hill. At 3.05 D, the velocity deficit over hill was about 0.5 the velocity deficit over flat terrain, and D_{wake} over hill was about 0.27 the D_{wake} over flat terrain. At 6.09 D, the velocity deficit over hill was about 0.67 the velocity deficit over flat terrain, and D_{wake} over hill was almost the same as D_{wake} over flat terrain.

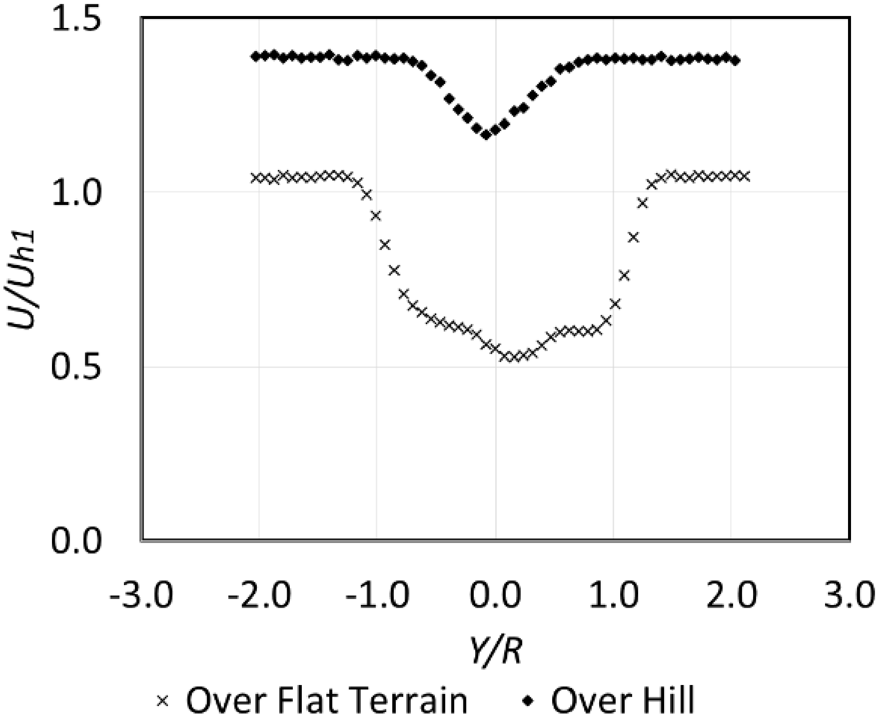

Figure 5.8 Comparison between configurations B and C at 3.05 D (Wind turbine at X=- L, measurement at X=0)

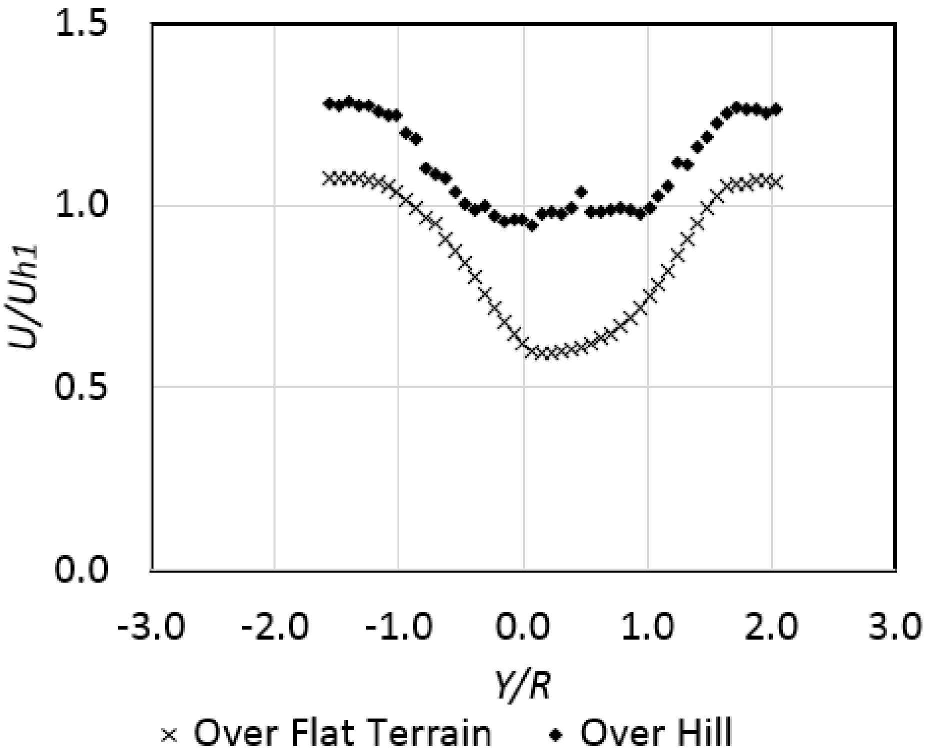

Figure 5.9 Comparison between configurations B and C at 6.09 D (Wind turbine at X=- L, measurement at X= L)

5.2 CFD Results

5.2.1 Wind Speed Profiles over the Two-Dimensional Hill

Figure 5.10 (a) to (f) compare wind tunnel test results with CFD simulation. Numerical results showed a good agreement with the experimental measurements.

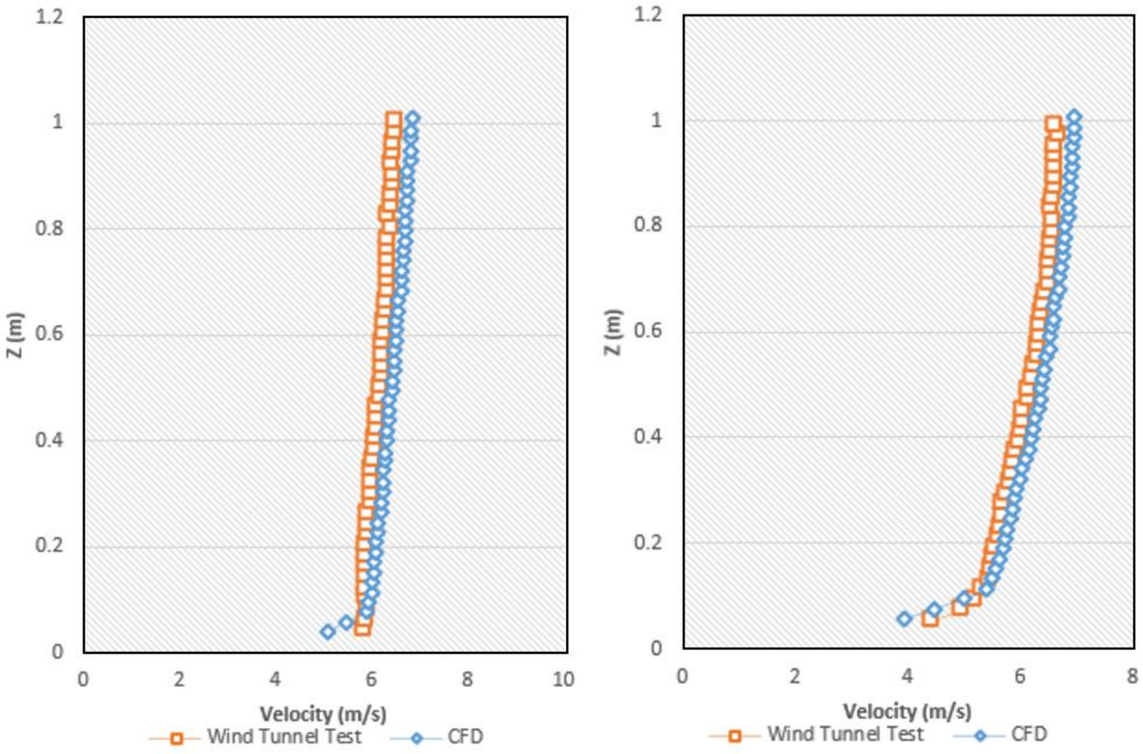

(a) (b)

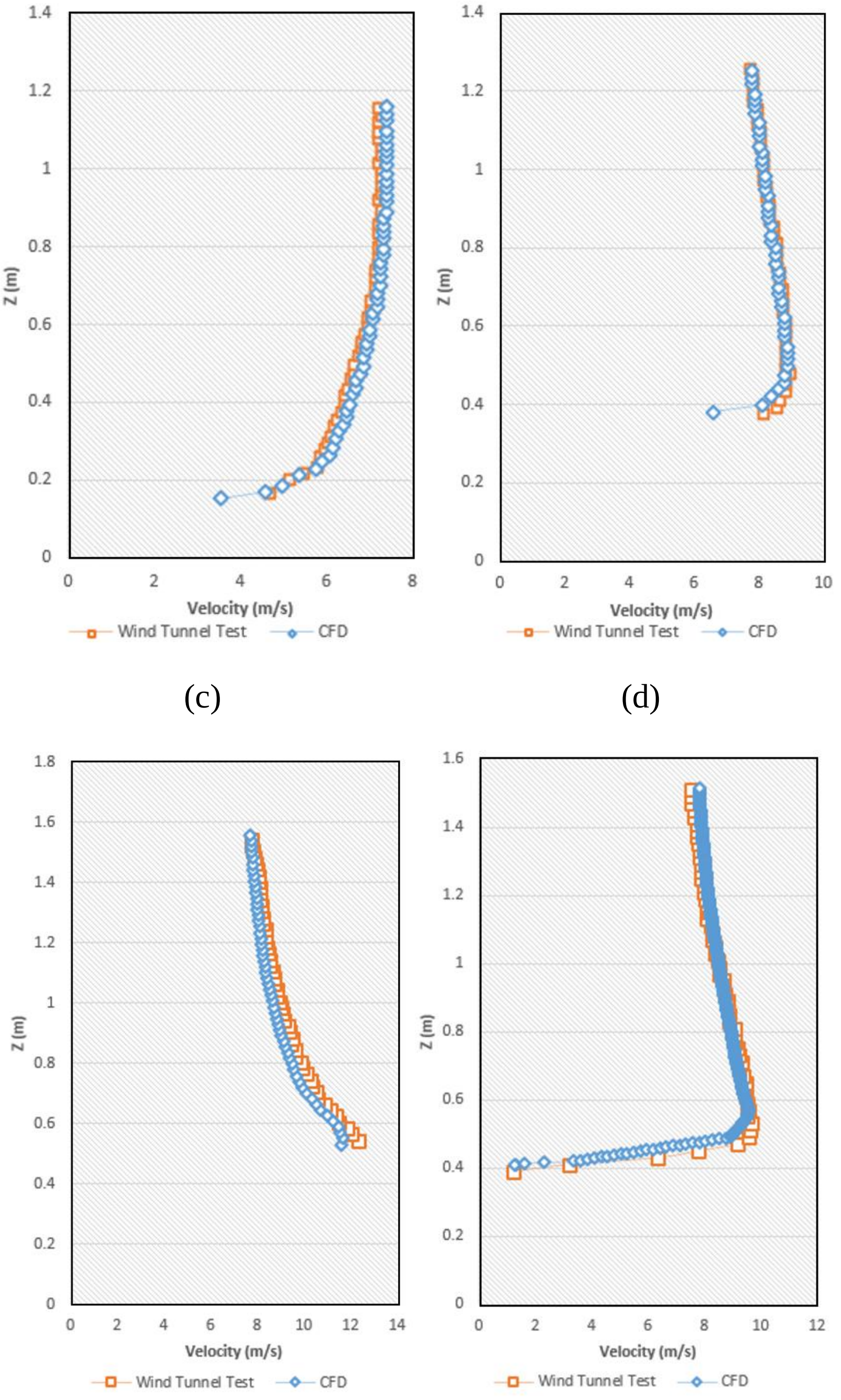

(c) (d)

(e) (f)

Figure 5.10 Wind speed profiles at: (a) –*L* (b) -3*L*/4 (c) –*L*/2 (d) –*L*/4 (e) 0 (f) *L*/4

5.2.2 Power and Thrust Coefficient

Figure 5.11 and Figure 5.12 show results of the second wind tunnel test configuration. Figure 5.11 shows the moment acting on turbine at six locations over 2D hill versus the tip speed ratio (TSR; λ). Moment acting on turbine is lowest at X = -1560 mm, and highest at X = 0 and X = 390 mm. This is due to the higher wind speed at the top of the hill compared with upstream wind speed. Power Coefficient (Cp) was calculated for the turbine at different tip speed ratios, as can be seen in Figure 5.12. Turbine performance at the top of the hill (X = 0) and X = 390 mm was better than that at X = -1560 mm (upstream of the hill), due to the higher hub wind speed.

Figure 5.13 and Figure 5.14 compare CFD simulations with wind tunnel test results upstream (over X = -1560 mm) and over X = 0. The Transition SST model had good agreement with experimental measurements. Predicting stall and flow separation at high tip speed ratios was possible using the Transition SST model, whereas the SST k-omega model failed to predict the stall as can be seen in Figure 5.13. This shows the usefulness of the Transition SST model as compared to a fully turbulent one. Therefore, the Transition SST model can be important for predicting wind turbine rotors performance.

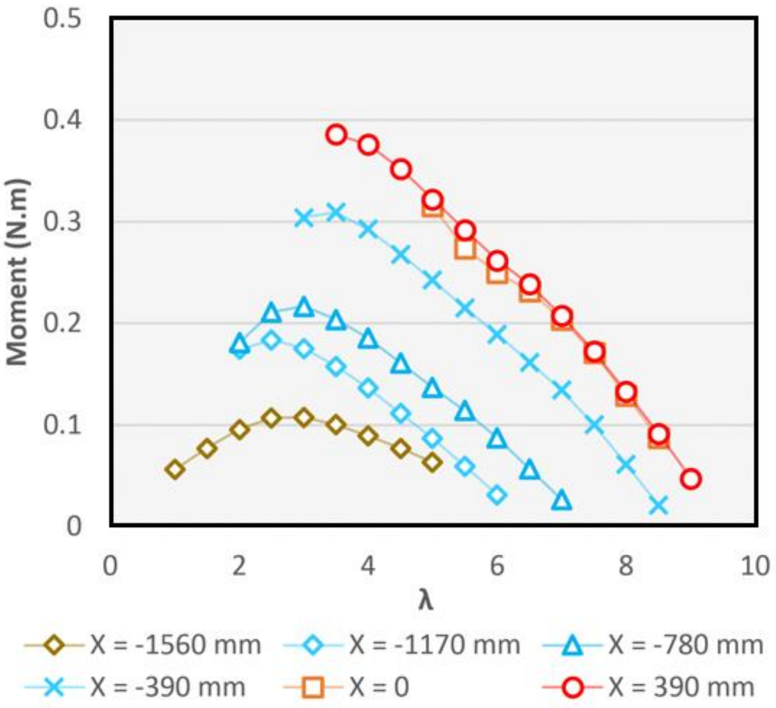

Figure 5.11 Moment acting on turbine over 2D hill at six locations.

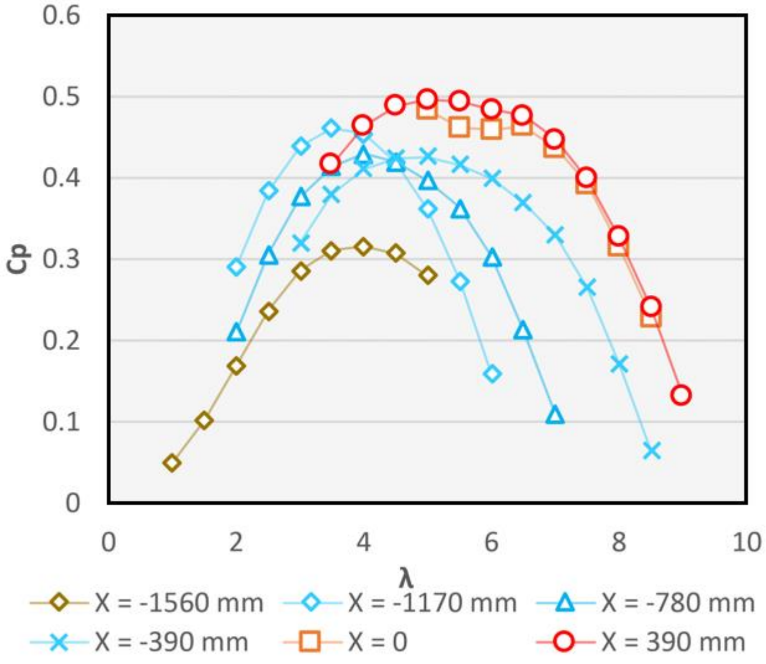

Figure 5.12 Wind turbine power coefficient over 2D hill at six locations.

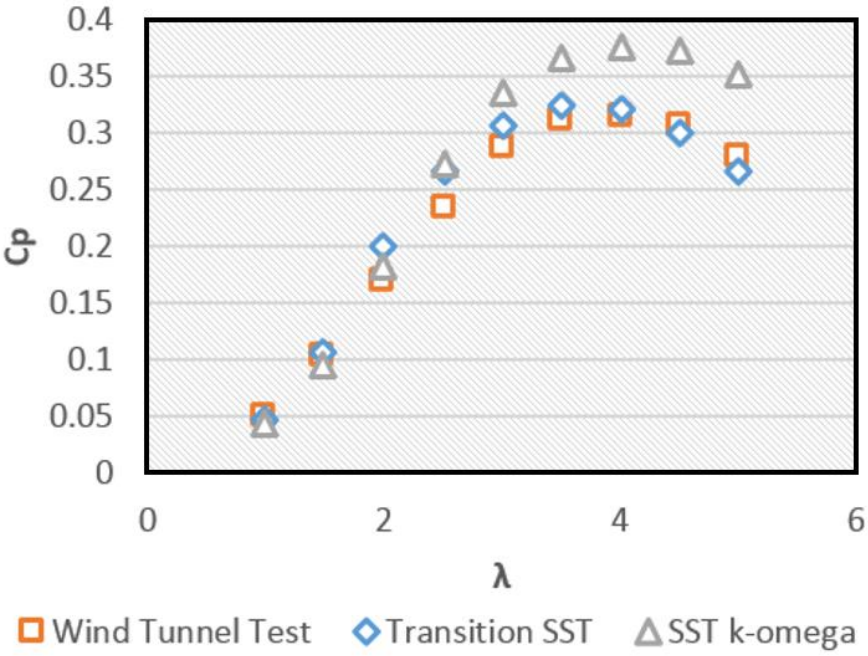

Figure 5.13 Wind turbine power coefficient at X = -1560 mm.

Figure 5.14 Wind turbine power coefficient at X = 0.

5.2.3 Wind Turbine Wake Development over Flat Terrain versus at the Top of the Hill

Figure 5.15 and Figure 5.16 show wake development over a flat terrain and that over a two-dimensional hill respectively. By comparing these two figures, the shape of the wake in Figure 5.16 is curved towards the ground compared to the wake shape over a flat terrain (Figure 5.15). This shows the great effect of the two-dimensional hill on the wind-turbine wake development.

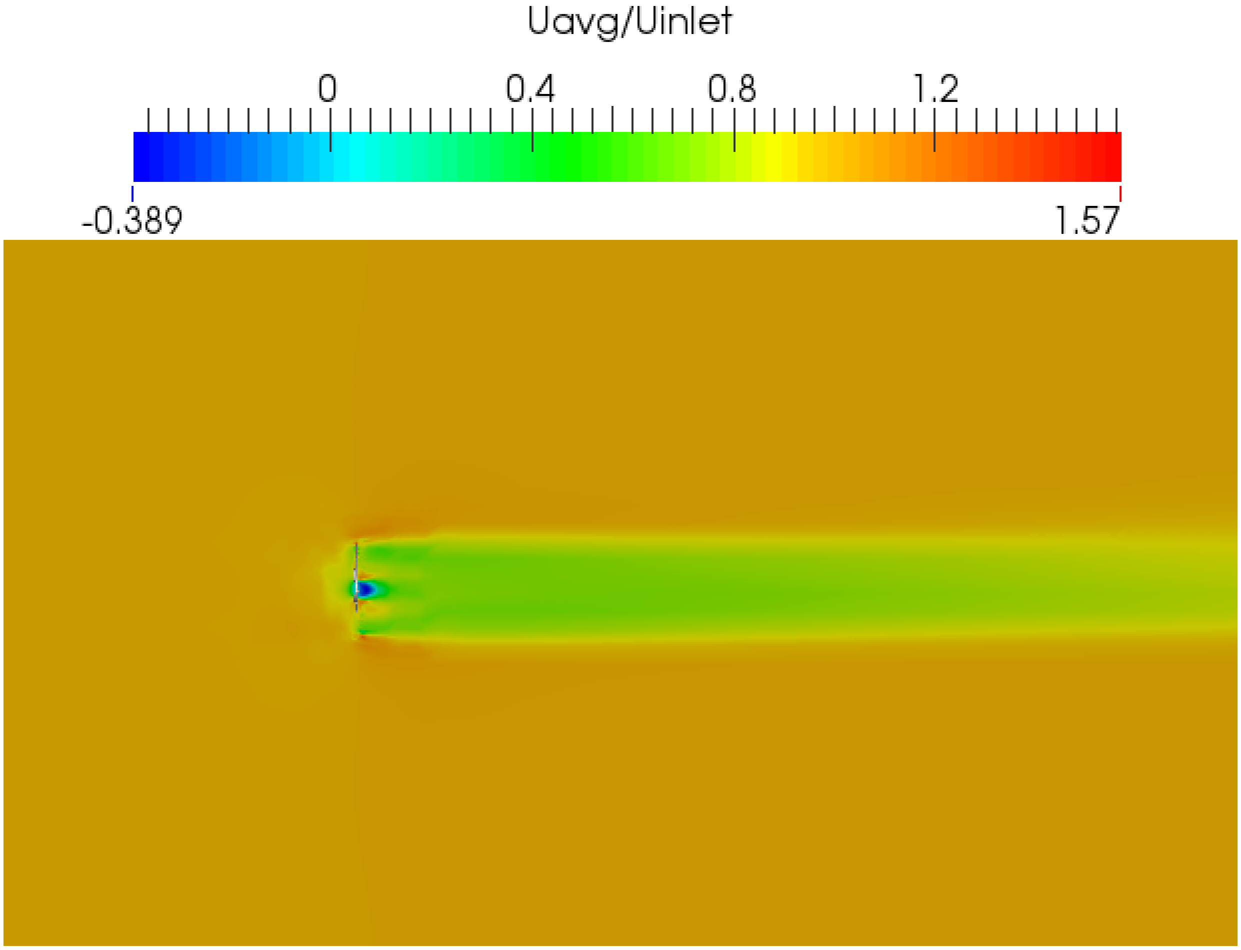

Figure 5.15 Wake development over a flat terrain.

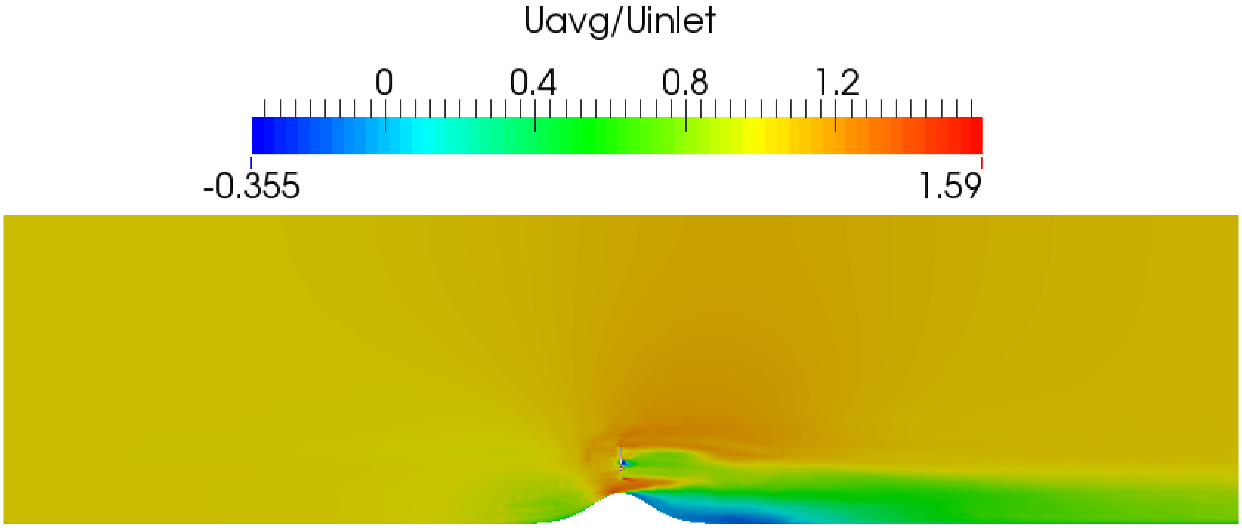

Figure 5.16 Wake development over a two-dimensional hill.

5.2.4 Wind Turbine Wake Development over the Two-Dimensional Hill

Figure 5.17 shows wind turbine wake development over the hill. The hill caused the wake to accelerate and shrink upstream of the hill. The wake center at the top of the hill was at the height of 0.8*h* from the hill surface, this means that the wake center at the top of the hill was shifted downwards due to the hill effect. Figure 5.18 show horizontal wake wind speed profiles at distances: 3*D*, 4*D*, 5*D*, and 6*D* away from the wind turbine rotor. At 3*D*, the wake width was about 1.26*D*, and by the time the wake reached 6*D* at the top of the hill, the wake width has decreased to about 0.39*D*. This means that the hill has caused the wake to accelerate and shrink upstream of the hill.

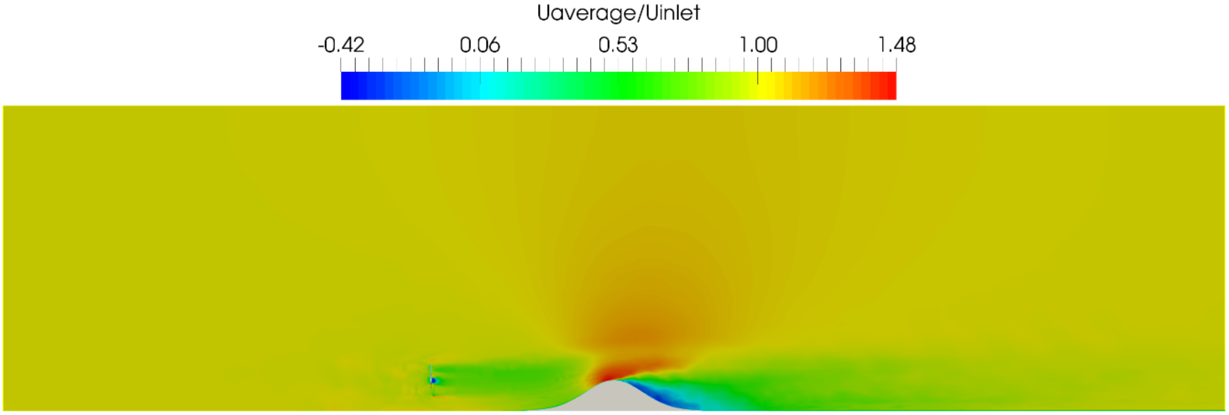

Figure 5.17 Wind turbine wake development over the hill.

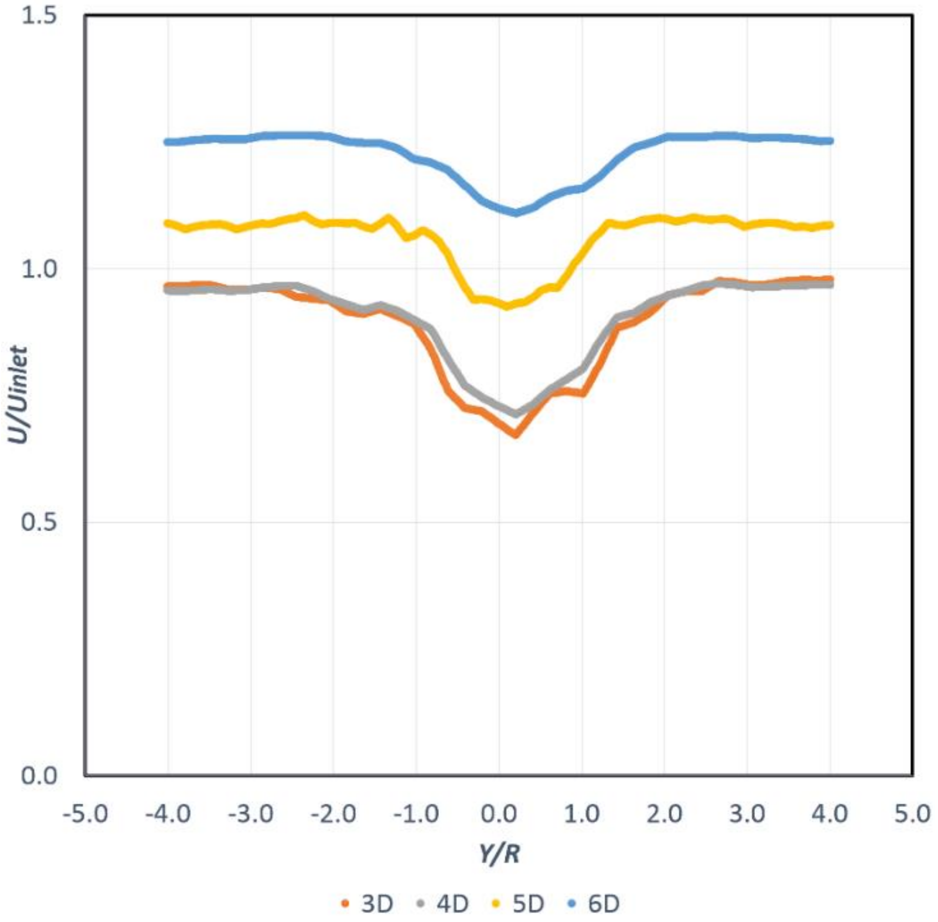

Figure 5.18 Horizontal wake wind speed profiles at distances: 3D, 4D, 5D, and 6D away from the wind turbine rotor.

6 Model Validation

6.1 Validation with Wind Tunnel Test

$C_{T\,Hill}$ was calculated at *X/L = -1/2*, *X/L = -1/4*, and *X/L = 0* using equation (2.5). All the parameters used for the calculations are shown in Table 6.1, where U_B is the value at 0.9 of the wake depth as shown in Figure 6.1. Figure 6.2 shows $C_{T\,Hill}/\,C_T$ over Flat terrain at locations 3 to 5. The Figure shows that $C_{T\,Hill}$ is very close to C_T over Flat terrain except at *X/L = 0*, this could be because the wake center at *X/L = 0* was moved downwards due to the hill effect.

Table 6.1 Parameters used for the calculations.

Parameters	Flat Terrain	*X/L* = -1/2	*X/L* = -1/4	*X/L* = 0
$\boldsymbol{D_{wake}/R}$	2.20	2.02	1.73	0.59
$\boldsymbol{U_{B0}/U_{h1}}$	1.07	1.15	1.30	1.39
$\boldsymbol{U_B/U_{h1}}$	0.64	0.85	0.99	1.19

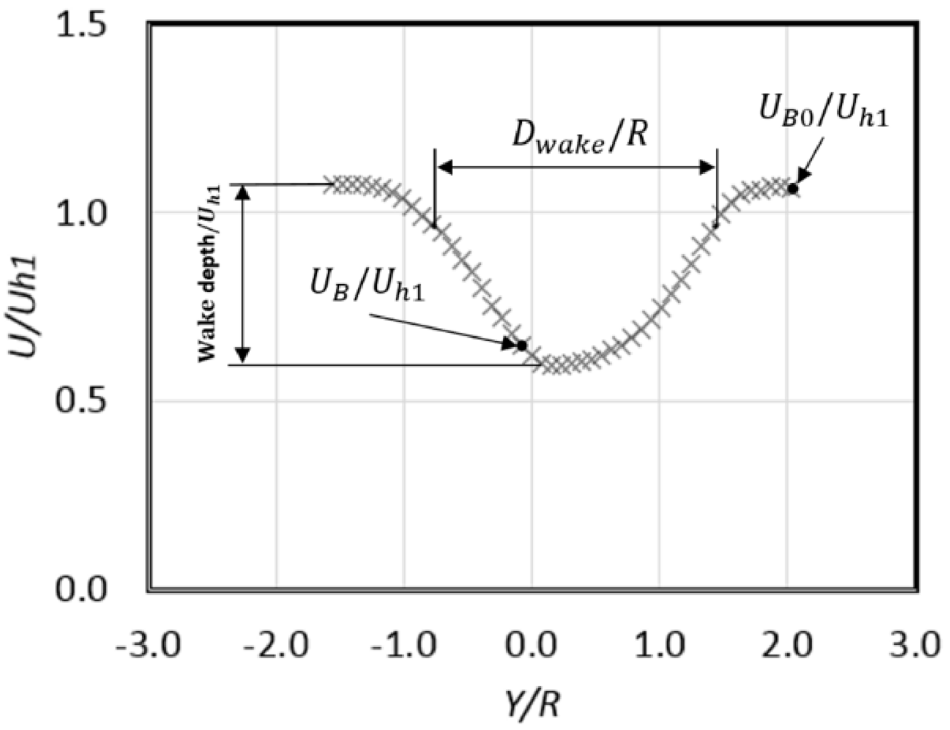

Figure 6.1 Wake over flat terrain at 6.09 *D* (Wind turbine at X=- *L*, measurement at X = *L*).

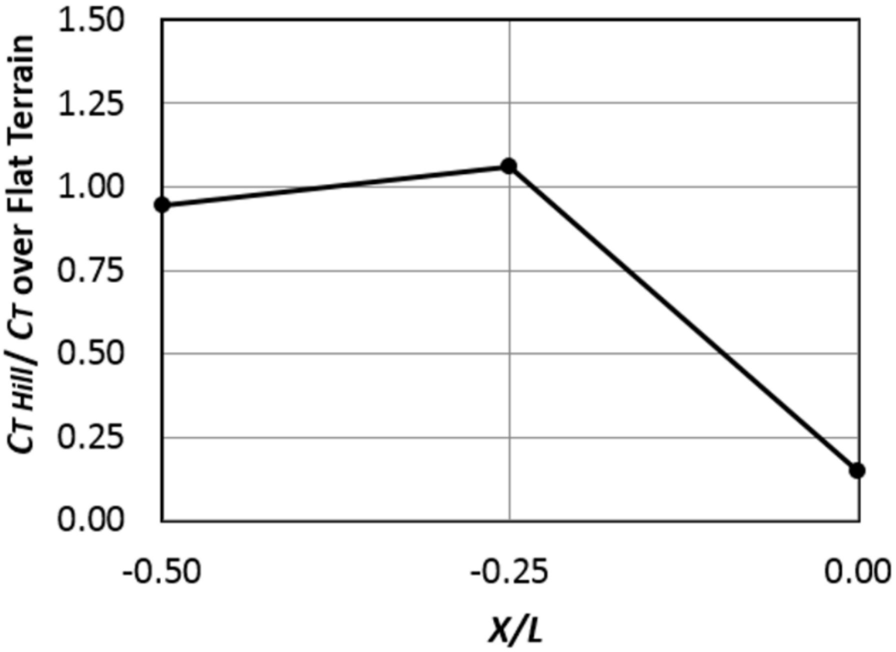

Figure 6.2 $C_{T\ Hill}/\ C_T$ over flat terrain at locations 3 to 5.

Equation (2.7) was used to calculate the estimated wake width. Figure 6.3 shows a comparison between the measured and estimated wake width/Rotor diameter for the configuration B at X/L=-1/2, X/L=-1/4, and X/L=0. The estimated wake width/Rotor diameter was close to that measured during the wind tunnel test. The percentage difference between the measured and estimated wake width/Rotor diameter at X/L=-1/2, X/L=-1/4, and X/L=0 is 13.3%, 23.6%, and 48.9% respectively. The measured wake width at the top of the hill (X/L=0) drops more quickly than the estimated value, this could be because, the wake shifts downward slightly due to the effect of the terrain.

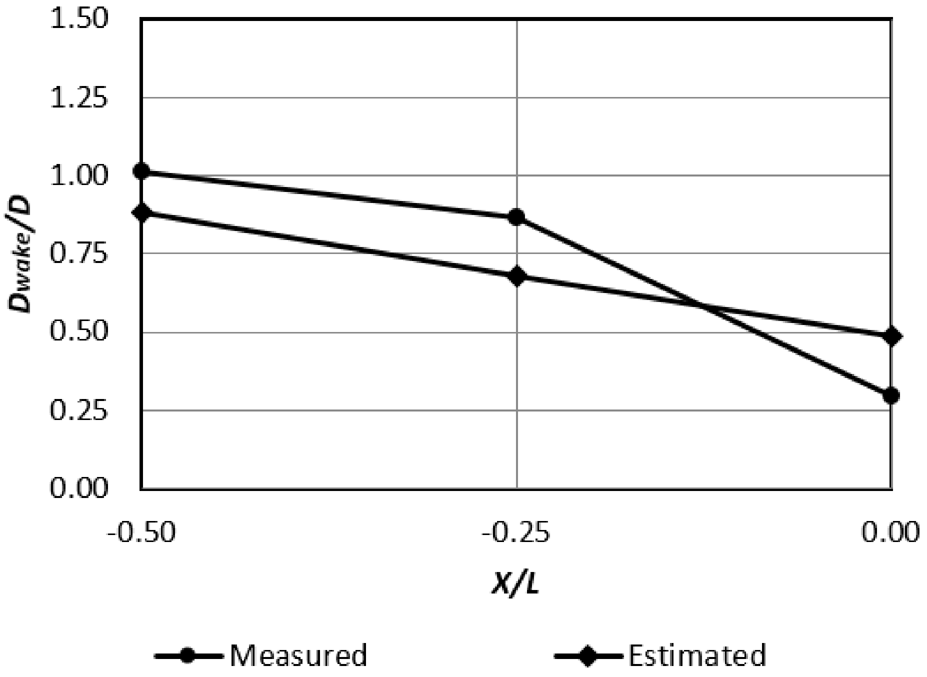

Figure 6.3 Comparison between the measured and estimated wake width/Rotor diameter.

6.2 Validation with CFD

Equation (2.7) was used to calculate the estimated wake width. All the parameters used for the calculations are shown in Table 6.2. Figure 6.4 shows a comparison between CFD and estimated wake width/Rotor diameter at distances: 4*D*, 5*D*, and 6*D* away from the wind turbine rotor. The estimated wake width/Rotor diameter was close to that obtained using CFD. The percentage difference between CFD and estimated wake width/Rotor diameter at 4*D*, 5*D*, and 6*D* is 9.41%, 13.95%, and 15.56% respectively.

Table 6.2 Parameters used for the calculations.

Parameters	3D	*4D*	*5D*	*6D*
$\boldsymbol{D_{wake}/R}$	2.52	2.04	1.24	0.78
$\boldsymbol{U_{B0}/U_{inlet}}$	0.99	0.96	1.09	1.26
$\boldsymbol{U_B/U_{inlet}}$	0.70	0.74	0.94	1.12

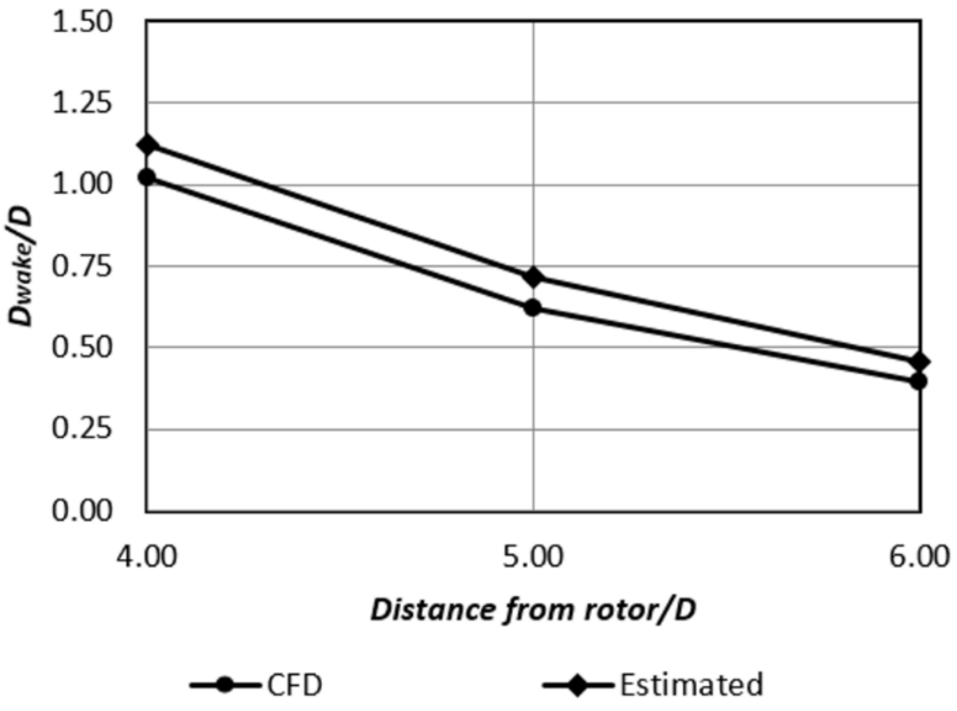

Figure 6.4 Comparison between CFD and estimated wake width/Rotor diameter.

7 Wind Farm Layout Optimization over Complex Terrain

7.1 Genetic Algorithm

A Genetic Algorithm (GA) was developed as an initial step for the wind farm layout optimization over complex terrain process. The GA consists of the following steps:

1. Create Parent, Offspring, and Elite sets.
2. Create the initial grid of wind turbines (Figure 7.2).
3. Randomly generate new populations.
4. Evaluate the fitness of each population with respect to the fitness function (Equation 7.1).
5. Select parents and choose Elite.
6. Produce children from parents either by mutation or crossover.
7. Replace current population with children to form the next generation.
8. Start again from step 4, and stop when a predetermined condition is met.

The algorithm can deal with any irregular wind farm borders as shown in Figure 7.1 to Figure 7.3. Also, the algorithm can avoid placing turbines inside irregular barriers such as roads, and areas with high Turbulence Intensity.

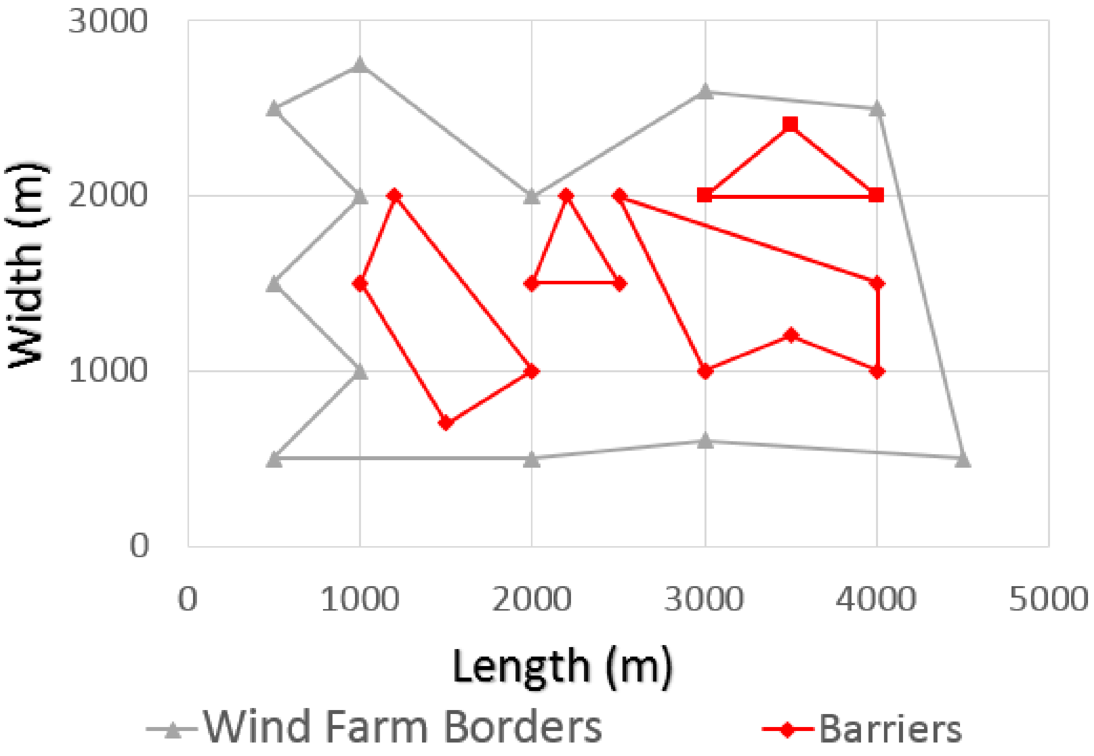

Figure 7.1 Wind farm borders and barriers.

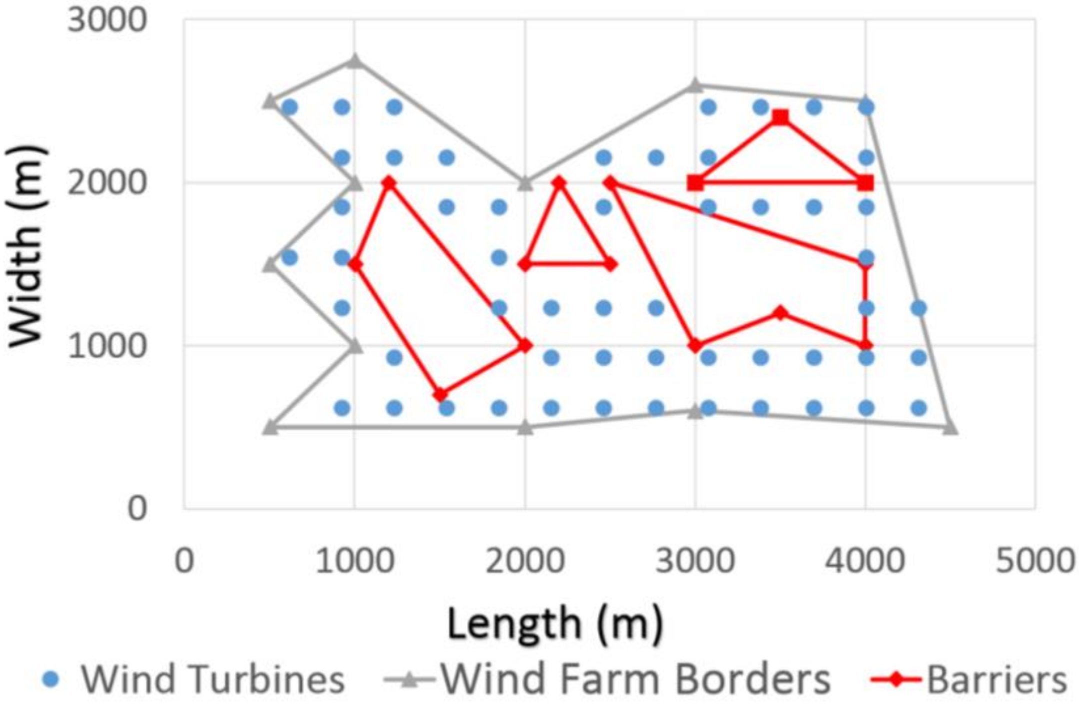

Figure 7.2 Initial Grid.

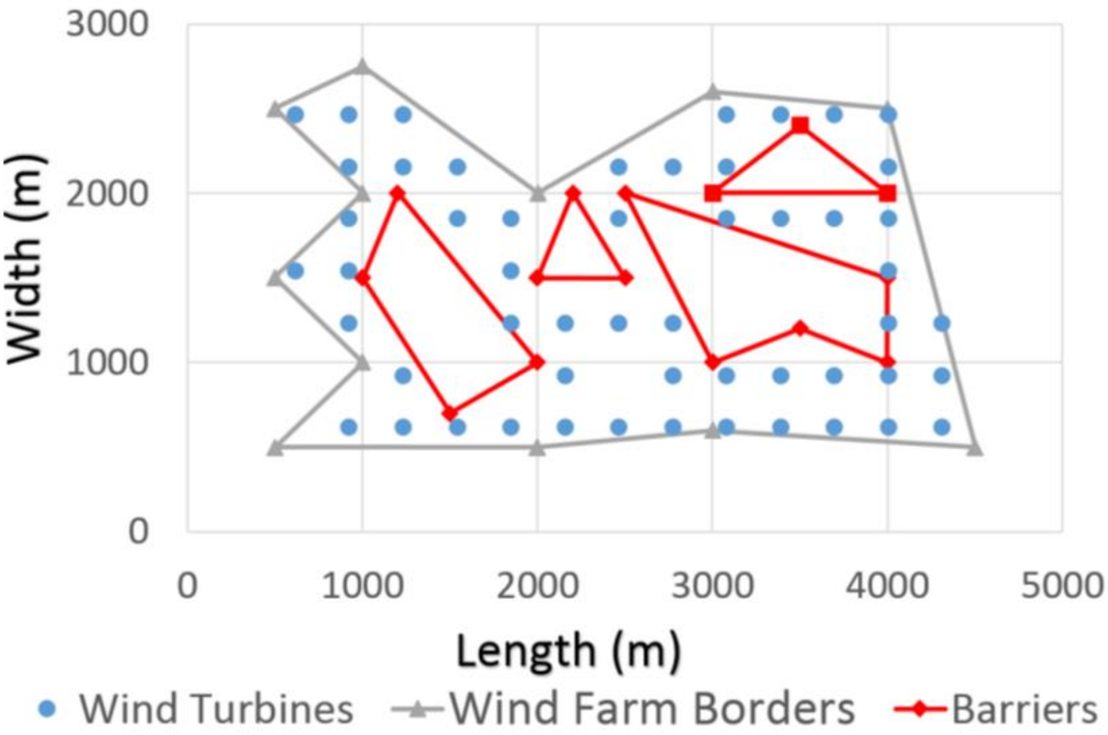

Figure 7.3 GA output.

The Cost of Energy (COE) for a wind farm can be represented by the following equation:

$$COE = \frac{N * C_{O\&M} + \left(N * C_{WT} + C_s * floor\left(\frac{N}{M}\right)\right)\left(\frac{1}{3} * e^{-0.00174N^2} + \frac{2}{3}\right)}{8760P_{WF} * (Annual\ Interests)} \tag{7.1}$$

Where, N is the number of wind turbines, $C_{O\&M}$ is the annual operation and maintenance cost per wind turbine, C_{WT} is the cost per wind turbine, C_s is the cost per substation, M is the number of wind turbines for each substation, P_{WF} is the wind farm power output.

7.2 A modified Random Algorithm

A modified Random Algorithm (RA) was developed in this thesis based on the work done by Feng and Shen [26]. The modified RA was developed to overcome the limitations of the Genetic Algorithm and improve the output of the optimization process. The modified RA consists of the following steps:

1. Use the output of the GA as an initial solution to the Random Algorithm.
2. Generate new random locations which satisfy the following conditions:
    i. Favors high elevations and high wind speeds, as shown in Figure 7.4.
    ii. Doesn’t favor lower elevations, low wind speeds, or high turbulence intensity areas.
    iii. Inside wind farm borders.
    iv. Outside of barriers
3. Select a random turbine from the initial solution.
4. Move the selected turbine to one of the new random locations generated in step 2.
5. Check if the distance between any two turbines less than 4D.
    i. If True: ignore step 4 and start again from step 3.
    ii. If False: continue to step 6.
6. Evaluate the Cost of Energy (COE) of the new wind farm layout.
    i. If COE increase: ignore step 4 and start again from step 3.
    ii. If COE decrease: keep the selected turbine at the new location.
7. Start again from step 3, and stop when a predetermined condition is met.

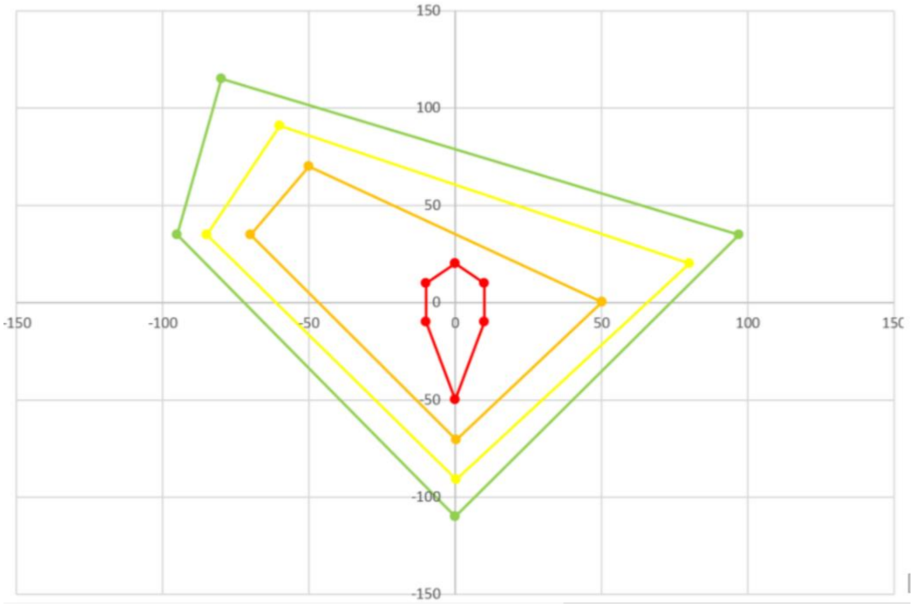

(a)

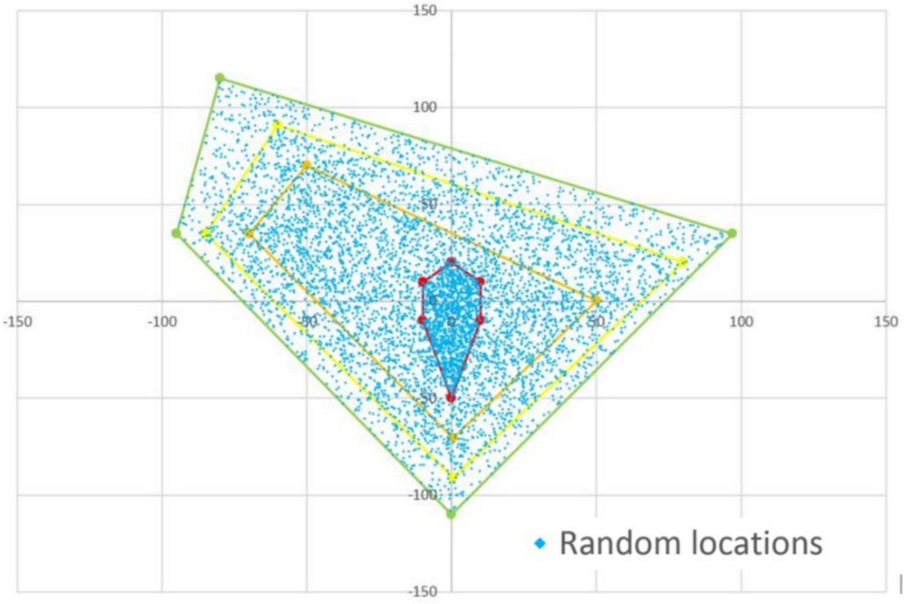

(b)

Figure 7.4 (a) Shows the contour lines of a terrain, where red represents the highest area, and blue represents the lowest areas; (b) New random locations were generated using the modified RA.

Figure 7.5 shows a comparison between the output of GA and the output of the modified RA. As can be seen in the figure, the modified RA was able to make use of all the wind farm borders, overcome the limitations of the Genetic Algorithm, and improve the output of the optimization algorithm to generate more energy and reduce the COE.

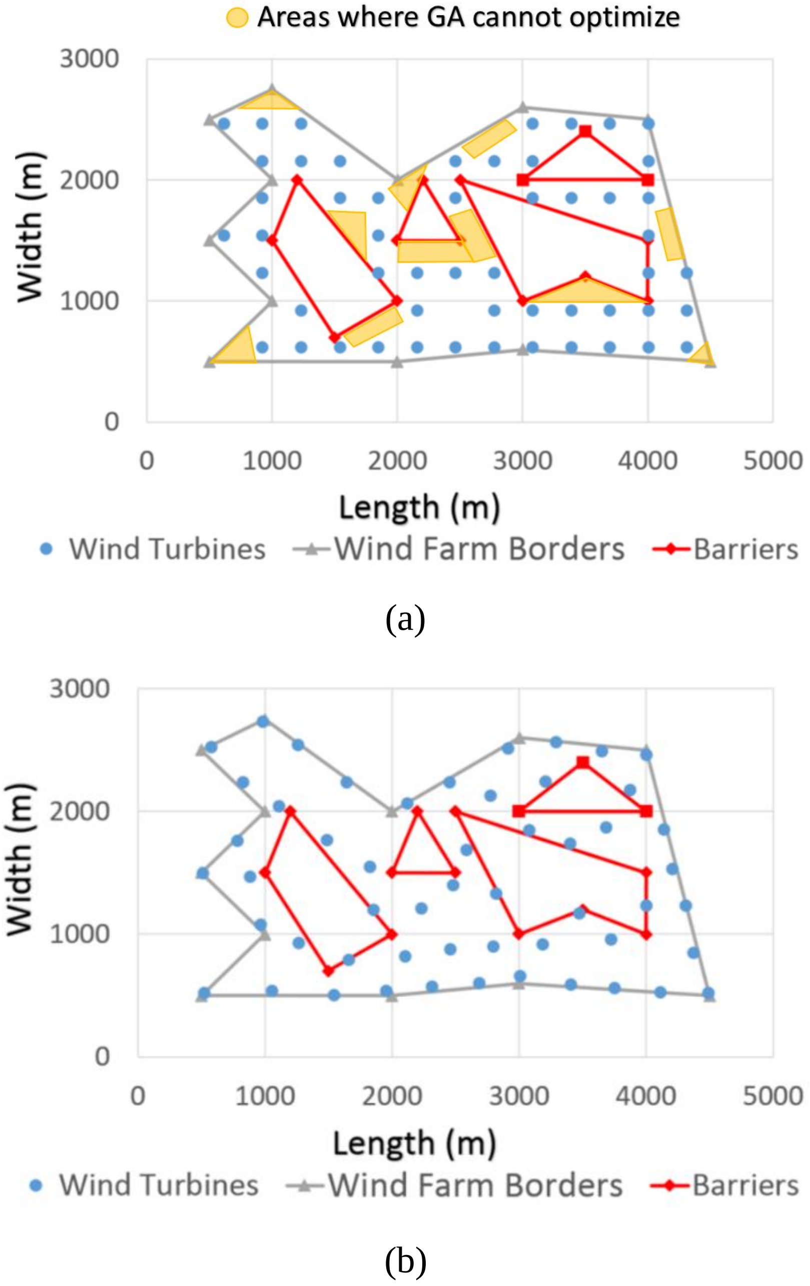

Figure 7.5 (a) GA output, where areas the GA cannot optimize are highlighted; (b) Modified RA output.

8 CTFLOW

CTFLOW (Complex Terrain Farm Layout Optimization Workbench) was developed by the author for layout optimization over complex terrain. The Graphical User Interface (GUI) is shown in Figure 8.1.

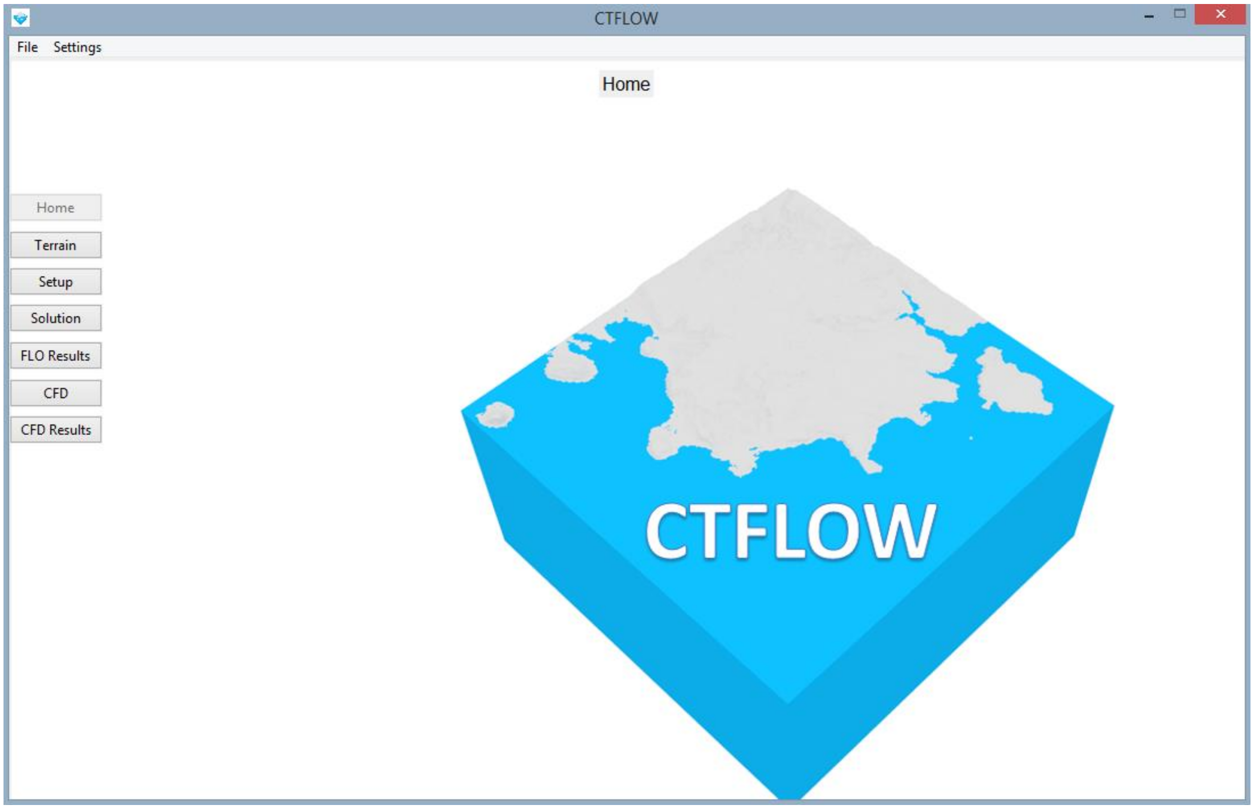

Figure 8.1 Complex Terrain Farm Layout Optimization Workbench.

The following are the steps for using the software:

Step 1: Generating terrain STL file

CTFLOW can import satellite terrain images then convert them directly to an STL file (as shown in Figure 8.2 to Figure 8.4), rather than creating the STL file manually (which can be a tedious and time consuming task).

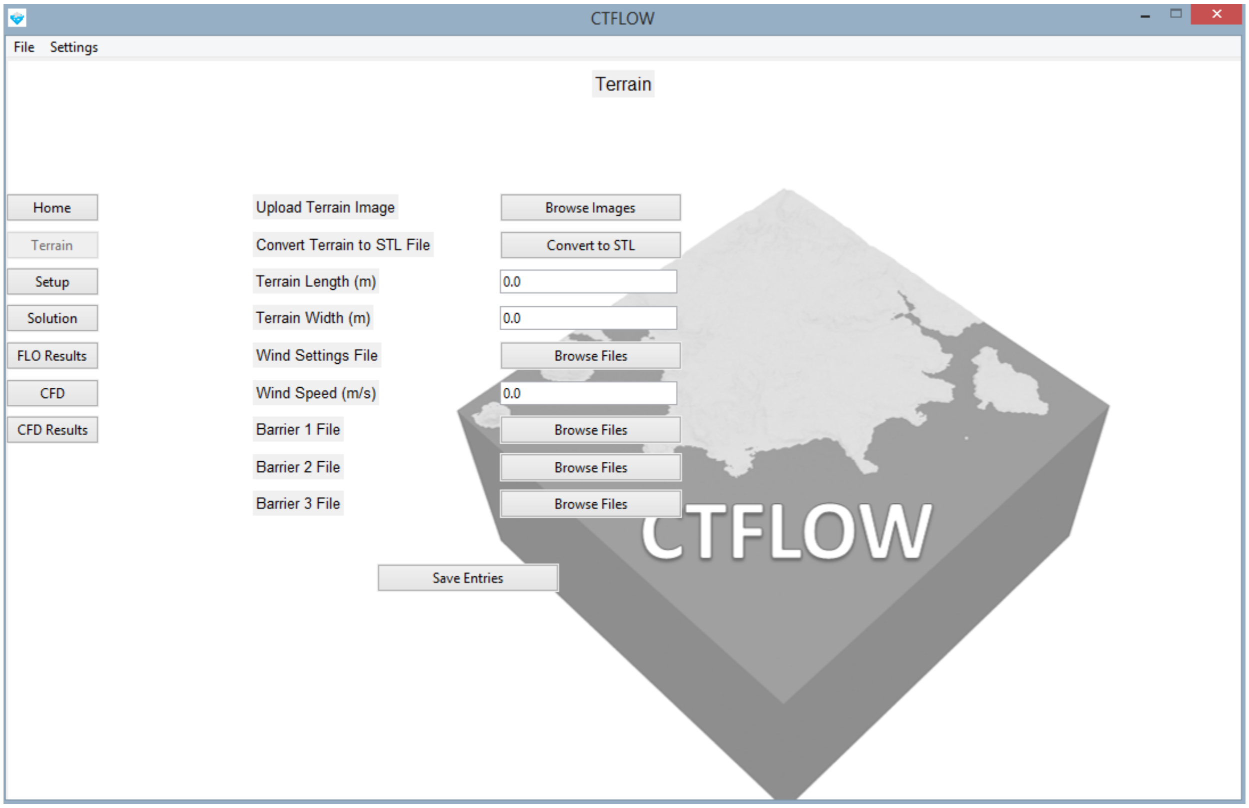

Terrain Length (m) 0.0

Terrain Width (m) 0.0

Wind Speed (m/s) 0.0

Figure 8.2 CTFLOW is used for wind farm layout optimization over complex terrain.

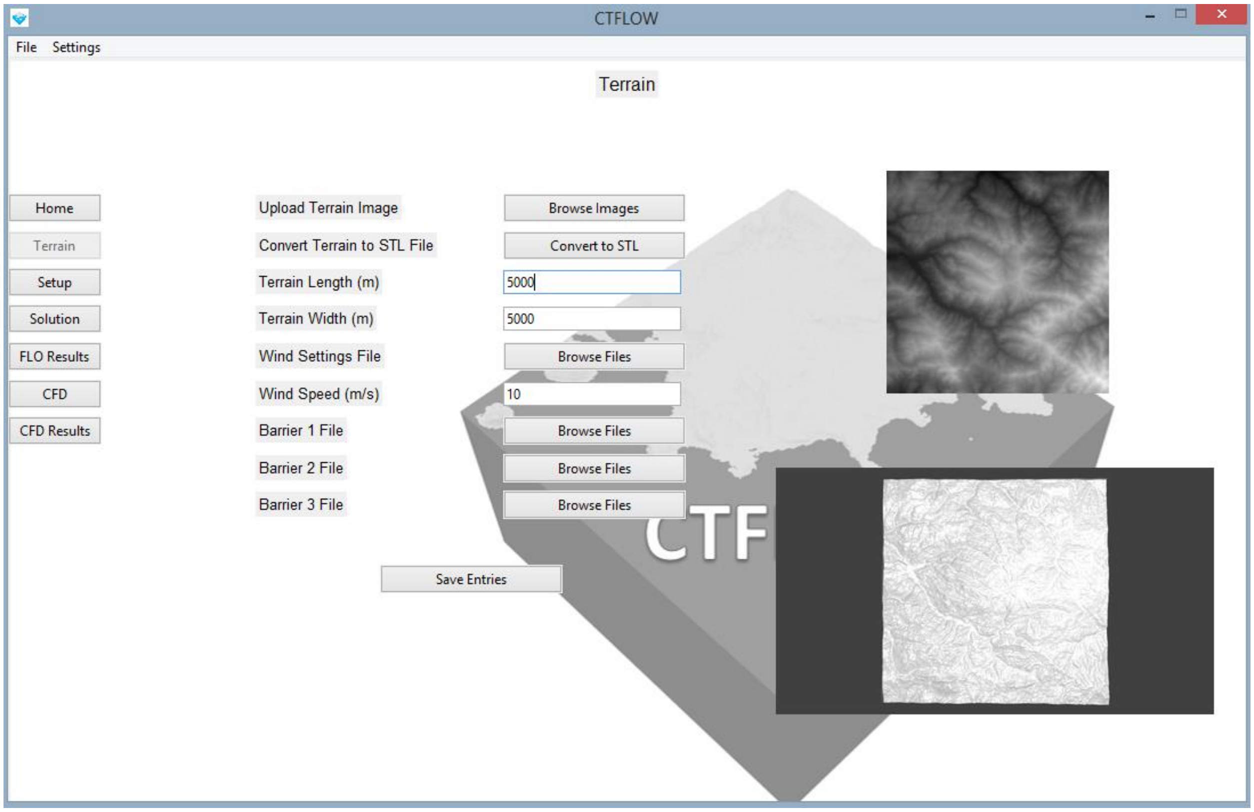

Terrain Length (m) 5000

Terrain Width (m) 5000

Wind Speed (m/s) 10

Figure 8.3 Importing satellite terrain images then converting them directly to an STL file

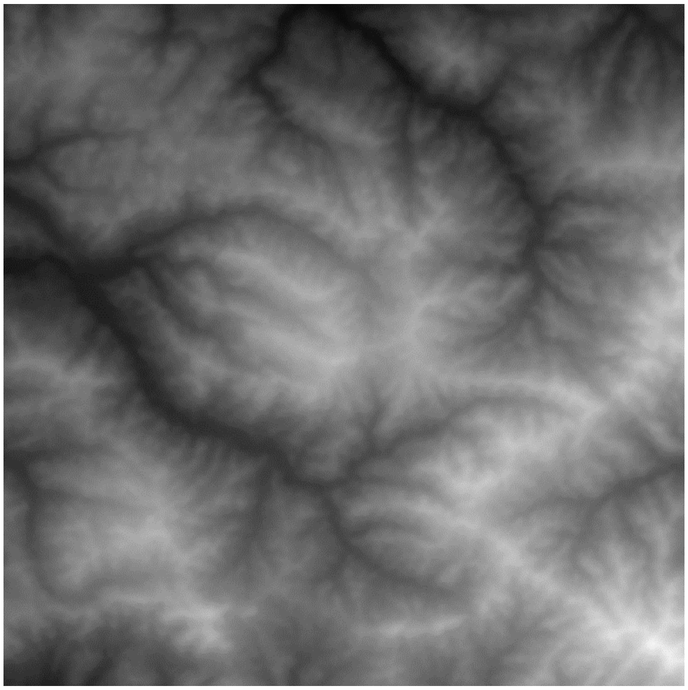

(a)

(b)

Figure 8.4 Converting satellite terrain image directly to an STL file. (a) Satellite terrain image; (b) STL file of the terrain.

Step 2: Uploading settings file

Uploading a settings file by the user that contains information such as: terrain length and width, wind setting file, wind farm borders, wind farm barriers, wind turbine specifications as shown in Table 8.1 to Table 8.5, and Figure 8.5 to Figure 8.7.

Table 8.1 An example of a wind setting file (From theta="0" to theta="45").

theta="0"	c="5.647690"	k="2.985195"	omega="0.048955"
theta="15"	c="7.349626"	k="3.523647"	omega="0.032574"
theta="30"	c="8.222031"	k="1.729255"	omega="0.017582"
theta="45"	c="8.071149"	k="2.568082"	omega="0.006319"

Table 8.2 An example of a wind setting file (From theta="60" to theta="345").

theta="60"	c="9.541978"	k="1.993438"	omega="0.000541"
theta="75"	c="8.652621"	k="2.490072"	omega="0.082663"
theta="90"	c="6.507816"	k="2.465158"	omega="0.077562"
theta="105"	c="8.949849"	k="3.062744"	omega="0.066829"
theta="120"	c="6.643308"	k="3.294917"	omega="0.052141"
theta="135"	c="5.697838"	k="3.044321"	omega="0.035789"
theta="150"	c="5.719562"	k="2.961634"	omega="0.020324"
theta="165"	c="8.743764"	k="2.166234"	omega="0.008159"
theta="180"	c="9.110421"	k="2.031583"	omega="0.001193"
theta="195"	c="6.725090"	k="1.815424"	omega="0.000512"
theta="210"	c="10.419769"	k="2.342080"	omega="0.006222"
theta="225"	c="7.617459"	k="2.990985"	omega="0.017433"
theta="240"	c="8.614856"	k="1.592461"	omega="0.032396"
theta="255"	c="7.876530"	k="4.841224"	omega="0.048775"
theta="270"	c="11.993449"	k="2.146332"	omega="0.064015"
theta="285"	c="9.379689"	k="3.739560"	omega="0.075739"
theta="300"	c="12.192645"	k="2.469500"	omega="0.082116"
theta="315"	c="9.169049"	k="1.327429"	omega="0.082152"
theta="330"	c="10.246860"	k="1.732229"	omega="0.075841"
theta="345"	c="8.355799"	k="2.204085"	omega="0.064168"

Table 8.3 An example of a wind farm borders file.

x="2000.1"	y="500.12"
x="500.2"	y="500.11"
x="1000.3"	y="1000.1"
x="500.4"	y="1500.9"
x="1000.5"	y="2000.8"
x="500.6"	y="2500.7"
x="1000.7"	y="2750.6"
x="2000.8"	y="2000.5"
x="3000.9"	y="2600.4"
x="4000.1"	y="2500.3"
x="4500.11"	y="500.2"
x="3000.12"	y="600.1"

Table 8.4 An example of a wind farm barriers file.

Barrier Number="0"	
x="3000.1"	y="1000.4"
x="2500.2"	y="2000.3"
x="4000.3"	y="1500.2"
x="4000.4"	y="1000.1"
x="3500.5"	y="1200.5"
Barrier Number="1"	
x="1000.1"	y="1500.4"
x="1200.2"	y="2000.3"
x="2000.3"	y="1000.2"
x="1500.4"	y="700.1"
Barrier Number="2"	
x="3000.1"	y="2000.7"
x="3500.64"	y="2400.48"
x="4000.23"	y="2000.45"
Barrier Number="3"	
x="2000.6"	y="1500.4"
x="2200.5"	y="2000.3"
x="2500.1"	y="1500.7"

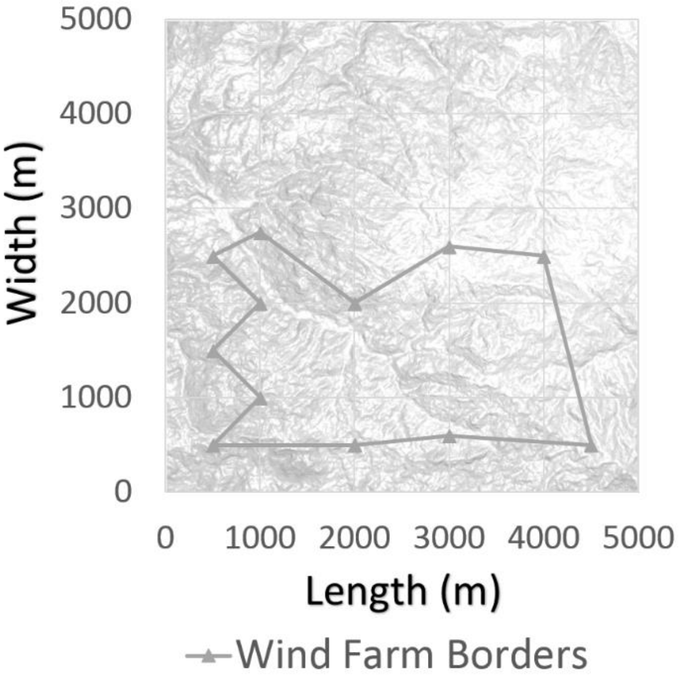

Figure 8.5 An example of wind farm borders.

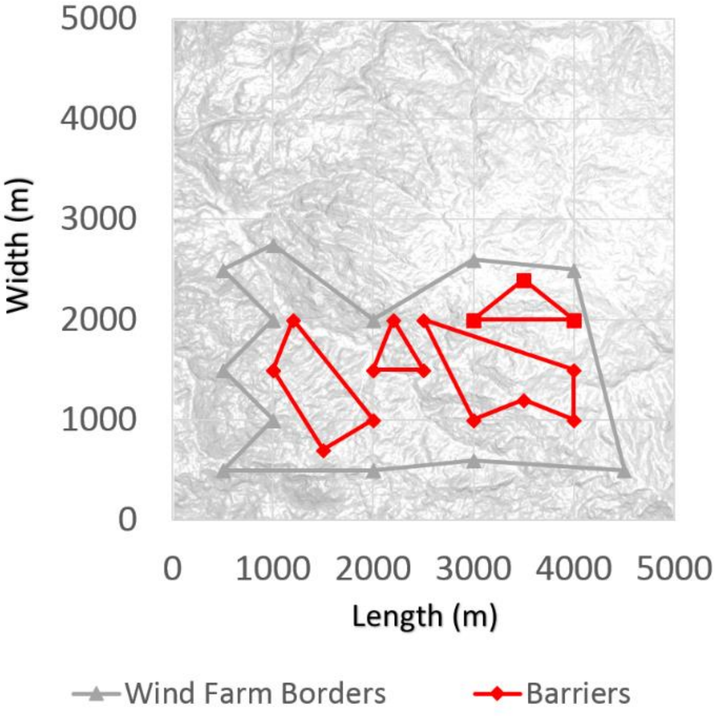

Figure 8.6 An example of barriers in a wind farm.

Table 8.5 An example of wind turbine specifications file.

Thrust Coefficient	0.8
Rated Power	2000
Wind Turbine Radius	40
eta	-550
k	0.075
lambda	150
Cut-in wind speed	4
Cut-out wind speed	25
Rated wind speed	13

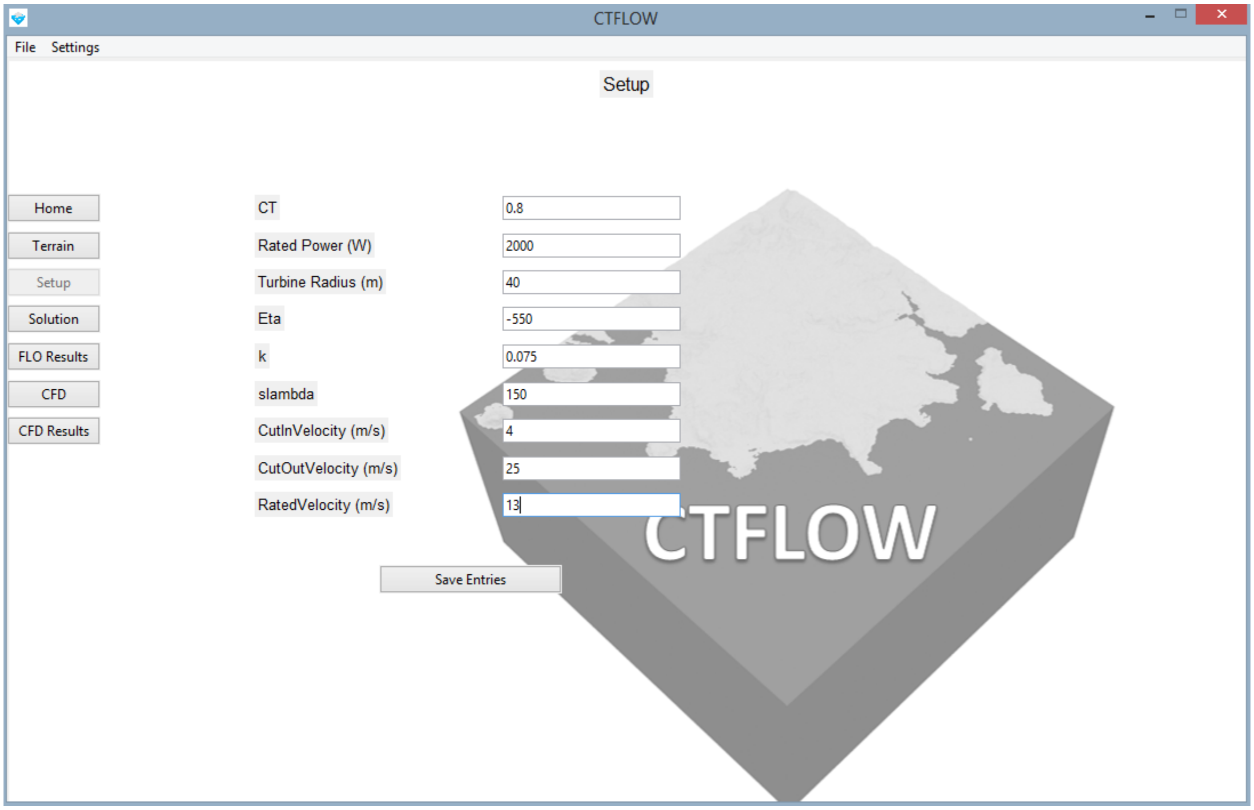

CT	0.8
Rated Power (W)	2000
Turbine Radius (m)	40
Eta	-550
k	0.075
slambda	150
CutInVelocity (m/s)	4
CutOutVelocity (m/s)	25
RatedVelocity (m/s)	13

Figure 8.7 Wind turbine specifications.

Step 3: CFD

CTFLOW will run CFD simulations of wind flow over the terrain using the STL file generated in step 1. The CFD simulations will be performed in at least 16 direction as shown in Figure 8.8 to obtain wind speed and turbulence intensity profiles over the terrain as shown in Figure 8.9, this is an important step for layout optimization over complex terrain, as the algorithm will avoid placing wind turbines in areas with high turbulence intensities.

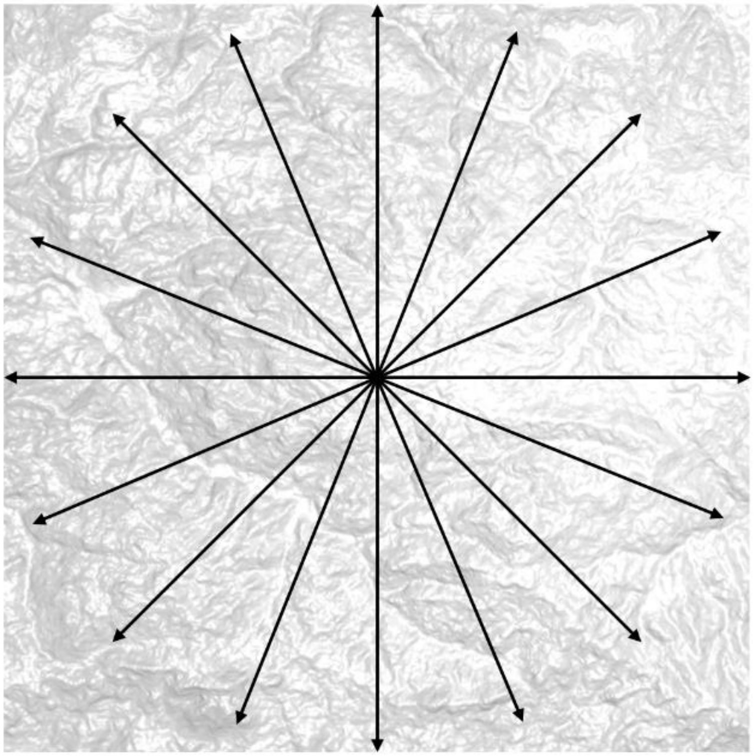

Figure 8.8 CFD will be performed in at least 16 direction over the terrain.

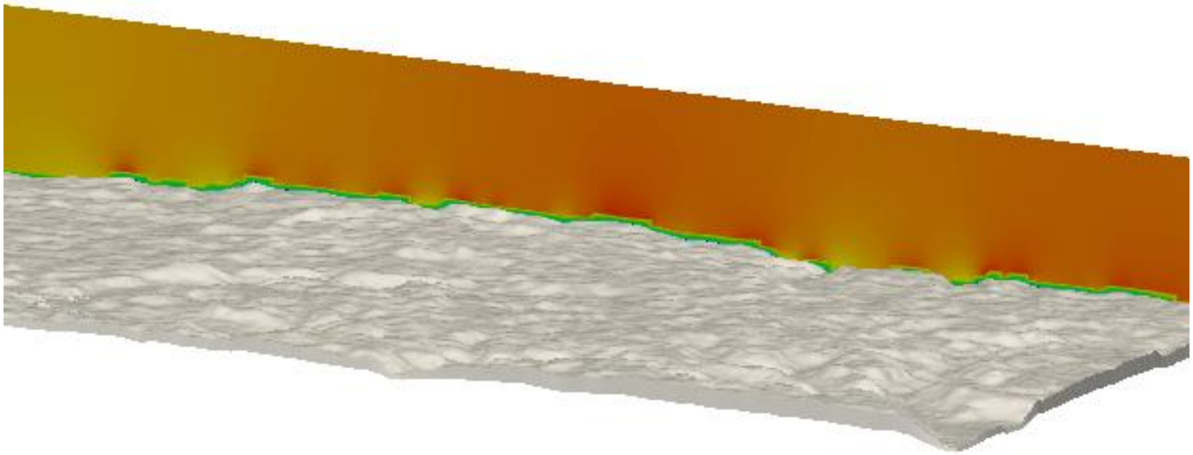

Figure 8.9 Wind speed profiles over the terrain.

Step 4: Post processing

Wind speed and turbulence intensity profiles will be imported, as these are important for the next optimization step.

Step 5: Layout optimization using GA

1. Create Parent, Offspring, and Elite sets.
2. Create the initial grid of wind turbines (Figure 8.10).
3. Randomly generate new populations.
4. Evaluate the fitness of each population with respect to the fitness function.
5. Select parents and choose Elite.
6. Produce children from parents either by mutation or crossover.
7. Replace current population with children to form the next generation.
8. Start again from step 4, and stop when a predetermined condition is met.

The final GA output is shown in Figure 8.11.

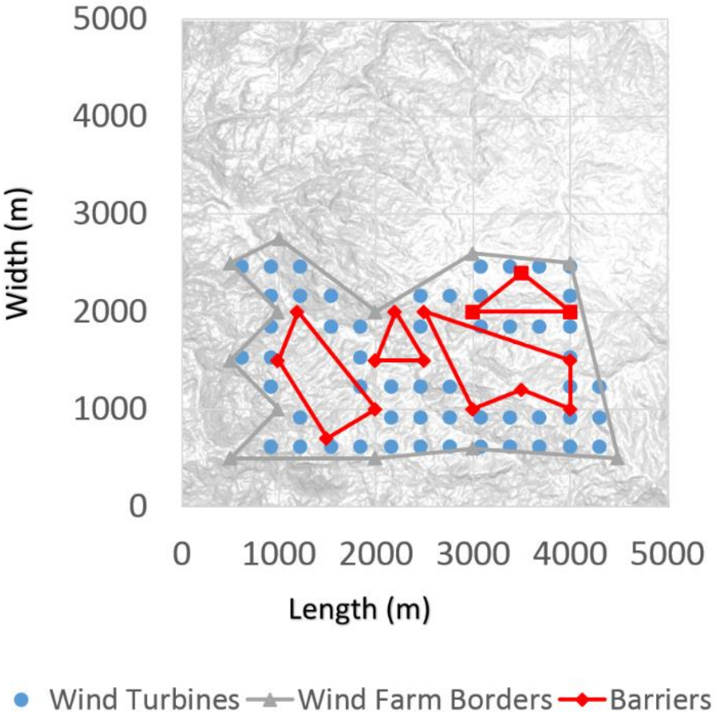

Figure 8.10 the initial grid of wind turbines.

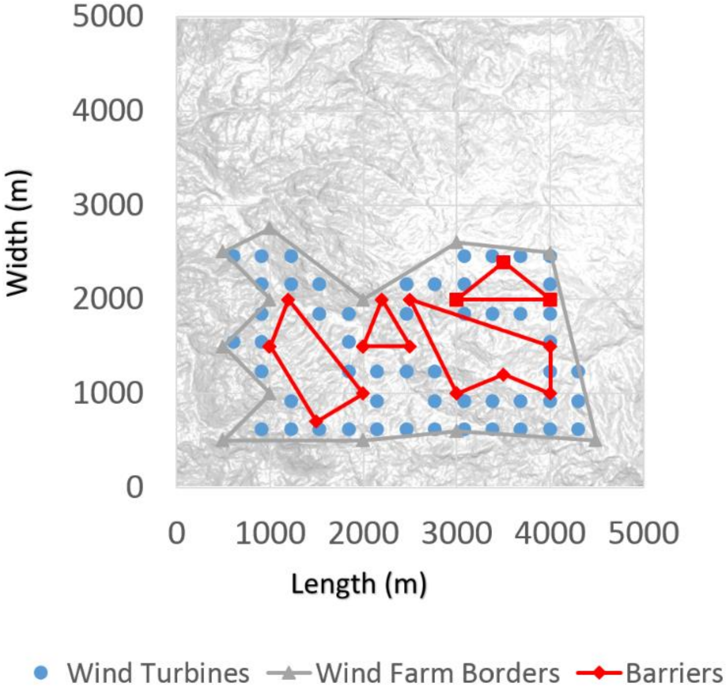

Figure 8.11 Final GA output.

Step 6: Improving GA output using Modified RA

1. Use the output of the GA as an initial solution to the Random Algorithm.
2. Generate new random locations which satisfy the following conditions:
    i. Favors high elevations and high wind speeds.
    ii. Doesn’t favor lower elevations, low wind speeds, or high turbulence intensity areas.
    iii. Inside wind farm borders.
    iv. Outside of barriers
3. Select a random turbine from the initial solution.
4. Move the selected turbine to one of the new random locations generated in step 2.
5. Check if the distance between any two turbines less than 4D.
    i. If True: ignore step 4 and start again from step 3.
    ii. If False: continue to step 6.
6. Evaluate the Cost of Energy (COE) of the new wind farm layout.
    i. If COE increase: ignore step 4 and start again from step 3.
    ii. If COE decrease: keep the selected turbine at the new location.
7. Start again from step 3, and stop when a predetermined condition is met

The final output of the Modified RA is as shown in Figure 8.12.

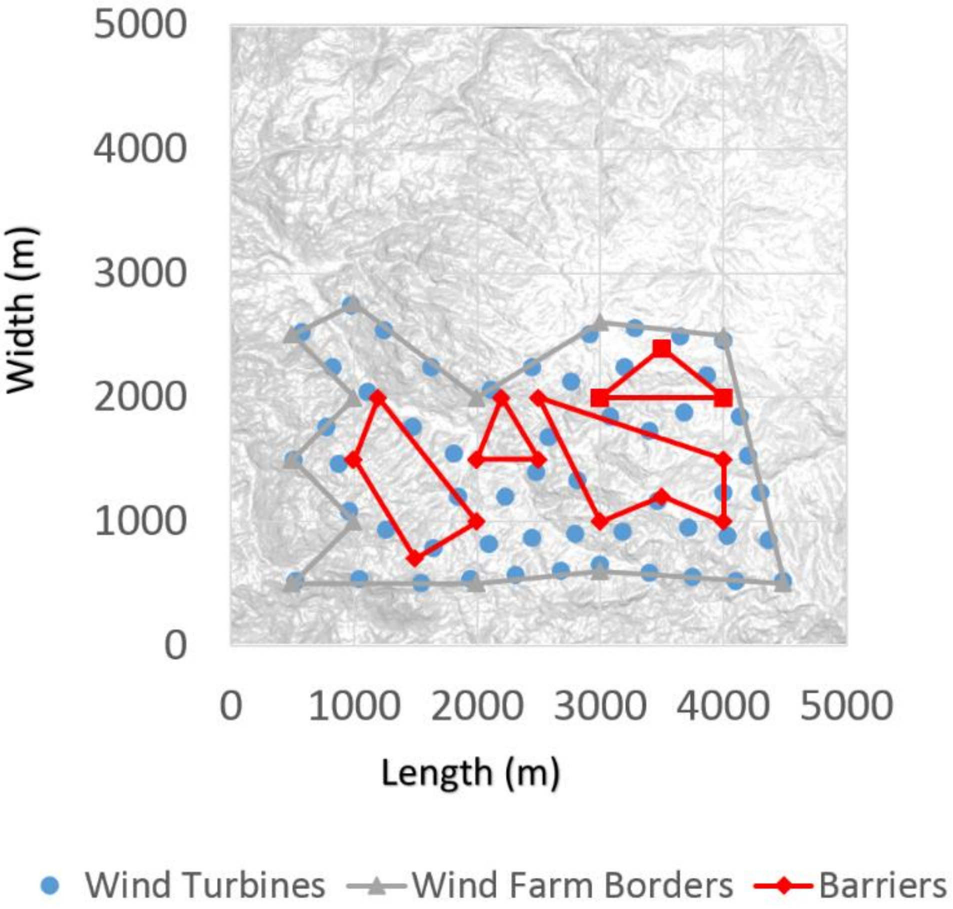

Figure 8.12 Final output of Modified RA.

9 Conclusions

This study examined the flow over a steep two-dimensional hill as well as the performance of a turbine located over the same hill. A good agreement between Experimental and Numerical simulations was achieved for the average vertical wind speed profiles. These results displayed the impact of the steep hill on air flow.

Moment acting on turbine was lowest upstream of the hill, and highest at the top of the hill. This is due to the higher wind speed at the top of the hill compared with upstream wind speed.

A good agreement between wind tunnel test and CFD results was achieved for the wind turbine power coefficient by using the Transition SST model. The Transition SST model yielded better results than the SST k-omega turbulence model specifically at high tip speed ratios.

An engineering wake model, that considers acceleration on a two-dimensional hill, was developed based on the momentum theory. The model consists of the wake width and wake wind speed. The equation to calculate the rotor thrust, which is calculated by the wake wind speed profiles, was also formulated. Then, the model was validated through wind tunnel test and CFD. The results obtained by using the current model were close to the wind tunnel test and CFD results, and by using the current model, it was possible to estimate the wake shrinkage in accelerating two-dimensional wind field.

In this thesis, a wind-tunnel test was conducted to investigate wake development over a two-dimensional hill in simple flow conditions, where a uniform approach-flow with turbulence intensity less than 0.5 % was used. Conducting the wind-tunnel test in such simple flow conditions was necessary for this study in order to investigate the effect of the hill on wake development and evaluate the new wake model without the influence of the Atmospheric Boundary Layer (ABL), ground roughness, or turbulence.

The wake model was compared with the wind-tunnel test, and the results obtained by using the wake model were close to the wind-tunnel test results. The wake model was able to estimate the wake shrinkage in accelerating two-dimensional wind field.

The measured wake width at the top of the hill was lower than the estimated value (by the wake model), this could be because the wake center at the top of the hill was moved downwards due to the hill effect.

In the wind-tunnel test, the hill surface was smooth as it was made of ABS resin, however, the surface roughness may affect wind speed profiles over the hill. Consequently, the effect of the surface roughness on wake development must be considered in the future studies.

Further experimental and numerical studies where the approach-flow represents real atmospheric conditions (where the ABL is reproduced) are required to investigate wake development over the hill in conditions that wind turbines experience in the field. Further modifications to the wake model are necessary to include the effect of turbulence and ground roughness on wake development over the hill, and to extend the wake model to decelerating wind field (downstream of the hill).

The wake model introduced in this thesis could be integrated into wind farm layout optimization algorithms to estimate far-wake shrinkage in accelerating wind field, which was not possible previously using the Jensen or the adapted Jensen wake models.

A wind farm layout optimization algorithm was developed, where a Genetic Algorithm was used as an initial step for the optimization process. Then, new Random Algorithm was developed to overcome the limitations of the Genetic Algorithm and improve the output of the optimization algorithm.

CTFLOW (Complex Terrain Farm Layout Optimization Workbench) was developed by the author for layout optimization over complex terrain. CTFLOW can import satellite terrain images then convert them directly to an STL file, rather than creating the STL file manually (which can be a tedious and time consuming task). CTFLOW will automatically run CFD simulations of wind flow over the terrain using the STL file generated. The CFD simulations will be performed in at least 16 directions to obtain wind speed and turbulence intensity profiles over the terrain, this is an important step for layout optimization over complex terrain, as the algorithm will avoid placing wind turbines in areas with high turbulence intensities, then wind speed and turbulence intensity profiles will be imported. Then, layout optimization using GA will start. The GA consists of the following steps: 1. Create Parent, Offspring, and Elite sets. 2. Create the initial grid of wind turbines. 3. Randomly generate new populations. 4. Evaluate the fitness of each population with respect to the fitness function.5. Select parents and choose Elite. 6. Produce children from parents either by mutation or crossover. 7. Replace current population with children to form the next generation.8. Start again from step 4, and stop when a predetermined condition is met. Then the new Random Algorithm will be used to improve the output of the GA as follows: 1. Use the output of the GA as an initial solution to the Random Algorithm. 2. Generate new random locations which favors high elevations and high wind speeds, and doesn’t favor lower elevations, low wind speeds, or high turbulence intensity areas. 3. Select a random turbine from the initial solution. 4. Move the selected turbine to one of the new random locations generated in step 2. 5. Check if the distance between any two turbines less than 4D: if True: ignore step 4 and start again from step 3, if False: continue to step 6. 6. Evaluate the Cost of Energy (COE) of the new wind farm layout: if COE increase: ignore step 4 and start again from step 3, if COE decrease: keep the selected turbine at the new location. 7. Start again from step 3, and stop when a predetermined condition is met.

References

[1] World Wind Energy Association (WWEA), "https://wwindea.org/," February 25, 2019. [Online]. Available: https://wwindea.org/blog/2019/02/25/wind-power-capacity-worldwide-reaches-600-gw-539-gw-added-in-2018/. [Accessed 31 May 2019].

[2] World Wind Energy Association (WWEA), "https://wwindea.org/," October 10, 2016. [Online]. Available: https://wwindea.org/blog/2016/10/10/wwea-half-year-report-worldwind-wind-capacity-reached-456-gw/. [Accessed 31 May 2019].

[3] World Wind Energy Association (WWEA), "https://wwindea.org/," June 8, 2017. [Online]. Available: https://wwindea.org/blog/2017/06/08/11961-2/. [Accessed 31 May 2019].

[4] Wind Engineering Section, RIAM, Kyushu University, "https://www.riam.kyushu-u.ac.jp/," [Online]. Available: https://www.riam.kyushu-u.ac.jp/windeng/en_MultiRotorTurbine.html. [Accessed 31 May 2019].

[5] J. Cleijne, "Results of Sexbierum Wind Farm; single wake measurements," TNO-Report 93-082, TNO Institute of Environmental and Energy Technology, 1993.

[6] P. B. S. Lissaman, "Energy Effectiveness of Arbitrary Arrays of Wind Turbines," *Journal of Energy,* vol. 3, no. 6, pp. 323-328, 1979.

[7] H. E. Neustadter and D. A. Spera, "Method for Evaluating Wind Turbine Wake Effects on Wind Farm Performance," *J. Sol. Energy Eng,* vol. 107, no. 3, pp. 240-243, 1985.

[8] R. Barthelmie, S. Frandsen, K. Hansen, J. Schepers, K. Rados, W. Schlez, A. Neubert, L. Jensen and S. Neckelmann, "Modelling the impact of wakes on power output at Nysted and Horns Rev," in *European Wind Energy Conference and Exhibition*, Marseilles, 2009.

[9] R. Barthelmie, S. Frandsen, O. Rathmann, E. Politis, J. Prospathopoulos, K. Rados, K. Hansen, D. Cabezon, W. Schlez, J. Phillips, A. Neubert, S. van der Pijl and J. Schepers, "Flow and wakes in large wind farms in complex terrain and offshore," in *American Wind Energy Association Conference*, Houston, Texas, 2008.

[10] Vattenfall, "flickr," License: Creative Commons, Attribution-NonCommercial-NoDerivs 2.0 Generic. Taken on September 18, 2010. [Online]. Available: https://www.flickr.com/photos/vattenfall/5020350552/in/album-72157619406616767/. [Accessed 30 May 2019].

[11] L. J. Vermeer, J. N. Sørensen and A. Crespo, "Wind turbine wake aerodynamics," *Progress in Aerospace Sciences,* vol. 39, pp. 467-510, 2003.

[12] B. Sanderse, "Aerodynamics of wind turbine wakes," Energy Research Centre of the Netherlands (ECN), ECN-E–09-016, 2009.

[13] Vattenfall, "flickr," License: Creative Commons, Attribution-NoDerivs 2.0 Generic. Taken on January 13, 2010. [Online]. Available: https://www.flickr.com/photos/vattenfall/4270899001/in/album-72157619406616767/. [Accessed 29 May 2019].

[14] M.-K. LIU, M. YOCKE and T. MYERS, "Mathematical model for the analysis of wind-turbine wakes," *Journal of Energy,* vol. 7, no. 1, pp. 73-78, 1983.

[15] D. Elliott, "Status of wake and array loss research," in *Windpower Conference*, Palm Springs, California, 1991.

[16] J. Ainslie, "Development of an eddy-viscosity model for wind turbine wakes," in *BWEA conference*, 1985.

[17] J. Ainslie, "Calculating the flowfield in the wake of wind turbines," *Journal of Wind Engineering and Industrial Aerodynamics,* vol. 27, pp. 213-224, 1988.

[18] J. Højstrup, "Spectral coherence in wind turbine wakes," *Journal of Wind Engineering and Industrial Aerodynamics,* vol. 80, pp. 137-146, 1999.

[19] J. Dahlberg, M. Poppen and S. Thor, "Load/fatigue life effects on a wind turbine generator in a wind farm," in *European Wind Energy Conference*, 1991.

[20] H. Aagaard Madsen, G. C. Larsen and K. Thomsen, "Wake flow characteristics in low ambient turbulence conditions," in *Copenhagen Offshore Wind*, Copenhagen, Denmark, 2005.

[21] G. C. Larsen, H. Madsen Aagaard, F. Bingöl, J. Mann, S. Ott, J. Sørensen, V. Okulov, N. Troldborg, N. M. Nielsen, K. Thomsen, T. J. Larsen and R. Mikkelsen, "Dynamic wake meandering modeling," Risø-R-1607(EN), Risø National Laboratory, Technical University of Denmark, 2007.

[22] D. Medici, "Experimental studies of wind turbine wakes - power optimisation and meandering," PhD thesis, KTH Mechanics, Royal Institute of Technology,, 2005.

[23] D. Medici and P. Alfredsson, "Measurements behind model wind turbines: further evidence of wake meandering," *Wind Energy,* vol. 11, p. 211–217, 2008.

[24] T. Burton, D. Sharpe, N. Jenkins and E. Bossanyi, Wind Energy Handbook, John Wiley & Sons, Ltd, 2001.

[25] I. Katic, J. Højstrup and N. Jensen, "A simple model for cluster efficiency," in *European Wind Energy Association Conference and Exhibition*, Rome, Italy, 1987.

[26] J. Feng and W. Z. Shen, "Wind farm layout optimization in complex terrain: A preliminary study on a Gaussian hill," *J. Phys.: Conf. Ser.*, vol. 524, p. 012146, 2014.

[27] J. Feng, W. Z. Shen, K. S. Hansen, A. Vignaroli, A. Bechmann, W. J. Zhu, G. C. Larsen, S. Ott, M. Nielsen, M. Jogararu and e. al, "Wind farm design in complex terrain: the FarmOpt methodology," in *China Wind Power 2017*, China International Exhibition Center (New Venue), Beijing, China, 2017.

[28] O. Ibrahim and S. Yoshida, "Experimental and Numerical Studies of a Horizontal Axis Wind Turbine Performance over a Steep 2D Hill," *Evergreen* , vol. 5, no. 3, pp. 12-21, 2018.

[29] O. Ibrahim, S. Yoshida, M. Hamasaki and A. Takada, "Decay Factor of Wind Turbine Wake in Accelerated Wind Field.," in *JWEA Wind Energy Symposium*, Tokyo, 2018.

[30] S. Yoshida, "Performance of Downwind Turbines in Complex Terrains," *Wind Engineering*, vol. 30, no. 6, pp. 487-501, 2006.

[31] T. Uchida, T. Maruyama, H. Ishikawa, M. Zako and A. and Deguchi, "Investigation of the Causes of Wind Turbine Blade Damage at Shiratakiyama Wind Farm in Japan : A Computer Simulation Based Approach," vol. 141, p. 13 – 25, 2011.

[32] G. Li, S. Takakuwa and T. and Uchida, "Application of CFD for Turbulence Related Operational Risks Assessment of Wind Turbines in Complex Terrain," in *EWEA2013*, Vienna, 2013.

[33] W. Tian, A. Ozbay, W. Yuan, P. Sarakar and H. Hu, "An Experimental Study on the Performances of Wind Turbines Over Complex Terrain," in *51st AIAA Aerospace Sciences Meeting including the New Horizons Forum and Aerospace Exposition*, Texas, 2013.

[34] D. R. Webster, D. B. DeGraaff and J. K. Eaton, "Turbulence Characteristics of a Boundary Layer Over a Two-Dimensional Bump," *J. Fluid Mech.,* vol. 320, pp. 53-69, 1996.

[35] C. G. Helmis, K. H. Papadopoulos, D. N. Asimakopoulos, P. G. Papageorgas and A. T. Soilemes, "An Experimental Study of the Near-Wake Structure of a Wind Turbine Operating Over Complex Terrain," *Solar Energy,* vol. 54, pp. 413-428, 1995.

[36] K. W. Ayotte and D. E. Hughes, "Observations of Boundary-Layer Wind-Tunnel Flow Over Isolated Ridges of Varying Steepness and Roughness," *Boundary-Layer Meteorology,* vol. 112, p. 525–556, 2004.

[37] J. Walmsley, P. Taylor and T. Keith, "A simple model of neutrally stratified boundary-layer flow over complex terrain with surface roughness modulations (MS3DJH/3R)," *Boundary-Layer Meteorology,* vol. 36, p. 157–186, 1986.

[38] A. Beljaars, J. Walmsley and P. Taylor, "A mixed spectral finite-difference model for neutrally stratified boundary-layer flow over roughness changes and topography," *Boundary-Layer Meteorology,* vol. 38, pp. 273-303, 1987.

[39] I. Troen and E. Petersen, "European Wind Atlas," Risø National Laboratory, Roskilde, Denmark, 1989.

[40] K. W. Ayotte and P. A. Taylor, "A Mixed Spectral Finite-Difference 3D Model of Neutral Planetary Boundary-Layer Flow over Topography," *J. Atmos. Sci.,* vol. 52, p. 3523–3538, 1995.

[41] S. Cao and T. Tamura, "Experimental study on roughness effects on turbulent boundary layer flow over a two-dimensional steep hill," *Journal of Wind Engineering and Industrial Aerodynamics,* vol. 94, pp. 1-19, 2006.

[42] T. Allen, "Flow over Hills with Variable Roughness," *Boundary-Layer Meteorology,* vol. 121, p. 475–490, 2006.

[43] S. Cao and T. Tamura, "Effects of roughness blocks on atmospheric boundary layer flow over a two-dimensional low hill with/without sudden roughness change," *Journal of Wind Engineering and Industrial Aerodynamics,* vol. 95, pp. 679-695, 2007.

[44] E. S. Politis, J. Prospathopoulos, D. Cabezon, K. S. Hansen, P. K. Chaviaropoulos and R. J. Barthelmie, "Modeling wake effects in large wind farms in complex terrain: the problem, the methods and the issues," *Wind Energy,* vol. 15, pp. 161-182, 2012.

[45] A. Makridis and J. Chick, "Validation of a CFD model of wind turbine wakes with terrain effects," *Journal of Wind Engineering and Industrial Aerodynamics,* vol. 123, pp. 12-29, 2013.

[46] K. S. Hansen, G. C. Larsen, R. Menke, N. Vasiljevic, N. Angelou, J. Feng, W. J. Zhu, A. Vignaroli, W. Liu W, C. Xu and W. Z. Shen, "Wind turbine wake measurement in complex terrain," *Journal of Physics: Conference Series,* vol. 753, p. 032013, 2016.

[47] F. Castellani, D. Astolfi, M. Mana, E. Piccioni, M. Becchetti and L. Terzi, "Investigation of terrain and wake effects on the performance of wind farms in

complex terrain using numerical and experimental data," *Wind Energy,* vol. 20, p. 1277–1289, 2017.

[48] D. Astolfi, F. Castellani and L. Terzi, "A study of wind turbine wakes in complex terrain through RANS simulation and SCADA data," *Journal of Solar Energy Engineering,* vol. 140, no. 3, p. 031001, 2018.

[49] A. Hyvärinen and A. Segalini, "Effects from complex terrain on wind-turbine performance," *Journal of Energy Resources Technology,* vol. 139, no. 5, p. 051205, 2017.

[50] A. Hyvärinen and A. Segalini, "Qualitative analysis of wind-turbine wakes over hilly terrain," *Journal of Physics: Conference Series*, vol. 854, p. 012023, 2017.

[51] F. Porté-Agel, Y.-T. Wu, H. Lu and R. J. Conzemius, "Large-Eddy Simulation of Atmospheric Boundary Layer Flow through Wind Turbines and Wind Farms," *Journal of Wind Engineering and Industrial Aerodynamics*, vol. 99, no. 4, pp. 154-168, 2011.

[52] H. Zhong, P. Du, F. Tang and L. Wang, "Lagrangian Dynamic Large-Eddy Simulation of Wind Turbine near Wakes Combined with an Actuator Line Method," *Applied Energy,* vol. 144, pp. 224-233, 2015.

[53] J. Berg, N. Troldborg, N. N. Sørensen, E. G. Patton and P. P. Sullivan, "Large-Eddy Simulation of turbine wake in complex terrain," *Journal of Physics: Conference Series,* vol. 854, p. 012003, 2017.

[54] M. Tabib, A. Rasheed and F. Fuchs, "Analyzing complex wake-terrain interactions and its implications on wind-farm performance," *Journal of Physics: Conference Series,* vol. 753, p. 032063, 2016.

[55] O. Ibrahim, S. Yoshida, M. Hamasaki and A. Takada, "Wind Turbine Wake Modeling in Accelerating Wind Field: A Preliminary Study on a Two-Dimensional Hill," *Fluids,* Vols. 4, 153, 2019.

[56] [Online]. Available: http://www.riam.kyushu-u.ac.jp/windeng/en_index.html.

[57] Y. Ohya and T. Karasudani, "A shrouded wind turbine generating high output power with wind-lens technology," *Energies,* vol. 3, no. 4, pp. 634-649, 2010.

[58] U. Goltenbott, Y. Ohya, S. Yoshida and P. Jamieson, "Aerodynamic interaction of diffuser augmented wind turbines in multi-rotor systems," *Renewable Energy,* vol. 112, pp. 25-34, 2017.

[59] Kanomax, "http://www.kanomax.co.jp/," [Online]. Available: http://www.kanomax.co.jp/img_data/file_730_1358246410.pdf. [Accessed 30 May 2019].

[60] NISSHO ELECTRIC WORKS CO., LTD., [Online]. Available: http://www.nissho-ew.co.jp/_userdata/LMC-6566A.pdf. [Accessed June 7, 2019].

[61] F. Zahle, N. N. Sørensen and J. Johansen, "Wind turbine rotor-tower interaction using an incompressible overset grid method," *Wind Energy,* vol. 12, no. 6, p. 594–619, 2009.

[62] N. N. Sørensen, J. A. Michelsen and S. Schreck, "Navier–Stokes predictions of the NREL phase VI rotor in the NASA Ames 80 ft × 120 ft wind tunnel," *Wind Energy,* vol. 5, pp. 151-169, 2002.

[63] J. Mo, A. Choudhry, M. Arjomandi and Y. Lee, "Large eddy simulation of the wind turbine wake characteristics in the numerical wind tunnel model,"

Journal of Wind Engineering and Industrial Aerodynamics, vol. 112, pp. 11-24, 2013.

[64] F. Zahle and N. N. Sørensen, "On the influence of far-wake resolution on wind turbine flow simulations," *Journal of Physics: Conference Series,* vol. 75, no. https://doi.org/10.1088/1742-6596/75/1/012042, p. 012042, 2007.

[65] E. P. N. Duque, C. P. van Dam and S. C. Hughes, "Navier-Stokes simulations of the NREL combined experiment phase II rotor," in *37th Aerospace Sciences Meeting and Exhibit*, Reno,NV,U.S.A, 1999.

[66] F. Zahle and N. N. Sørensen, "Overset grid flow simulation on a modern wind turbine," in *26th AIAA Applied Aerodynamics Conference*, Honolulu, Hawaii, 2008.

[67] P. Réthoré, P. Laan, N. Troldborg, F. Zahle and N. N. Sørensen, "Verification and validation of an actuator disc model," *Wind Energy,* vol. 17, no. 6, pp. 919-937, 2014.

[68] P. Réthoré, N. N. Sørensen and F. Zahle, "Validation of an actuator disc model," in *EWEC 2010*, 2010.

[69] J. Johansen, N. N. Sørensen, J. A. Michelsen and S. Schreck, "Detached-eddy simulation of flow around the NREL Phase VI blade," *Wind Energy,* vol. 5, pp. 185-197, 2002.

[70] N. N. Sørensen and A. Myken, "Unsteady actuator disc model for horizontal axis wind turbines," *Journal of Wind Engineering and Industrial Aerodynamics,* vol. 39, pp. 139-149, 1992.

[71] C. Masson, A. Smaïli and C. Leclerc, "Aerodynamic analysis of HAWTs operating in unsteady conditions," *Wind Energy,* vol. 4, pp. 1-22, 2001.

[72] F. Castellani and A. Vignaroli, "An application of the actuator disc model for wind turbine wakes calculations," *Applied Energy*, vol. 101, pp. 432-440, 2013.

[73] N. Troldborg, J. N. Sørensen and R. Mikkelsen, "Actuator Line Simulation of Wake of Wind Turbine Operating in Turbulent Inflow," *Journal of Physics: Conference Series*, vol. 75, p. 012063, 2007.

[74] G. D. Raithby, G. D. Stubley and P. A. Taylor, "The Askervein Hill project: a finite control volume prediction of three-dimensional flows over the hill," *Boundary-Layer Meteorology*, vol. 39, no. 3, p. 247–267, 1987.

[75] N. N. Sørensen, "General purpose flow solver applied to flow over hills," Risø National Laboratory, Risø-R-827(EN), 1995.

[76] B. E. Launder and D. B. Spalding, "The numerical computation of turbulent flows," *Computer Methods in Applied Mechanics and Engineering,* vol. 3, no. 2, p. 269–289, 1974.

[77] A. Bechmann and N. N. Sørensen, "Hybrid RANS/LES method for wind flow over complex terrain," *Wind Energy*, vol. 13, p. 36–50, 2010.

[78] Z. Liu, T. Ishihara, X. He and H. Niu, "LES study on the turbulent flow fields over complex terrain covered by vegetation canopy," *Journal of Wind Engineering and Industrial Aerodynamics*, vol. 155, pp. 60-73, 2016.

[79] A. Bechmann, "Large-Eddy Simulation of Atmospheric Flow over Complex Terrain," Risø National Laboratory, Risø-PhD-28(EN), 2006.

[80] J. Smagorinsky, "General circulation experiments with the primitive equations: I. The basic experiment," *Monthly Weather Review,* vol. 91, no. 3, p. 99–164, 1963.

[81] ANSYS, Inc., [Online]. Available: https://www.ansys.com/.

[82] F. R. Menter, R. B. Langtry, S. R. Likki, Y. B. Suzen, P. G. Huang and S. Völker, "A correlation-based transition model using local variables—part I: model formulation," *J. Turbomach,* vol. 128, no. 3, pp. 413-422, 2004.

[83] R. B. Langtry, F. R. Menter, S. R. Likki, Y. B. Suzen, P. G. Huang and S. Völker, "A correlation-based transition model using local variables—part II: test cases and industrial applications," *J. Turbomach,* vol. 128, no. 3, pp. 423-434, 2004.

[84] F. R. Menter, R. Langtry and S. Völker, "Transition modelling for general purpose CFD codes," *Flow Turbulence Combust,* vol. 77, p. 277–303, 2006.

[85] R. B. Langtry, J. Gola and F. R. Menter, "Predicting 2D airfoil and 3D wind turbine rotor performance using a transition model for general CFD codes," in *44th AIAA Aerospace Sciences Meeting and Exhibit*, Reno, Nevada, 2006.

[86] N. N. Sørensen, "CFD modelling of laminar-turbulent transition for airfoils and rotors using the γ - model," *Wind Energy,* vol. 12, no. 8, pp. 715-733, 2009.

[87] The OpenFOAM Foundation Ltd, [Online]. Available: https://openfoam.org/.

Appendices

Appendix A

Wind Turbine Load Measurement in the Wake over the hill

The objective of this configuration was to measure the load of a wind turbine operating in the wake of another wind turbine over the hill as shown in Figure A.1. The 1st wind turbine was located at X=-*L*. The 2nd wind turbine was located at X=-*L/2*, X = 0, X = *L/2*, and X = *L*. Both wind turbines had a diameter *D* = 0.512 m. The inlet wind velocity was 7 m/s. The forces acting on wind turbine in X, Y, and Z directions as well as the moments around X, Y, and Z directions were measured using a 6 component load cell.

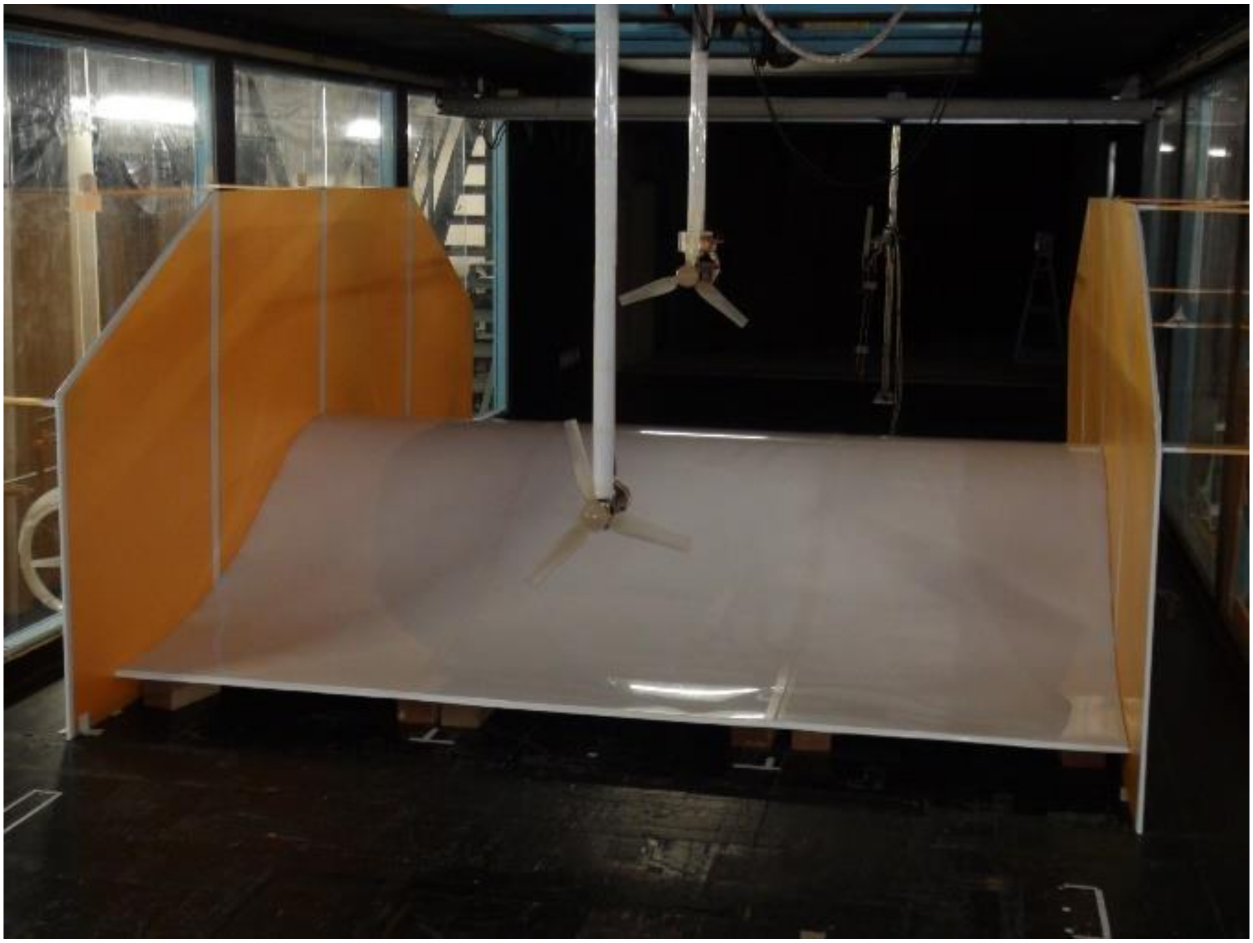

(a)

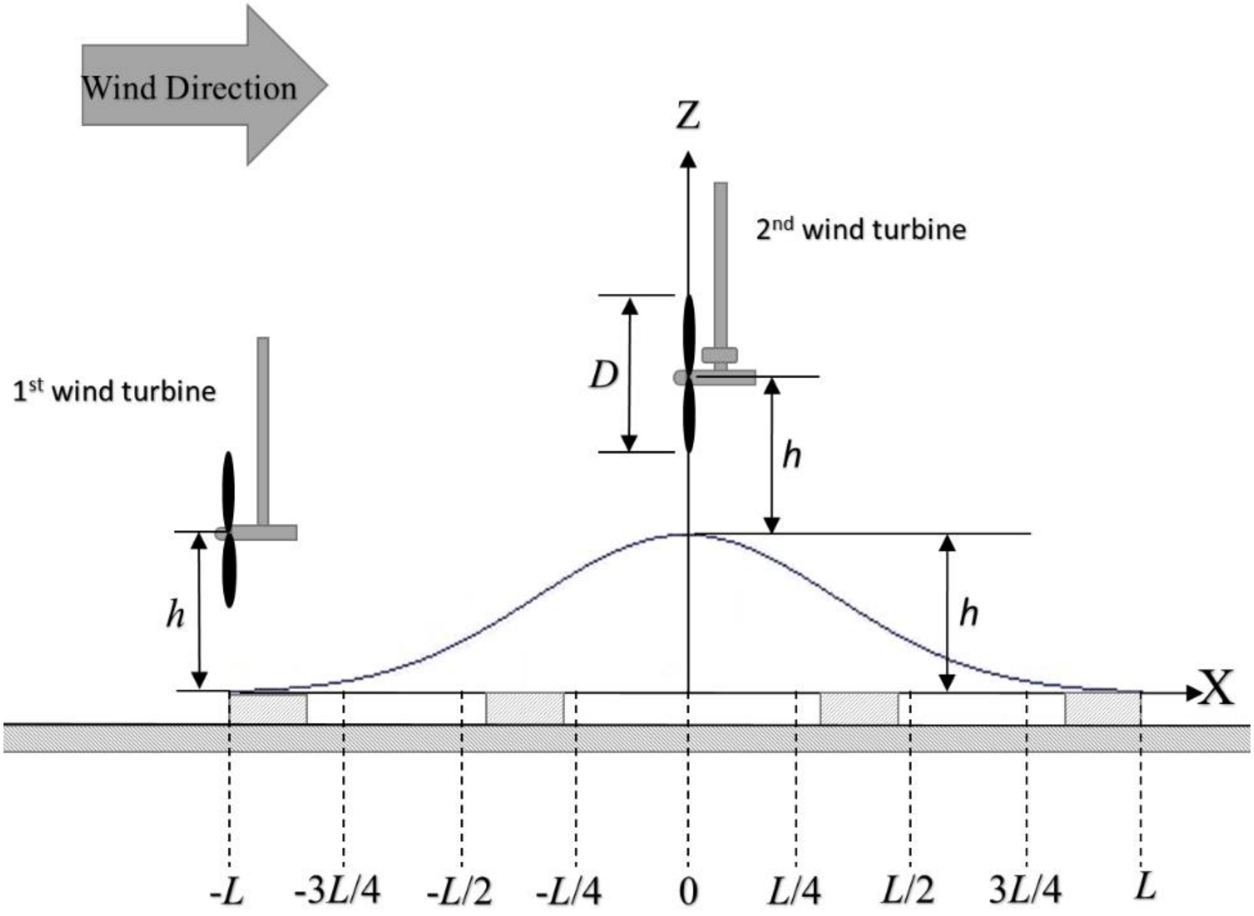

(b)

Figure A.1 (a) Wind tunnel test configuration setup; (b) a schematic diagram of the measurement setup.

C_p and C_t of the 2nd wind turbine were obtained at X = - 780 mm, X = 0, X = 780 mm, and X = 1560 mm as shown in Figure A.2 to A.9. Rotational speeds of the 1st wind turbine was *n* = 783 rpm, 1044 rpm, and 1306 rpm.

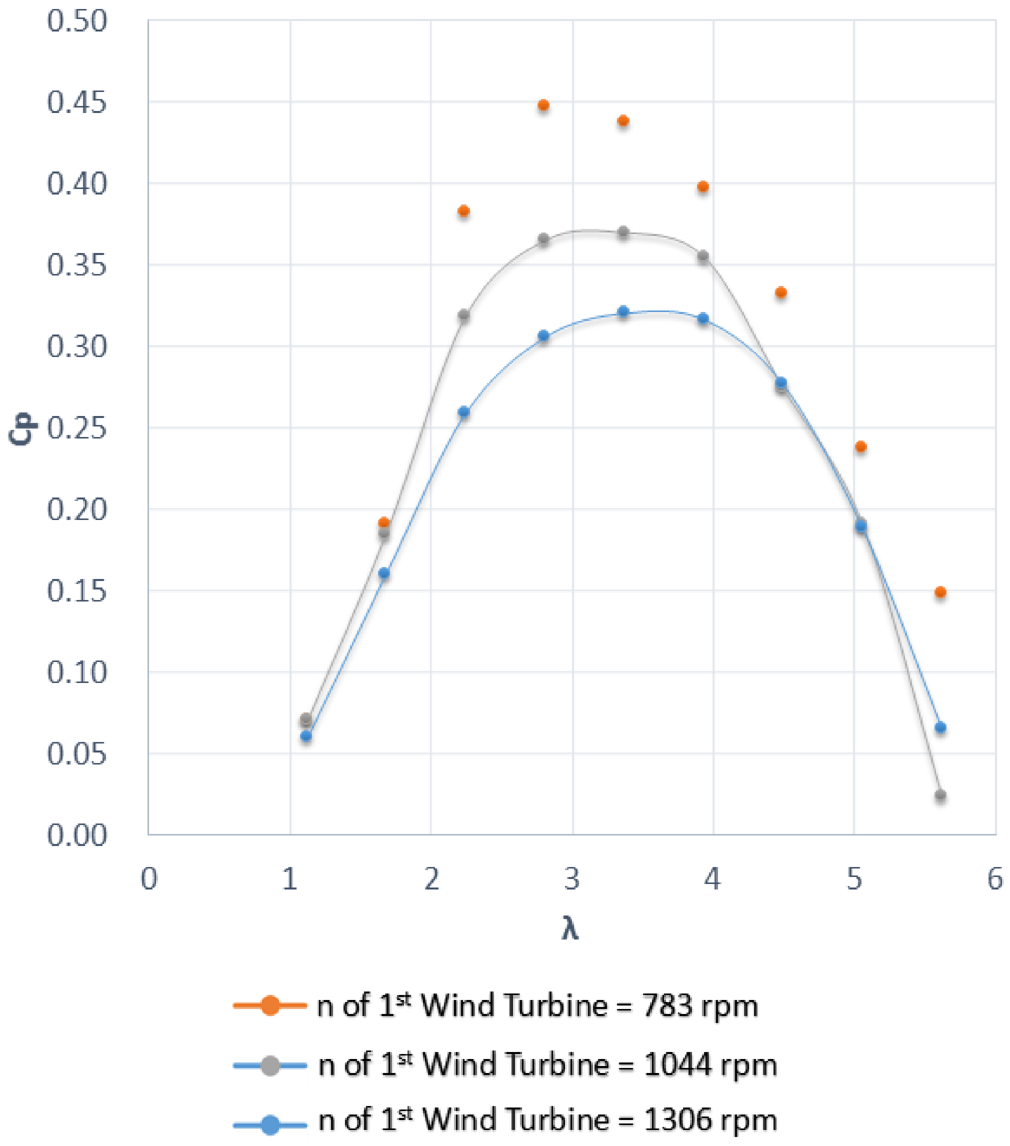

Figure A.2 1st WT at x=-1560mm, 2nd WT at x= -780mm

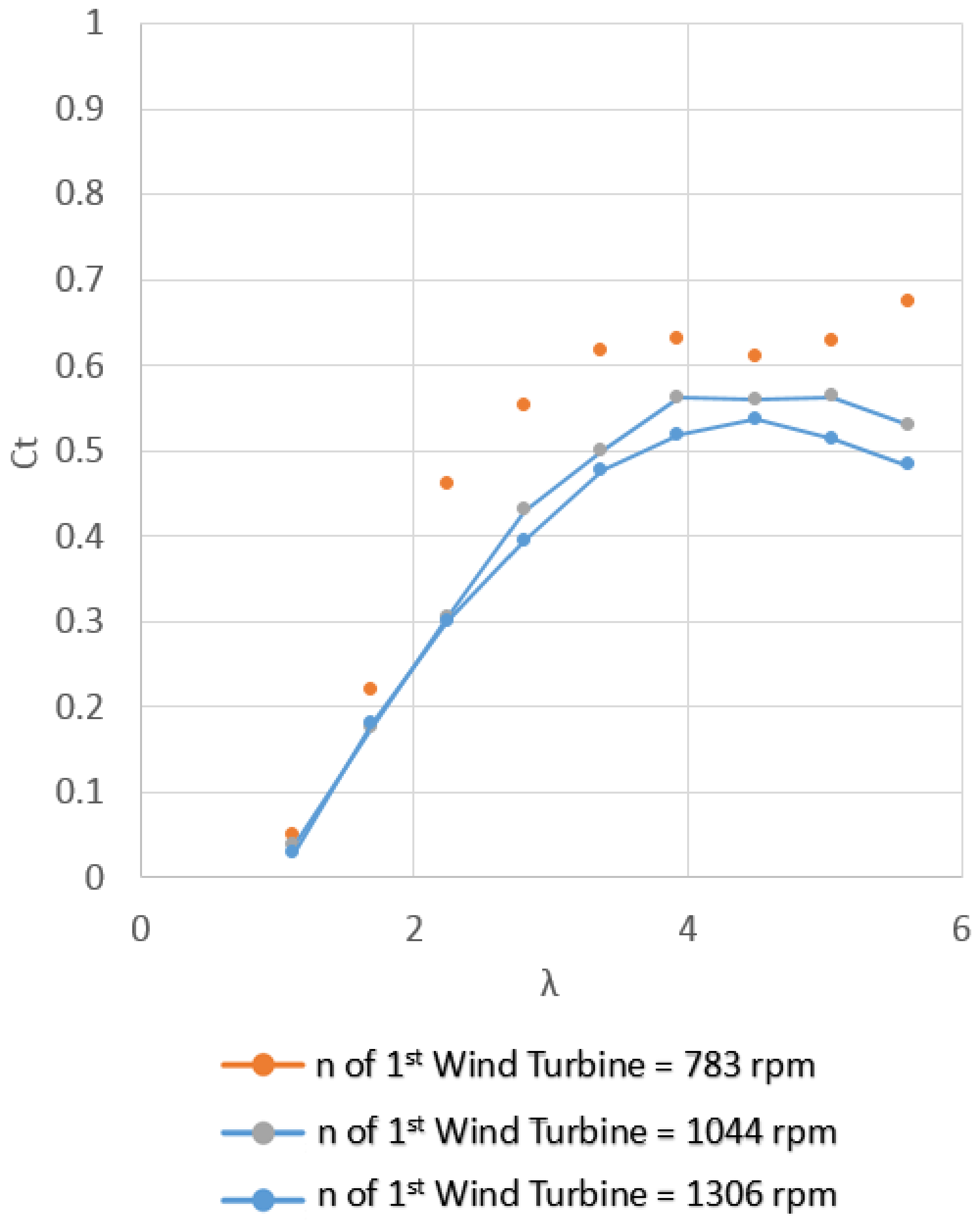

Figure A.3 1st WT at x=-1560mm, 2nd WT at x= -780mm

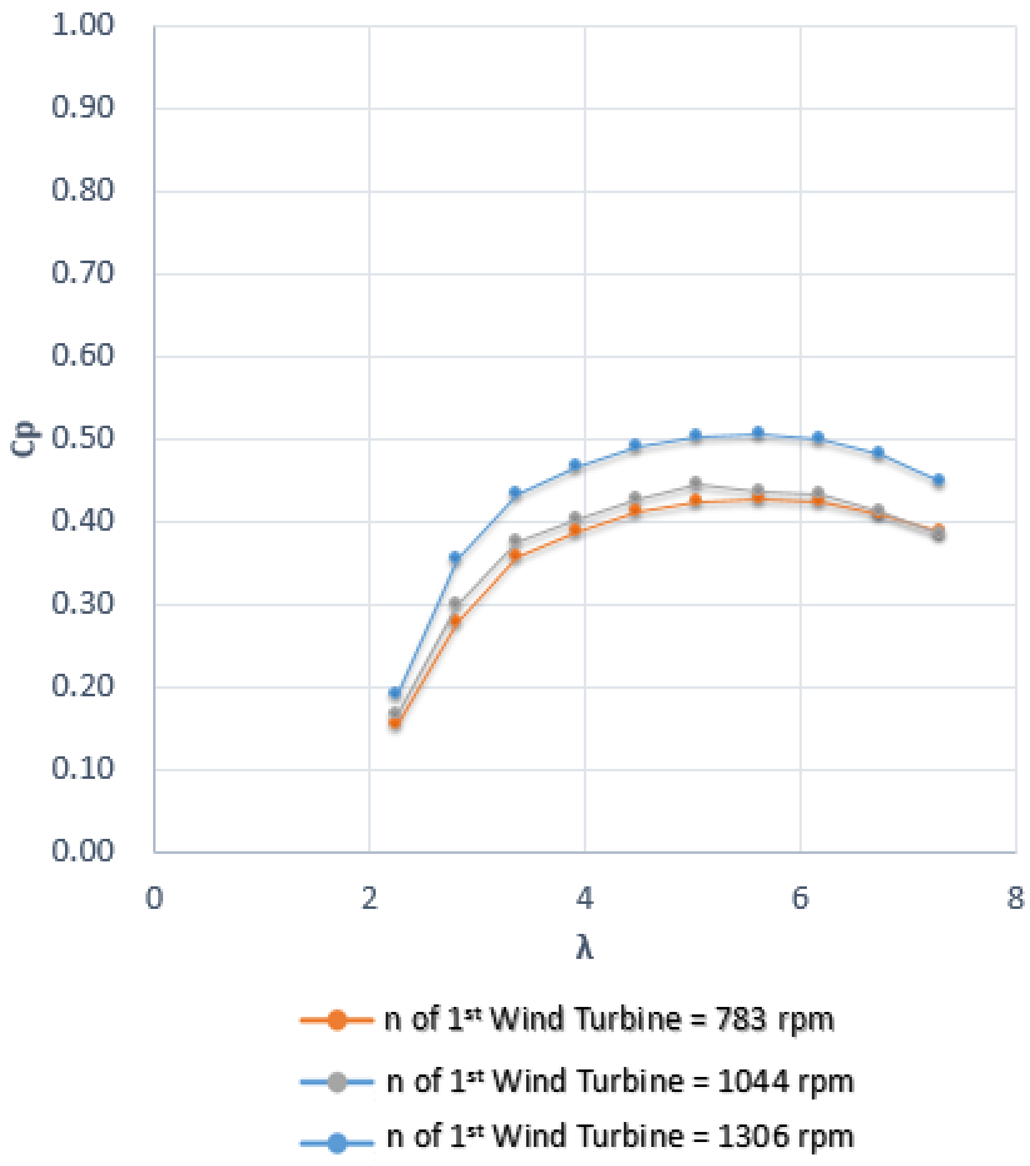

Figure A.4 1st WT at x=-1560mm, 2nd WT at x=0.

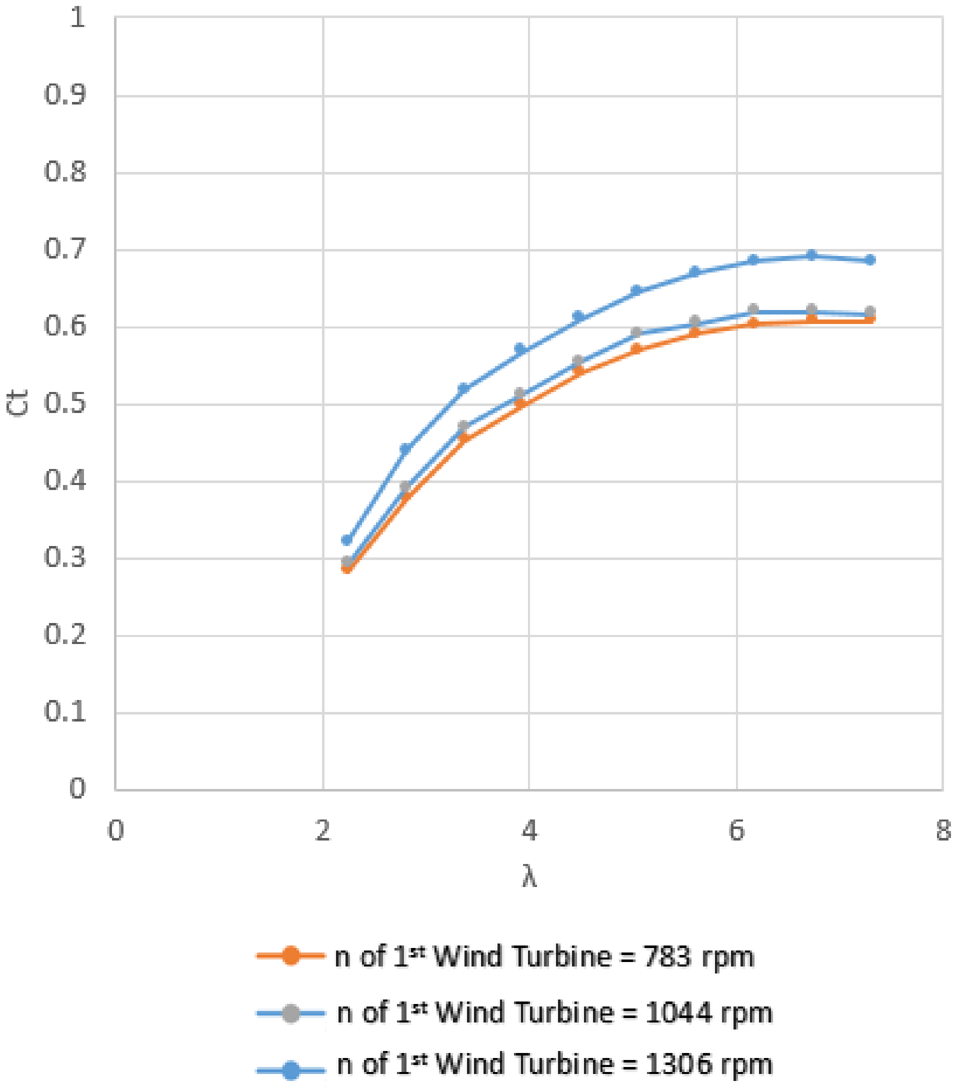

Figure A.5 1st WT at x=-1560mm, 2nd WT at x=0.

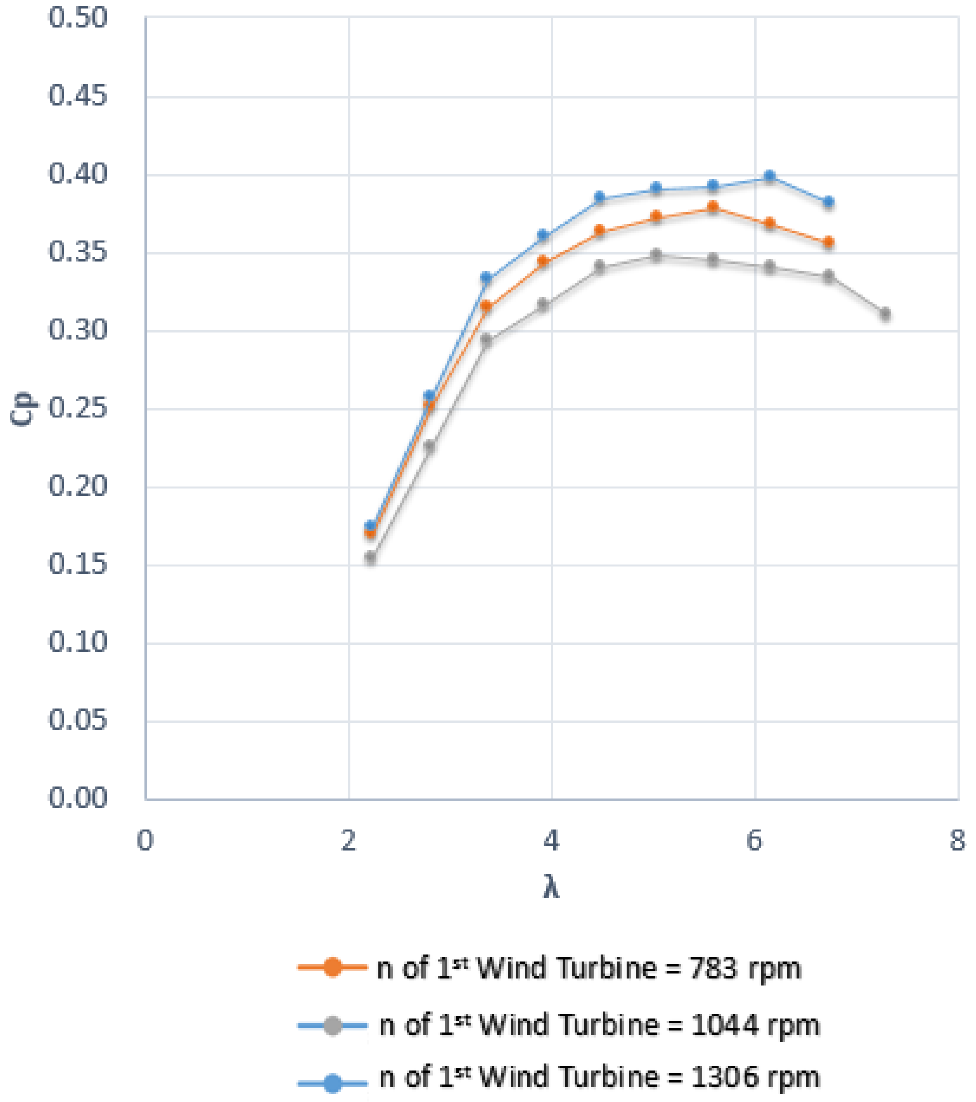

Figure A.6 1stWT at x=-1560mm, 2nd WT at x=+780mm.

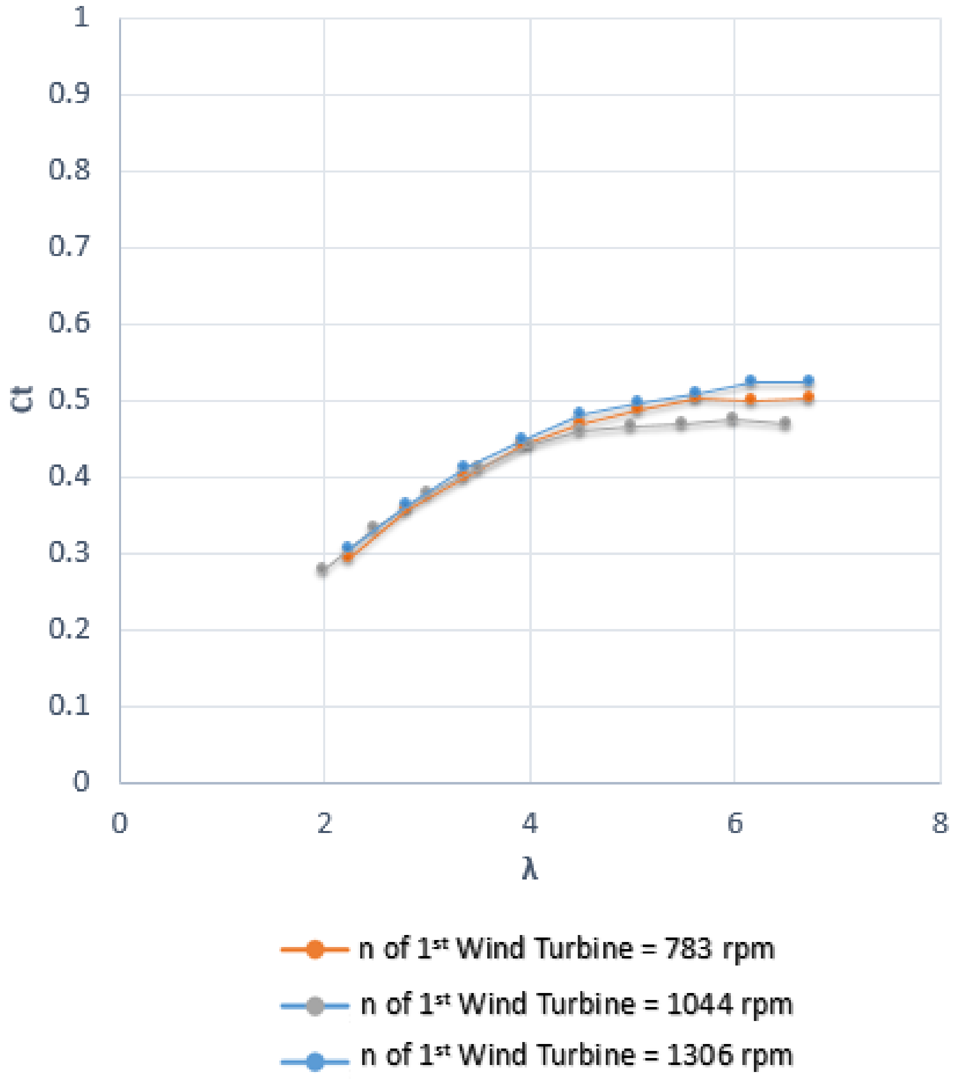

Figure A.7 1st WT at x=-1560mm, 2ndWT at x=+780mm.

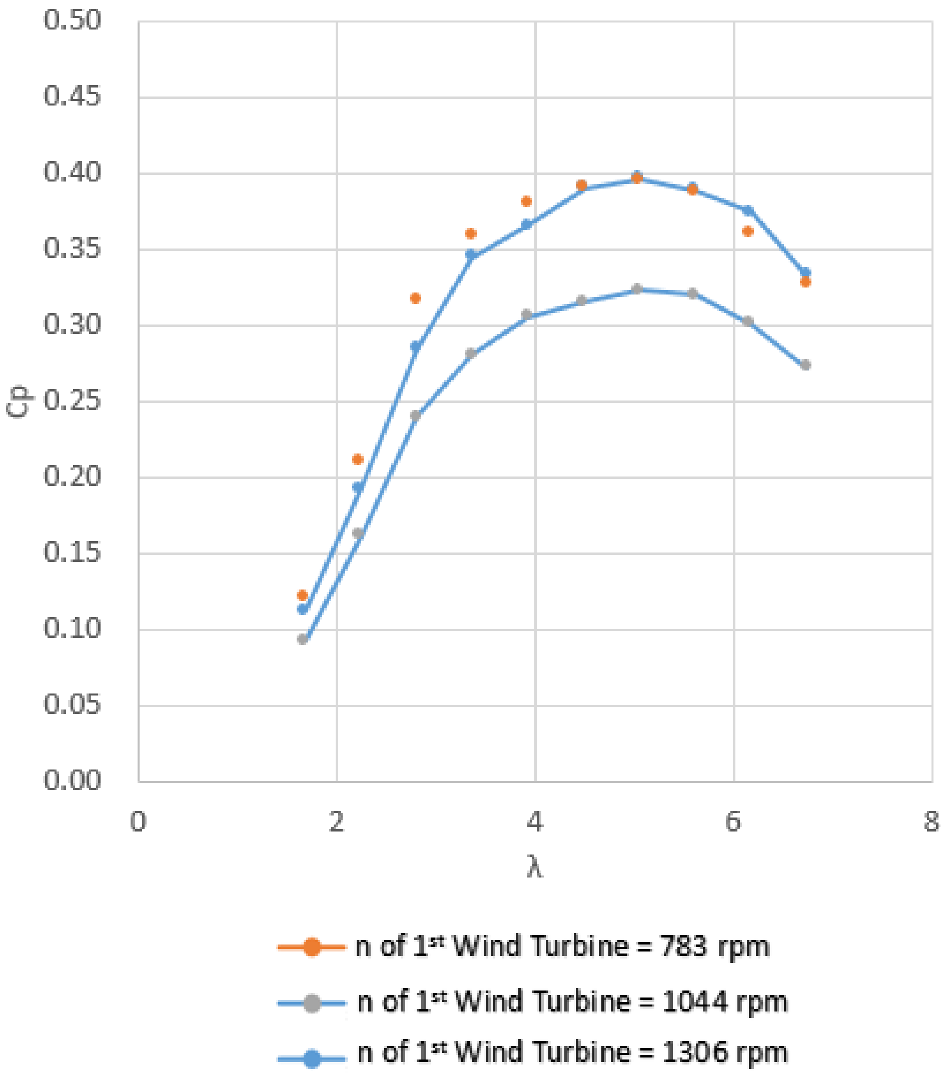

Figure A.8 1stWT at x=-1560mm, 2ndWT at x=+1560mm.

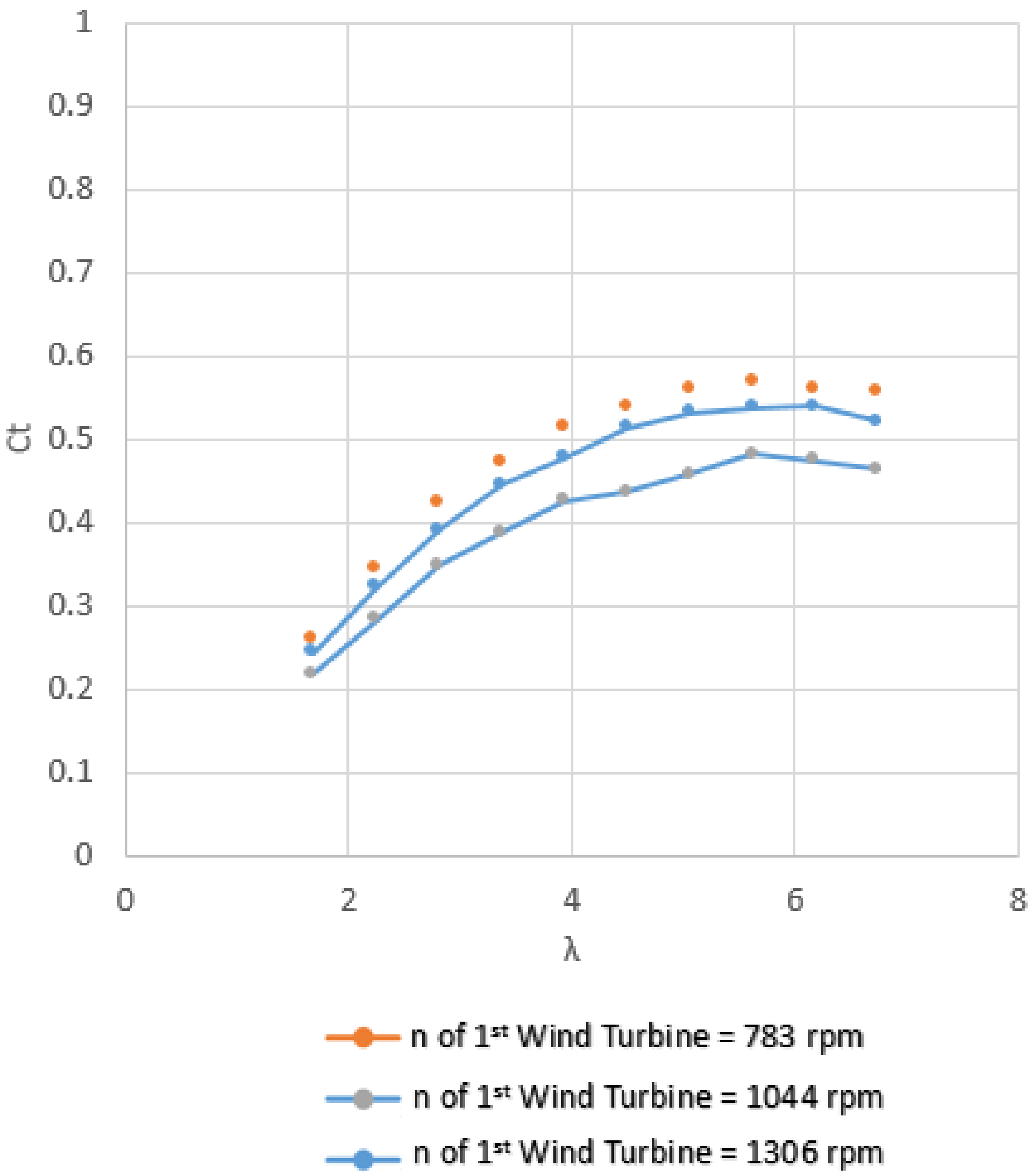

Figure A.9 1stWT at x=-1560mm, 2ndWT at x=+1560mm.

Appendix B

Wind Turbine Load Measurement in the Wake over Flat Terrain

The objective of this configuration was to measure the load of a wind turbine operating in the wake of another wind turbine over flat terrain as shown in Figure B.1. The 1st wind turbine was located at X=-*L*. The 2nd wind turbine was located at X = 0. Both wind turbines had a diameter D = 0.512 m. The inlet wind velocity was 7 m/s. The forces acting on wind turbine in X, Y, and Z directions as well as the moments around X, Y, and Z directions were measured using a 6 component load cell. Figure B.2 shows a comparison between the two-dimensional hill and the flat terrain.

(a)

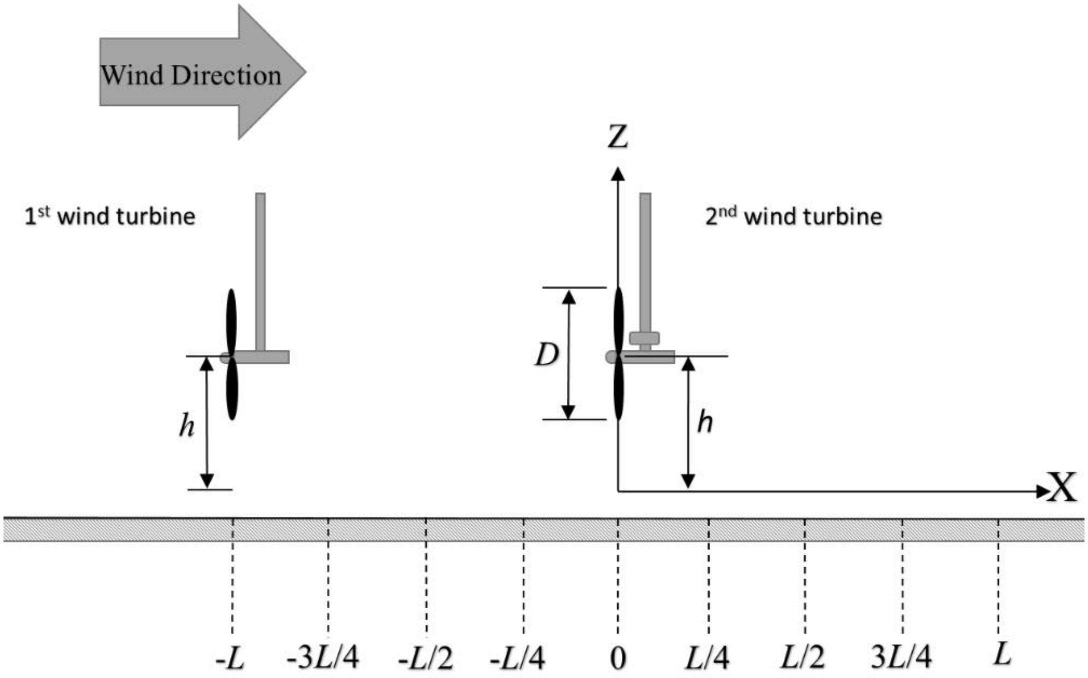

(b)

Figure B.1 (a) Wind tunnel test configuration setup; (b) a schematic diagram of the measurement setup.

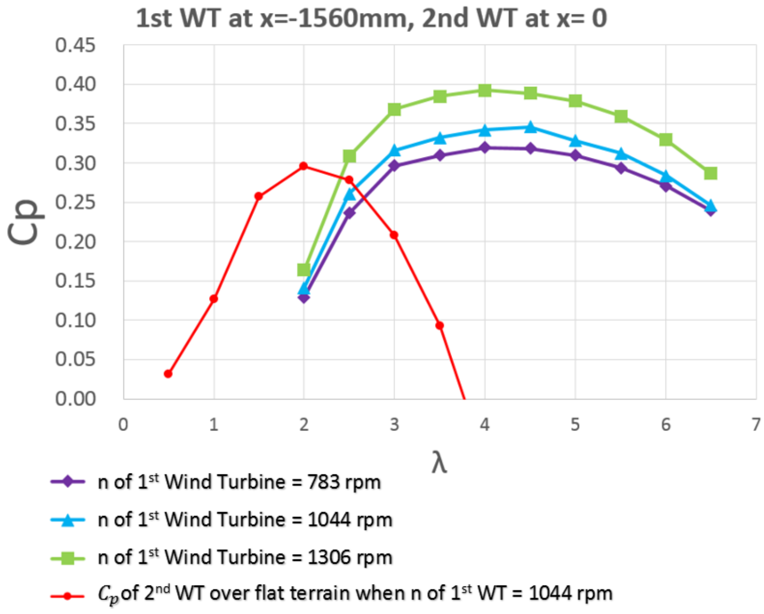

(a)

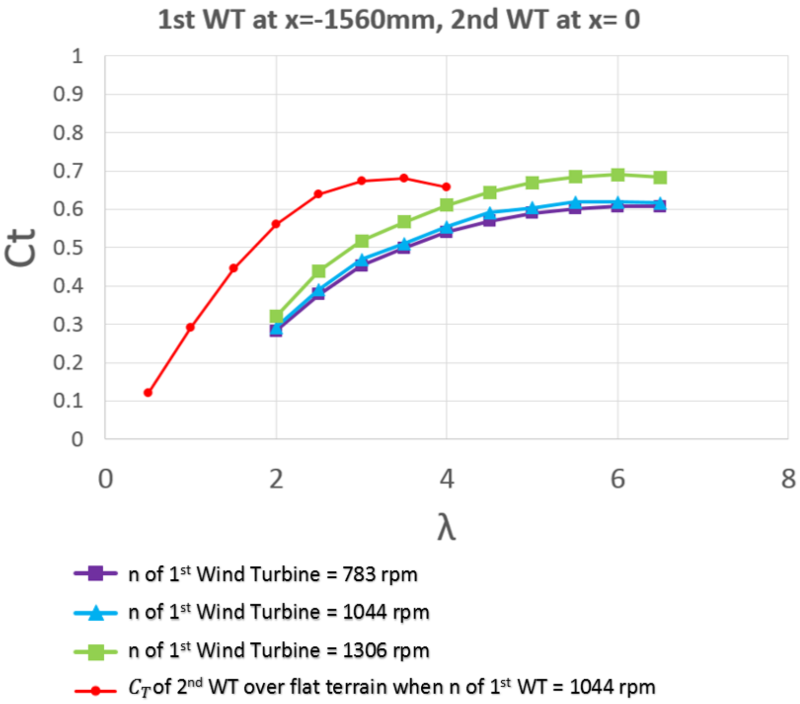

(b)

Figure B.2 A comparison between the two-dimensional hill and the flat terrain (a) Power coefficient; (b) Thrust coefficient.